THÈSE

En vue de l'obtention du

DOCTORAT DE L'UNIVERSITÉ DE TOULOUSE

Délivré par
Institut National Polytechnique de Toulouse (INP Toulouse)

Discipline ou spécialité
Science et Génie des Materiaux

Présentée et soutenue par
Aneesha O ct{''Varghese
Le 19 Avril, 2012

Titre
Relation between structure and properties of TiO2 coatings on metallic substrates

---

Ecole doctorale
Sciences de la Matière (SDM)
Unité de recherche
Centre Interuniversitaire de Recherche Ingénierie f gu'Materiaux, CIRIMAT

Directeur(s) de Thèse
Dr. Pierre ALPHONSE
Dr. Claire TENDERO

Rapporteurs
Dr. Michel LANGLET
Dr. Pascal TRISTANT

Membre(s) du jury

Dr. Pascal FLOQUET	Professeur, Université de Toulouse	Président
Dr. Michel LANGLET	Directeur de recherche, CNRS (Grenoble)	Rapporteur
Dr. Pascal TRISTANT	Professeur, Université de Limoges	Rapporteur
Dr. Vincent ROUESSAC	Chargé de recherche, CNRS (Montpellier)	Examinateur
Dr. Pierre ALPHONSE	Ingénieur de recherche, CNRS (Toulouse)	Directeur de thèse
Dr. Claire TENDERO	Maître de conference, ENSIACET (Toulouse)	Co-directrice de thèse

Acknowledgements

The culmination of three years work, 19 April, 2012 will go down as one of the most memorable days of my life. It is almost impossible to get here by yourself therefore at this point I would like to take some time to thank the various people who have been there for me when the going got tough.

Contents

Introduction

Since the dawn of time, mankind has found ways to change its environment to suit its needs. In recent years, there has been a gradual awakening to the fact that these changes have started to take their toll on the environment. The various problems faced on a global scale today range from over-population to global warming. Different research groups, all over the world, have taken it upon themselves to find ways to mitigate the numerous issues facing both man and his environment.

With the rise of factories and industries comes the inevitable pollution (by SO_2, NO, NO_2, CO, Pb, As, Hg, etc.) of the surrounding water, air and soil. To counter this problem, various measures have been taken, such as filtration techniques to purify water and air and thermal remediation to purify soil. While filtration techniques have done an admirable effort in alleviating water pollution, the fact is, these techniques only filter the problem, that is to say, the problem still exists. To this end, the decontamination of water-pollutants by photocatalysis (under UV light), primarily using titanium dioxide has become a popular method. This method is popular for many reasons, namely, the decomposition of the pollutants, the low-cost and the easy synthesis of titanium dioxide. Research is being conducted into making this technology more efficient and more economical, such as improving the properties of titanium dioxide so it may be efficient under sunlight and finding ways to lower the synthesis cost so it may be available to a larger percentage of the general population.

Now, coming to the definition of the objective of this study; it may be broadly classified under two divisions, one concerning a way to determine clearly the properties of titanium dioxide coatings that play the most significant role in photocatalysis and the other, to find an environmentally friendly procedure to synthesize titanium dioxide.

Chapter 1 will commence with a discussion on photo-induced phenomena, with an emphasis on photocatalysis. This will be followed by an introduction on the material under investigation, i.e. titanium dioxide (TiO_2); its role in photocatalysis and the various synthesis procedures used, especially the two procedures used in this study, namely, sol-gel and chemical vapour deposition (CVD). The motive behind employing these two techniques

was to produce TiO_2 with a wide range of morphologies with similar polymorphic composition. The goal here was to determine the effect of these properties on the photo-induced activity (photocatalytic activity, in this case) of TiO_2.

Chapter 2 will describe the experimental set-up, characterization techniques and statistical tools used in this study. The precursor for both techniques was the same, titanium (IV) isopropoxide, as were the substrates that were utilized: Si(100) and stainless steel. TiO_2 coatings and powders synthesized during this study were characterized by the following properties: crystalline composition, crystallite size, specific surface area, roughness, thickness, zeta-potential (sol). Two statistical tools were exploited in this study,

1. Design of experiment (DoE) - This was employed during the synthesis of CVD coatings to determine, quantitatively, the relationship between the process parameters and final coating properties.

2. Principal component analysis (PCA) - This was utilized to aid in the analysis of the properties of all coatings (sol-gel and CVD) to determine the properties that were the most crucial for photocatalytic activity.

Chapter 3 will discuss the results obtained from the synthesis of an environmentally friendly sol, as well as the relation between the process parameters and the CVD coating properties, via DoE . In the case of sol-gel synthesis, most of the sols used in various reported procedures have shown very limited stability (<24 h). It should be highlighted that, when scaling-up the production of TiO_2 coatings, long term stability of the sol is crucial in order to achieve reasonable reproducibility. Amongst the vast number of studies dealing with TiO_2 synthesis by the sol–gel process, very few were interested in the long term stability of the nanoparticle dispersion in water. Therefore, before proceeding to establish the relationship between the structural and functional properties of TiO_2 coatings, a study was conducted on the relevant processing parameters required to easily prepare highly stable TiO_2 hydrosols suitable for coatings. From various data available in literature and experimental data from this study, an investigation was conducted into the effect of the main synthesis parameters on the size, the organization and the stability of TiO_2 hydrosols. First, the optimum processing parameters required to prepare highly stable sols composed of ultrafine nanoparticles were chosen. This was followed by the assembly and control of these nanoparticles in order to obtain the required properties, i.e. surface area, porosity, thermal stability, etc.

Chapter 4 will discuss the use of an experimental methodology called Design of experiments (DoE). In the case of CVD, three studies had already been conducted (in CIRIMAT, Toulouse) on TiO_2, synthesized under different conditions, and so, in this study the goal

was to put into place an experimental methodology (DoE) that would determine the relation between the process parameters and coating properties, with a minimum number of experiments, while at the same time covering a large experimental domain.

Chapter 5 consists of the results obtained on the properties of the coatings, by both techniques. The first set of analyses was performed by plotting the properties, individually, with respect to the photocatalytic activity of the material. The second set of analyses was performed using PCA as it allowed for a better interpretation of the data when compared to the he first set.

Chapter 1

Literature Review

Contents

A *photo-induced process* is one, wherein a semi-conductor is excited by a photon source whose energy is greater than the band-gap energy of the semi-conductor. When these photons interact with the semiconductor, an electron passes from the valence band (VB) into the conduction band (CB) leaving behind a hole in the VB. These high energy electron-hole pairs are then utilised, either electrically as in the case of solar cells, or chemically as in the case of organic-pollutant degradation. The common denominator amongst the various photo-induced processes is the redox reaction taking place at the semi-conductor surface. These processes are of interest as they have been reported to change the surface properties of the semi-conductor, for example, inducing super-hydrophilicity in titanium dioxide [1].

1.1 Different photo-induced processes

The use of the energy produced due to the excitation of the semi-conductor by a photon source defines the nature of the photo-induced process. A *photovoltaic (PV) cell* is one in which the electrons that are produced, due to excitation of the semiconductor, are harnessed to produce electricity. When the holes, which are produced due to the excitation process, are used chemically to degrade a target (usually pollutant) molecule, adsorbed on the semiconductor surface, the process is defined as a *photochemical catalytic (PC) process*.

The importance of titanium dioxide (TiO_2) begins to manifest itself at this point, as it is one of the most widely used materials in the processes mentioned above, Figure 1.1. In this study, though the focus is on the PC process, the working of a PV cell will also be briefly discussed (Section 1.1.1), as these two phenomena occur concomitantly on the semiconductor surface [1].

1.1.1 Photovoltaic cells

A photovoltaic cell is constructed using a semiconductor that is irradiated with a photon source; often times that source is sunlight. The electrons in the VB of the semiconductor are excited to the CB, which are then removed to an external circuit and in this way used to produce electricity. An important parameter in a PV cell is the lifetime of the electrons in the CB; if the lifetime is too short, then the process is not efficient since more energy has gone into exciting the semiconductor when compared to the electricity produced. To combat this problem, the semiconductors are often doped to increase the lifetime of electron-hole pairs. The doping of the semiconductor occurs either externally, by adding a different element(s) to it or internally, by the presence of defects [1].
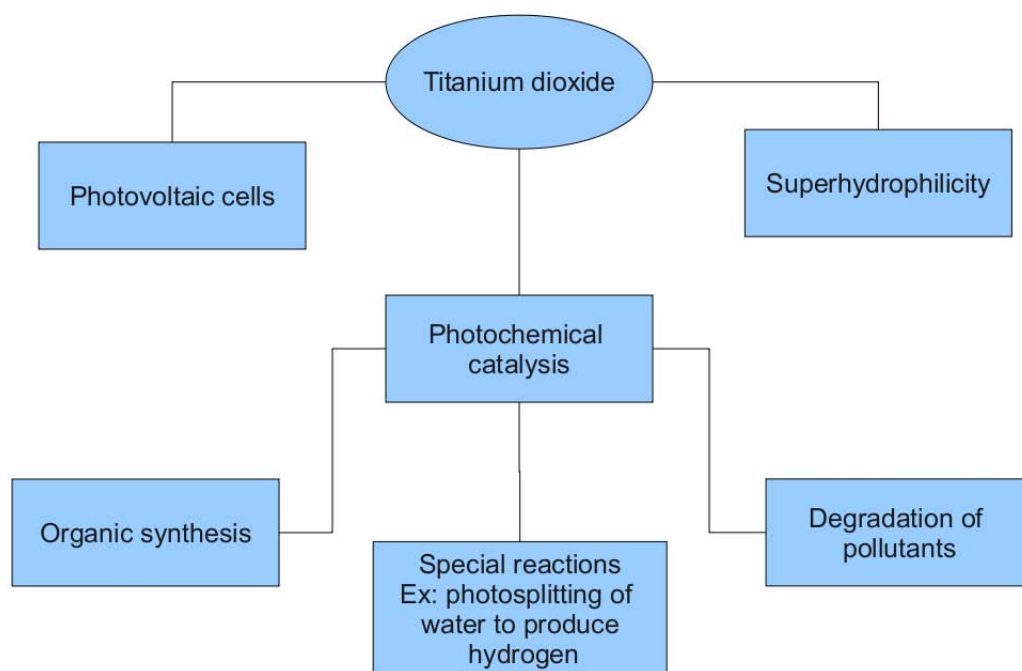
Figure 1.1: Photo-induced processes on Titanium dioxide. Figure adapted from [1].

For the construction of solar cells, the semiconductor that is most often used for commercial purposes is silicon. This is because of the high efficiency that silicon exhibits compared to other semiconductors. But, despite this high efficiency, there are some grave disadvantages to silicon; the need for high purity silicon, and hence, the necessity for its encapsulation to prevent oxidation. These drawbacks incur high costs which is the reason for the high price of solar electricity (five times more expensive than electricity from fossil fuels). While silicon has a higher efficiency than many semiconductors, its theoretical efficiency of 31% is still far from being competitive with the other energy sources available; this low efficiency value is due to unavoidable spectral mismatch, low lifetime of electron-hole pairs and resistance losses. Another high purity semiconductor is GaAs with higher efficiencies than silicon, though despite this seeming advantage it is used more often in space applications because of its high cost (higher than silicon) and the presence of toxic elements [1].

Although a lot of research on silicon based solar cells is directed towards improving its efficiency and developing thin film devices, another way to produce low-cost solar cells is by the use of organic chromophores. This is often called an organic or hybrid solar cell and combines a wide band-gap semiconductor, such as, TiO_2 or ZnO_2, and a photon absorbing dye. The semiconductor is sensitized by the presence of this dye, which when exposed to

a light source, excites the electrons in the semiconductor VB into its CB. The efficiency of flat film organic solar cells is poor, less than 1% [1], which is attributed to the high resistivity of the organic material that leads to ohmic losses. The thickness of the organic material is critical as well, since if it is too thin it will not absorb the light and if it is too thick, the excited electrons can recombine. The literature gives the optimum thickness for most organic compounds to be between 5-20nm [1, 2, 3, 4].

In 1991, Grätzel and O'Reagan created a cell which comprised nanocrystalline (nc) TiO_2 with a monolayer of ruthenium complex dye; the advantage of this 'Grätzel cell', Figure 1.2, was lower resistance losses due to the monolayer and higher surface area due to the use of nc-TiO_2. This increased the efficiency of the organic solar cells to 8% with higher values (12%) being obtained at the laboratory scale. The disadvantage with this cell is the fact that the use of the liquid electrolyte (which regenerates the dye molecules) could lead to leakage or explosions. Hence, commercially this cell is still at the early research stage [1, 5].
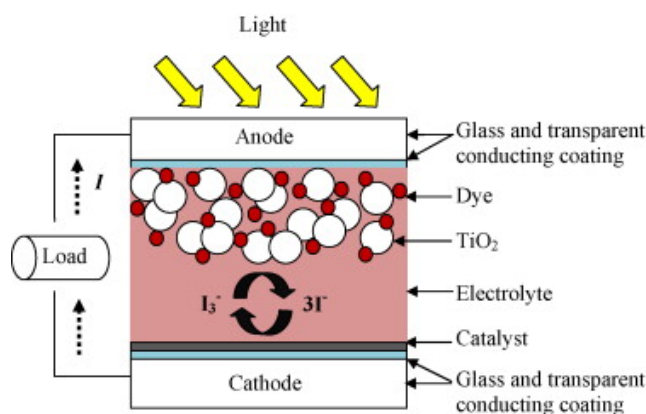
Figure 1.2: Working of a dye-sensitised solar cell [6].

1.1.2 Advanced oxidation process: Heterogeneous photocatalysis

The late twentieth century saw the beginning of a novel advanced oxidation process (AOP) called heterogeneous photocatalysis, now claiming over a thousand articles published annually. This process, has since been utilized in a large variety of reactions, namely, dehydrogenation, hydrogen transfer, air and water purification treatment. An apt definition of a photocatalyst is quoted here, from an article by Jean-Marie Herrmann [7], *"Photocatalysis is based on the double aptitude of the photocatalyst (essentially titania) to simultaneously adsorb both reactants and to absorb efficient photons ($h\nu \geqq E_g$)"*.

The phenomenon may be split into 5 steps that take place sequentially (Figure1.3) as reported by Herrmann et al. [7], :

1. Transfer of the reactants in the fluid phase to the surface,

2. Adsorption of the reactants,

3. At this point, activation of the reaction in the adsorbed phase by the photons (UV or visible irradiation),

4. Desorption of the products,

5. Removal of the products from the interface region.
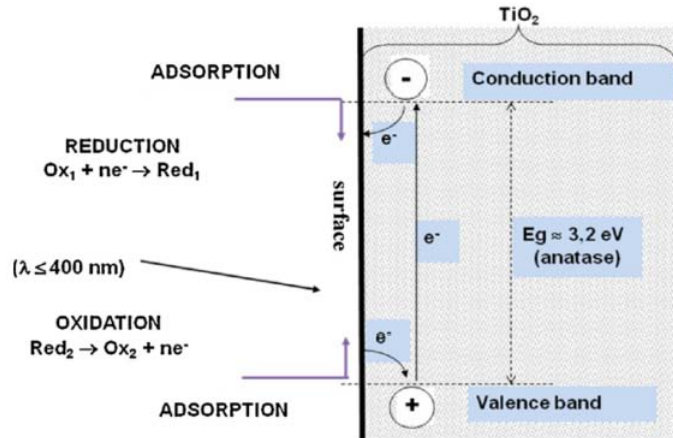
Figure 1.3: Electron energy band diagram of TiO_2 (anatase) [7]

When TiO_2 is irradiated with a photon source whose energy is greater than that of the band-gap of TiO_2, it gives up an e^- to the conduction band (equation 1.1). It should be noted that depending on the sign of the Gibbs free energy (Δ G°), the overall reaction may be termed as either photocatalysis (Δ G° = -ve) or photosynthesis (Δ G° = +ve)[1, 7].

$$TiO_2 + h\nu \quad e^- + h^+ \tag{1.1}$$
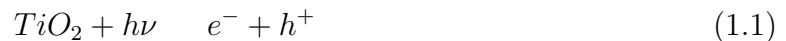
Equations (1.2) to (1.8) trace the possible paths of the different radicals and intermediates formed [7]. The rate determining step in photocatalysis is, typically, the electron transfer to oxygen.

$$O_2 + e^- \quad O_2^- \tag{1.2}$$

$$H_2O \leftrightharpoons OH^- + H^+ \qquad (1.3)$$

$$OH^- + h^+ \quad OH^\circ \qquad (1.4)$$

$$O_2^- + H^+ \quad HOO^\circ \qquad (1.5)$$

$$2HOO^\circ \quad O_2 + H_2O_2 \qquad (1.6)$$

$$H_2O_2 \quad 2OH^\circ \qquad (1.7)$$

or,

$$H_2O_2 + e^- \quad OH^\circ + OH^- \qquad (1.8)$$

The equations (1.9) to (1.11), show the breakdown of the target adsorbed reactant (here R-H) by oxidation due to the radicals formed during the photo-excitation of TiO_2, to give the final end-product(s) [7].

$$R - H + {}^\circ OH \quad R^\circ + H_2O \qquad (1.9)$$

$$R^\circ + {}^\circ OH \quad ROH \qquad (1.10)$$

$$R - OH + {}^\circ OH \quad Intermediates \quad CO_2 \qquad (1.11)$$

To improve the external quantum efficiency of steady state PC processes, which is the percentage of the photons producing an electron-hole pair, it is important to focus on increasing either the charge-carrier lifetime or the interfacial electron transfer [1].

There is some dispute in the scientific community, over the role of VB holes; some [8] suggest that they are directly responsible (before trapping) for the degradation of organic compounds, while others [9, 10, 11] suggest that degradation occurs indirectly by trapped holes at the surface (surface bound hydroxyls). It is difficult to distinguish between the two mechanisms as both of them produce similar products in oxygenated aqueous solutions [1].

It is commonly reported that for the photodegradation process to occur, the target

molecule (TM) *has* to be adsorbed on the semiconductor (SC) surface [1]. On the other hand, there are some studies that report that while adsorption of the TM will increase the rate of the degradation process, it is not a pre-requisite [12, 13]. This is because the OH radicals can diffuse into the fluid phase and react with the TM. In conclusion, while there seems to be some contradiction in the reports obtained regarding the necessity for adsorption of the TM, it does appear to be clear that the rate of degradation increases when adsorption occurs, and therefore is an important factor in the PC process.

The law that is commonly used to determine the reaction kinetics in a fluid phase PC process is the Langmuir-Hinshelwood (LH) law (equation 1.12) [14, 15, 16, 17]. It should be noted that due to the complexity of the reaction mechanism, there is some difficulty in developing a model for the entire PC process [1].

$$R_i = k(S)\theta = -\frac{d[S_i]}{dt} = \frac{k(S)K(S)[S_i]}{(1 + k(S)[S_i])} \tag{1.12}$$

where, R_i is the initial rate of substrate removal; θ is the surface coverage; $[S_i]$ is the initial concentration of the organic substrate S; t is the reaction time; k(S) is the Langmuir adsorption constant of S; K(S) is the adsorption constant of S, which measures the intrinsic reactivity of S. There have been variations made to this model over the years by introducing parameters such as the oxygen concentration, light intensity and catalyst dosage. These different models were interested in either the initial formation rate of CO_2 or the initial disappearance rate of organics [18, 19, 20].

1.1.2.1 Factors affecting photocatalysis

There are several factors affecting the degradation rate of the PC process. They are, temperature, UV light intensity, oxygen concentration, catalyst dosage, target molecule (its character and concentration), pH (in aqueous degradation processes), water concentration (gaseous degradation processes), structure and morphology [1].

The *effect of temperature* has been known to have a negligible effect on the degradation rate of the PC process [21], since it is overshadowed by the effect of the transfer rate of interfacial electrons to oxygen [22]. But studies have reported that at higher temperatures, there is an increase in the desorption rate of both the substrates and intermediates from the catalyst, thereby increasing the effective surface area for the degradation process [23]. This leads to the conclusion that while the effect of temperature is negligible at room temperature, it does seem to affect the degradation rate at higher temperatures ($> 75\,°C$).

The *UV light* used has two possible effects on the degradation process depending on its intensity; at photon fluxes lower than 25 mW/cm^2, the electron-hole pairs are used towards PC process chemical reactions, whereas, at higher intensities the recombination

rate of electron-hole pairs is dominant [24, 25, 26, 27, 28, 29].

The *oxygen concentration* has a favourable effect on the degradation rate of organic compounds because of its electrophilic nature which tends to prevent electron-hole pair recombination. Nevertheless, over a certain optimum level of oxygen the effect turns unfavourable possibly because of the increase of the hydroxyl layer on the SC surface which prevents the adsorption of target molecule(s) at active sites . For example, an oxygen concentration of over 1000 ppmv, showed little effect on the breakdown of the target molecule, in this case tricholoroethylene [24, 30, 31, 32, 33].

The *effect of catalyst loading* is quite similar to that of oxygen concentration; the degradation process increases with catalyst loading up to an optimum point (0.15 - 8 g/l) [34, 35, 36, 37], after which there is a decrease in the degradation process. This is because up to the optimum point, the increase in the catalyst load increases the surface area (more active sites) available for the adsorption of the TM. After the optimum is surpassed the particles of the catalyst contribute to a reduction in the light available due to scattering, which reduces the degradation rate [19, 38, 39, 40, 41]. For semiconductors that are immobilized, the degradation rate increases with thickness as the interfacial area is proportional to thickness for catalysts having thick, porous films, but, there is an optimum thickness beyond which degradation rate decreases due to the increase in the recombination of electron-hole pairs [1].

At high *pollutant concentration* all active sites are occupied (following LH law), and therefore, an increase in the pollutant concentration does not affect the concentration of the pollutants already adsorbed on the catalyst surface, thereby leading to a decrease in the rate constant. There are two mechanisms that occur in series and are potentially rate determining. They are, generation of electron-hole pairs and reaction of these pairs with organic compounds. At low pollutant concentrations, the 2nd mechanism is dominant and the degradation rate is a linear function of concentration, while at high concentrations, the 1st mechanism is dominant and the degradation rate is slower [1].

The presence of *crystallinity* appears to be a pre-requisite for good photocatalytic activity since it was reported that amorphous TiO_2 has negligible photocatalytic activity [42]. The effect of *crystallite size* is important as changes in the crystallite diameter alter the surface/bulk ratio significantly, thereby changing the volume and surface electron-hole recombination rate [1]. The effect of *surface area* appears to be unclear at this point with conflicting reports from various groups. The surface area (SA) of the catalyst is often reported to be the determining factor in many photodegradation processes since a large SA allows for more TM to be adsorbed leading to a higher degradation rate [43, 44, 22, 45, 46, 47, 48]. On the other hand, semiconductors in powder form with large surface area are usually accompanied by crystalline defects, which lead to higher recombination rate of

electron-hole pairs, and therefore, lower photocatalytic activity [1].

1.1.2.2   Photodegradation efficiency determination

It is usually difficult to compare the photo degradation efficiencies reported by various research groups due to the difference in experimental parameters. To overcome this problem, the degradation efficiency is often expressed in terms of quantum yields, turnover number (ratio between pollutant degraded to catalyst used) and electrical energy per mass or per order, instead of percentage of degradation [49, 50, 51, 52, 53].

At the industrial scale, the photodegradation efficiency of an adsorbed photon may be evaluated in two different ways; one way is by determining the ratio of the number of molecules either being degraded or products being formed (N_{mol}) to the number of photons absorbed, N_{ph} (by reactants or semiconductor photocatalyst) [1]:

$$\Phi_{overall} = \frac{N_{mol}}{N_{ph}} = \frac{\textbf{rate of reaction}}{\textbf{rate of absorption of photons}} \tag{1.13}$$

Another way is to measure the photonic efficiency, which is defined as the ratio between the number of reactant molecules transformed or product molecules formed to the number of photons incident inside the front window of the cell at a given wavelength:

$$\xi = \frac{N_{mol}}{N_{ph}} = \frac{\textbf{transformed/produced}}{\textbf{incident inside reactor cell}} \tag{1.14}$$

1.2   Titanium dioxide

1.2.1   Crystal structure and properties

TiO_2 exists as different polymorphs in nature, namely: anatase, brookite, rutile and $TiO_2(B)$. The synthetic polymorphs that are produced from rutile at high pressures are $TiO_2(II)$ and $TiO_2(H)$. Amongst all the above forms, the anatase and rutile forms are most often studied, Figure 1.4. Both these forms consist of TiO_6 octahedra linked in a tetragonal structure. In the rutile phase, two TiO_6 units are present in a single tetragonal unit cell. The Ti ion has a coordination number of 6 and is connected to O via two long (1.976Å) and four short (1.946Å) bonds, at 15 K. In the anatase phase the octahedra are significantly distorted and consist of four TiO_6 units in a single tetragonal unit cell, where Ti is connected to O via two long (1.979Å) and four short (1.932Å) bonds[54].

The control of the transformation of anatase to rutile is important as final applications are quite often phase specific (either anatase or rutile) such as: pigments in paint, photocat-
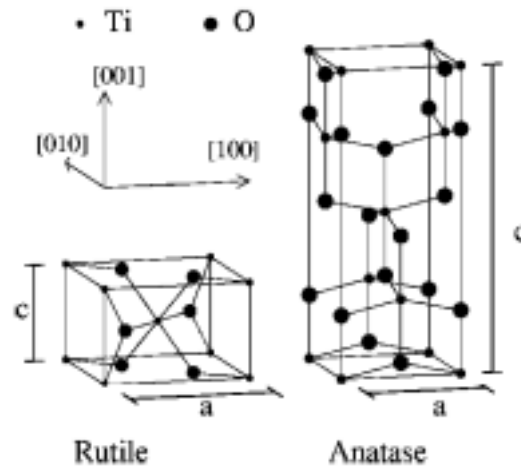
Figure 1.4: Polymorphs of TiO$_2$ [54]

alyst, or as ceramic membrane material [55, 56, 57]. At normal pressure and temperature, anatase and rutile are relatively similar in their stability, as shown by the small differences in the Gibbs free (4-20 kJ/mole) energy, with rutile being the most stable. The transformation from anatase to rutile is affected by varying the temperature or pressure and is influenced by the lattice and surface defects present, as well as, the crystallite size. Rutile transformation rate is enhanced by the increase in surface defects which act as nucleation sites. Experimental results report that when crystallites have small diameter (below 10 nm) anatase is preferentially formed rather than rutile. This is possibly due to the fact that anatase has lower surface energy than rutile. An increase in the diameter to above 35 nm leads to preferential growth of rutile [1, 54, 58].

1.2.2 Role in photocatalysis

O.Carp et al. [1] state the following characteristics for an ideal photocatalyst:

1. *chemically and biologically inert,*
2. *photocatalytically stable,*
3. *easy to produce and to use,*
4. *efficiently activated by sunlight,*
5. *able to efficiently catalyse reactions,*
6. *cheap, and,*
7. *without risks to the environment and humans.*

The semiconductor that comes closest to having the above-mentioned criteria is TiO$_2$. The main drawback in using TiO$_2$ is its lack of absorption in the visible region of the electromagnetic spectrum [1].

The indiscriminate, high-potential (2.80V) oxidizing agents (holes and HO° radicals) produced when TiO_2 is irradiated with light are widely used to photodegrade environmental pollutants such as organics, bacteria, fungi, viruses into harmless products such as CO_2, H_2O and other harmless inorganic molecules [17]. This indiscriminate behaviour of the TiO_2 catalyst has to be controlled in certain applications to prevent undue damage, in such cases as cosmetics [59], where UVC-induced pyrimide dimer formation damages DNA cells and in paints to prevent chalking due to loss of pigments [60, 61, 62, 63, 64, 65, 66].

From a thermodynamic point of view, anatase and rutile are both capable of initializing photocatalytic oxidation because of the similarity in their valence band. But despite this, studies show that the anatase form has been identified as the more efficient photocatalyst of the two forms [67]. A possible explanation could be due to the lifetime of the charge carriers which has been shown to be longer for anatase when compared to that of rutile [68]. Other studies show that a mixture of anatase and rutile to be a better photocatalyst than anatase by itself. This has been explained to be the result of a possible synergetic effect due to the combination of the two phases [69]. In a study by Kurkin et al. [70], the photocatalytic degradation of acetone in the gaseous phase increased with the rise in calcination temperature reaching a maximum activity at 450 °C. This could be due to the increase in the number of charge carriers at the crystallite surface as a result of improved crystallinity. After 450 °C, there was a decrease in activity which is possibly due to the growth in crystallite size leading to a loss in specific surface area. The difference in efficiency between the two phases may be attributed to different parameters as well, such as: charge carrier mobility in the matrix of the material, crystallite size, specific surface area and absorption of the photons which is affected by crystallite size and texture of the material [1].

A few major accomplishments in photocatalysis using TiO_2 include: the splitting of water by Fujishima and Honda, in 1972, with the very first photoelectrochemical cell comprising of a rutile photoanode and a Pt counter electrode [71]; the mineralization of organic pollutants by Ollis, in 1983, using semiconductor sensitized reactions [72, 73], the production of an efficient solar cell comprising of nc-TiO_2 by Grätzel and O'Reagan, in 1991 [74]; superhydrophilic TiO_2 surfaces by Wang et al. in 1998 [75], etc.

Besides its importance in photocatalysis, TiO_2 is used in various other applications, such as: gas sensors (electrical conductivity changes with the ambient gas composition) [76, 77, 78, 79], biomaterials (haemocompatible with the human body) [80, 81, 82]. The rutile phase is used as a dielectric material due to its high dielectric constant($\varepsilon > 100$) [83, 84]. In solar cells, the anatase phase is reported to be preferred to the rutile phase as it is the lower temperature phase, has higher electron mobility, lower density, and lower dielectric constant [1].

1.2.3 Synthesis procedures

The different forms (powder, thin films, crystals) of TiO_2 can be prepared by two distinct routes [1], namely:

1. Solution route synthesis

2. Gas phase synthesis

Solution route synthesis

This route is often used to synthesize thin films of TiO_2 because of its ease and convenience. It allows for control over stoichiometry and homogeneity, formation of complex shapes as well as the synthesis of composite materials. The disadvantages of this route lie in its cost, processing time as well as presence of impurities, such as, carbon. Some of the commonly used solution route synthesis methods are explained briefly here:

1. Precipitation(co-)methods

2. Solvothermal methods

3. Microemulsion methods

4. Combustion synthesis

5. Electrochemical synthesis

6. Sol–gel methods

Gas phase synthesis

This route specializes in forming coatings to alter different properties, such as the mechanical, electrical, thermal, optical, corrosion resistance, and wear resistance properties, of various substrates. They can be also be used to form composite materials by the process of infiltration. The different gas phase methods are:

1. Chemical vapour deposition (CVD)

2. Physical vapour deposition (PVD)

3. Spray pyrolysis deposition (SPD)

4. Molecular beam epitaxy

In this study, the sol-gel method and the CVD method were chosen to synthesize TiO_2. The main reasons behind choosing these two techniques were,

1. to obtain different morphologies of TiO_2,

2. availability of expertise and apparatus,

3. possibility of comparing data with previous studies performed on the same apparatus.

1.2.4   Sol-gel synthesis

Sol-gel processing is not a recent technology, rather, its use at the laboratory scale can be traced back to the mid-1800s when Ebelman [85, 86] reported his results on making monolithic optical lens from silica gels that were synthesized by the sol-gel process. At that time while this received scientific interest, the technological interest was low due to high drying times (1 year) that were required. The interest in this process was recaptured in the late 1800s with the formation of Liesegang rings from gels [87, 88]. Since then, various research groups have recognized the potential of this process to produce gels with high chemical homogeneity [89, 90, 91, 92], control in morphology and size [93] and uniform distribution of crystallite size [94].

The definitions of certain commonly occurring terms in the sol-gel process are mentioned here, with the aid of the textbook on sol-gel science by Brinker and Scherer [95]. A *sol-gel process* as depicted in Figure 1.5, is broadly defined as a wet chemical technique [96] that is used to prepare a ceramic material from either organic or inorganic precursors.

This section will focus its attention on one of the most commonly used precursors: metal alkoxides, which have a organic ligands attached to a metal or metalloid atom. Their popularity arises out of their high reactivity with water. The term *ceramic* is an 'umbrella' that covers all materials that are either metal oxides, nitrides or carbides, both crystalline and non-crystalline. A *sol* is defined as a colloidal suspension of solid particles(1-1000nm) in a liquid, that is dominated by short range forces such as Van der Waals forces and surface charges. A *gel* consists of two phases having colloidal dimensions; a continuous liquid phase enclosed by a continuous solid skeleton [95]. A gel is grown from, either, mechanical mixing of discrete colloidal particles at a pH that prevents precipitation, or, from an interconnected 3-D network formed during the hydrolysis and polycondensation of the precursor [98]. The different routes that can be followed to obtain sol-gel monoliths are depicted in Figure 1.6 [99, 100]. The resultant product obtained when a gel is dried under ambient conditions by evaporation is called a *xerogel*. The volume of these xerogels are usually 5 to 10 times less than the original gel. If the gel is dried in an autoclave,
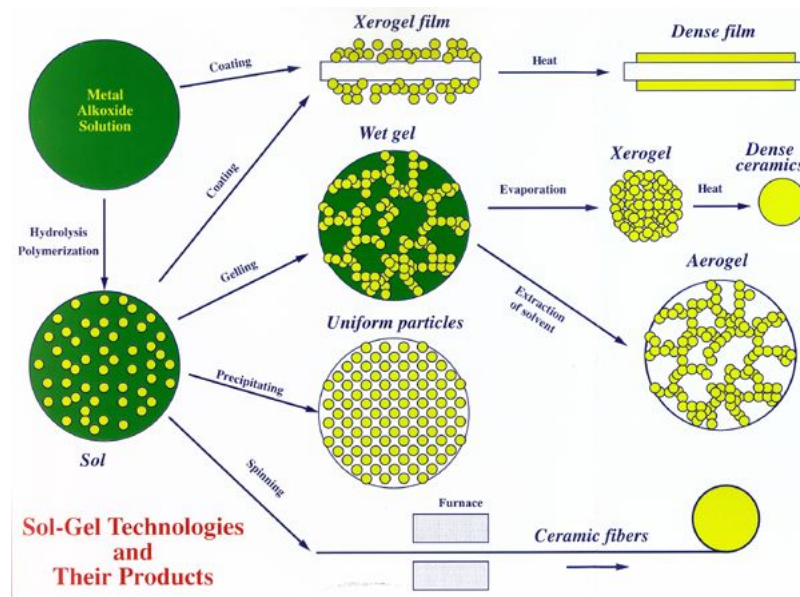
Figure 1.5: Sol-gel process [97].

the resultant product is called an *aerogel*. An aerogel has almost the same volume as the original gel, due to the absence of capillary pressure while drying [95].
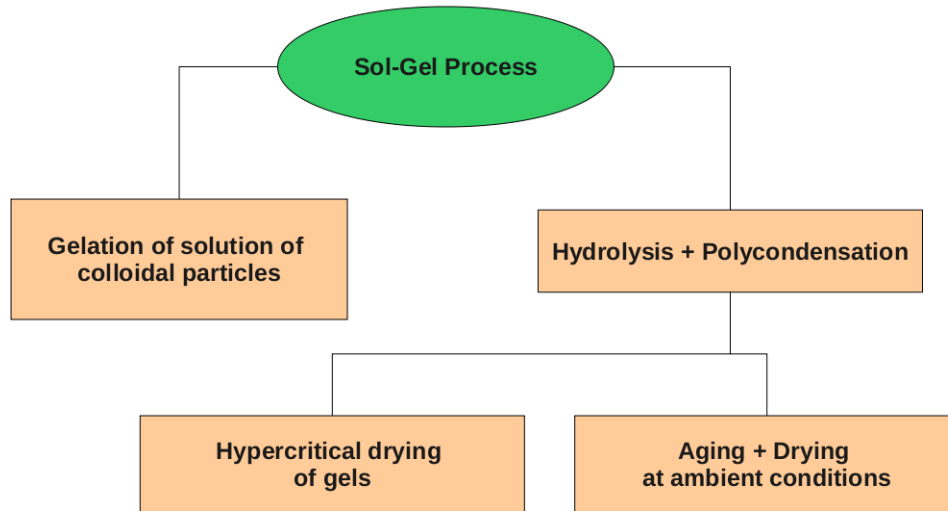
Figure 1.6: Sol-gel routes to obtain monoliths adapted from [98, 96].

1.2.4.1   Reaction mechanism

As shown in Figure 1.6, the structure of the gel depends on the gelation route. For gels obtained by the hydrolysis and condensation route, the structure depends heavily on the kinetics of these reactions. The processes that succeed this step, such as ageing, drying,

stabilization and densification, rely on the gel structure [98]. For example, in reactions involving metal alkoxides, the hydrolysis and condensation reaction mechanisms occur by nucleophilic addition, followed by a transfer of protons from the attacking molecule to an alkoxide [95].

$$M(OR) + H_2O \quad M(OH) + RO - H \tag{1.15}$$

The protonated species are finally removed as either alcohol (alcoxolation), equation 1.16, or water (oxolation), equation 1.17 [95].

$$M(OH) + M(OR) \quad M(OM) + RO - H \tag{1.16}$$

$$M(OH) + M(OH) \quad M(OM) + H_2O \tag{1.17}$$
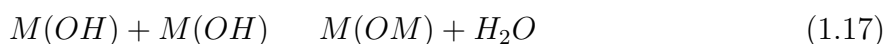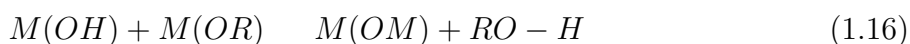
Hydrolysis and condensation kinetics are influenced by the size and electron-giving/taking *ability of the organic ligand.* In titanium n-alkoxides ($Ti(OR_n)_4$), the increase in the length of the alkyl chain leads to a decrease in the hydrolysis kinetics, possibly due to the steric effect [101, 102]. The effect of the organic ligand on the condensation kinetics has been qualitatively illustrated by observations that, for large values of R, stable sols are obtained while for small values of R, precipitates are formed even under mild hydrolysis conditions. It has been suggested that oligomeric species are initially formed and then eventually aggregate to form gels or precipitates. The influence of R on the oligomer species has been observed; the larger the size of R, the smaller is the oligomer. Therefore, in addition to its effect on the kinetics, the R group also affects the crystallite size, surface area and by its influence on the size and structure of the primary oligomers, the crystalline behaviour of the gel [101, 103, 104, 105, 106, 107, 108, 109].

The formation of a stable TiO_2 sol [110] is schematically depicted in Figure 1.7, where the hydrolysis of the precursor is followed rapidly by the condensation, nucleation and growth of primary particles. These primary particles aggregate quickly to form large agglomerates that slowly over time undergo peptization, which is observed by the formation of a translucent sol (disappearance of precipitates). There is a competition between the rate of peptization and rate of re-agglomeration and in the case of an unstable sol, the rate of agglomeration dominates, leading to precipitation.

The stability of a colloid is indicated by its *zeta potential*, which is related to the overall charge a particle acquires in a specific medium. When the zeta potential is low then the particles of the colloid tend to aggregate, as there is no force keeping them apart, while a large zeta potential (either negative or positive) leads to a repulsion between the colloidal particles. Therefore, the magnitude of the zeta potential is an indicator of the stability of
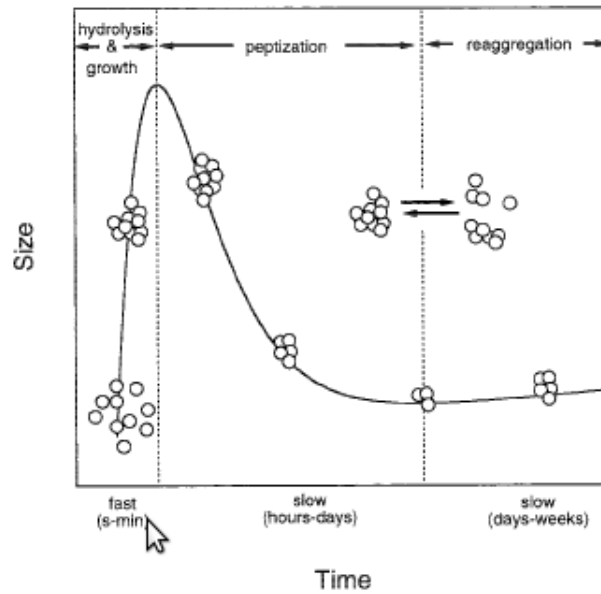
Figure 1.7: Schematic of formation of TiO$_2$ sol [110]

a sol. Typically, sols with zeta potentials lower than -30 mV and higher than 30 mV are considered stable (Figure 1.8) [111]. For a given material, the factors affecting the zeta potential are the pH of the sol and the nature of the electrolytes in the solution [96].
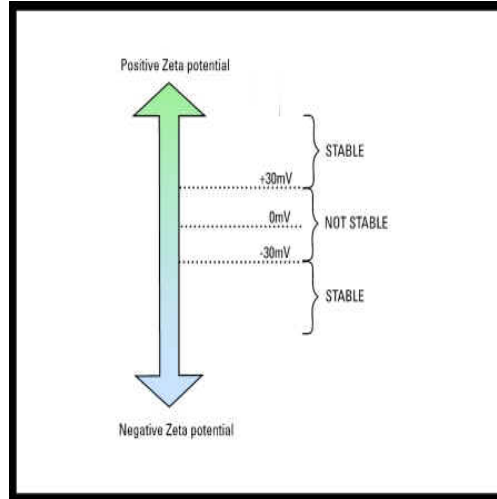
Figure 1.8: Effect of zeta potential on sol stability [111]

1.2.4.2 Factors influencing properties of TiO$_2$ sol

The effect of the *water to alkoxide ratio (r)* is important to control the size, stability and morphology of the TiO$_2$ sol particles. It has been observed that for low r (< 10) values the particles are predominantly spherical (0.5-1μm) and relatively mono-dispersed

[112, 113, 114, 115], whereas, for higher r values, unstable colloidal particles ($<$100 nm after peptisation) that tend to agglomerate, are formed [116, 117, 118].

The *temperature* of the hydrolysis step affects the particle size of the colloid as reported by Vorkapic et al. [110] in a study involving different alkoxides of titanium, Figure 1.9. The same study also reports that the peptization temperature has the strongest impact on the crystallite size, when compared to other parameters such as nature of alkoxide, hydrolysis temperature and nature of alcohol, Figure 1.10. The hypothesis put forth by the authors [110] to explain the crystallite dependence on temperature is that there are two competing mechanisms working on the colloidal particles: the peptization mechanism which results in breakdown of large agglomerates into smaller clusters or primary particles, and the re-agglomeration mechanism which results in the clusters reattaching themselves into large agglomerates. An increase in the temperature increases the peptization rate though there is an optimum temperature after which an increase in temperature leads to a decrease in the solvent dielectric constant which lowers the electrostatic barrier and favours agglomeration.
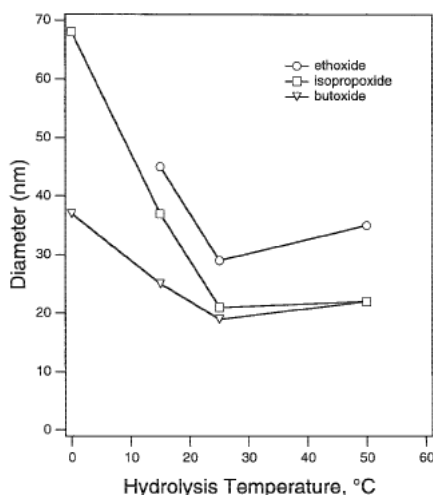
Figure 1.9: Effect of temperature on hydrolysis [110]

It has been reported that the particle size is affected (becomes smaller) in the *presence of acid* during hydrolysis, with smallest particles obtained at [H$^+$]:[Ti] $\sim$ 0.2. At high ratios of [H$^+$]:[Ti], the stability of the sol is adversely affected due to the screening effect of the protonated surface, while at very low acid concentrations, precipitation occurs due to insufficient peptization [116]. The polymorphic composition of the colloidal particles is also affected by the pH of the sol; certain studies report that at low pH, the rutile phase is strongly favoured over the anatase and that at high pH, the anatase phase is favoured over rutile. This is explained via Ostwalds' ripening theory, where the oxide particles, in
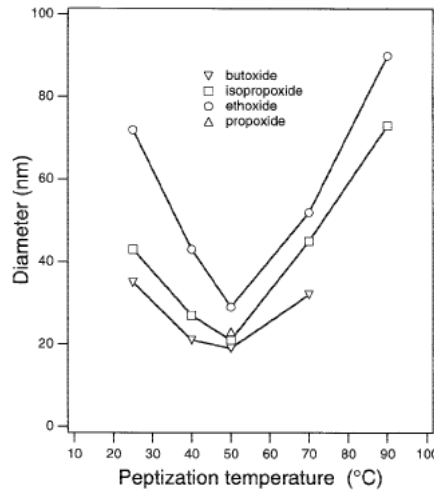
Figure 1.10: Effect of temperature on peptization [110]

a highly acidic environment, undergo a dissolution-crystallization effect and recrystallize into the thermodynamically stable phase, i.e. rutile. At high pH, a relatively amorphous form of TiO_2 is formed, with only the presence of anatase up to a temperature of 600 °C, which turns into a predominantly rutile rich phase, after 700 °C [96].

The addition of alcohol is a standard practise in the synthesis of TiO_2 sols [113, 115, 116, 118] because it aids in slowing the reaction and providing a homogeneous environment for the crystallite growth. At the same time, it has been reported that the presence of alcohol produces crystallites twice as large as those produced when no alcohol was used in the synthesis [110].

1.2.4.3 Coating techniques

The standard techniques used to synthesize coatings through the sol-gel process are, dip-coating, tape-casting, spin coating, etc. Some important parameters for a good quality coating are: good adhesion to the substrate, resistance to cracking, and homogeneous thickness [96].

The first commercial thin film coatings by the *dip coating* process were produced in the early 1900s [119, 120]). It is a simple process which consists of lowering the previously cleaned substrate into the sol and then withdrawing it at controlled speeds [96], Figure 1.11. Two mechanisms are at work to produce the films: one is the force of gravity that drains the liquid from the substrate surface and the other is the evaporation of the liquid phase (solvent).The advantage of this process is that, typically, the geometry of the substrate can vary [119]. The parameters that play an important role on the film thickness are the withdrawal speed of the substrate and the viscosity of the liquid. The *tape-casting*

technique is a cost-effective way to produce large-scale ceramic coatings, multi-layered structural composites [121]. Here, the sol is spread over a moving substrate with the help of a stationary blade, Figure 1.12. The expected thickness of the coatings is in the micron range [96]. The *spin coating* technique consists of depositing an excess of liquid over the substrate, then the spin-up stage where the liquid is moved radially, followed by the spin-off stage where the excess liquid is removed as droplets from the perimeter of the substrate, and finally, evaporation of the liquid on the substrate [95], Figure 1.13. The parameters that play an important role on the film thickness are the spin speed, liquid viscosity and spin time [119].
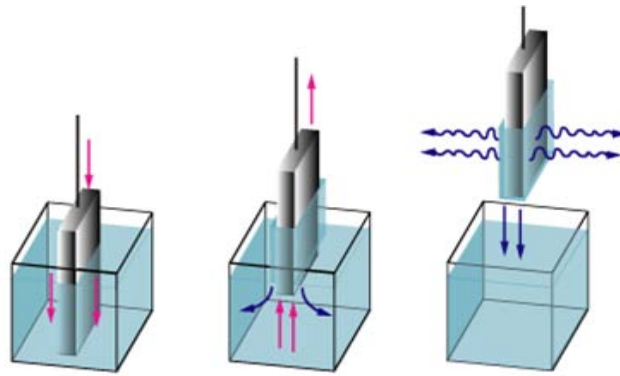
Figure 1.11: Dip coating, Figure from [122]
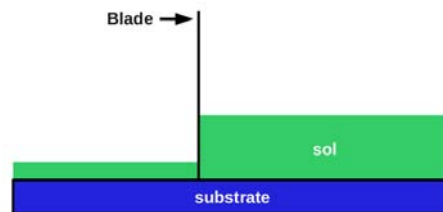
Figure 1.12: Tape casting
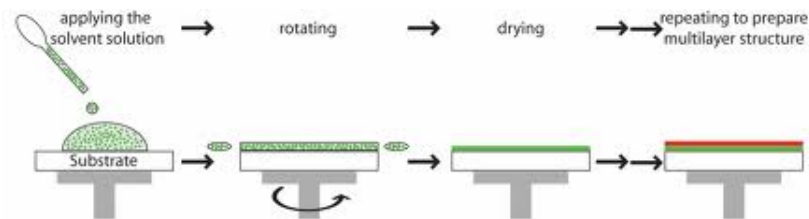
Figure 1.13: Spin coating, Figure from materials [123]

1.2.5 Chemical Vapour Deposition

The Chemical Vapour Deposition (CVD) process is more recent than the sol-gel technique with its debut in the 1940's, as a process to purify refractory metals. In the last couple of decades, the CVD process has carved a niche for itself in the large-scale production of high-performance materials. This is due to its many advantages: high uniformity of coating on complex geometries, epitaxial growth, low-cost and relatively easy deposition control [124].

CVD is defined as any process that involves the formation of thin solid films, on a substrate, by means of chemical reactions of gaseous precursor species. It is these chemical reactions, initiated by thermal energy, that distinguish it from the various physical vapour deposition processes [125].

The advantages of CVD over PVD techniques such as magnetron sputtering, pulsed laser ablation, etc. are indicated below [126]:

1. high uniformity over large area,

2. coverage of geometries with high aspect ratio (Figure 1.14),

3. line-of-sight not required.
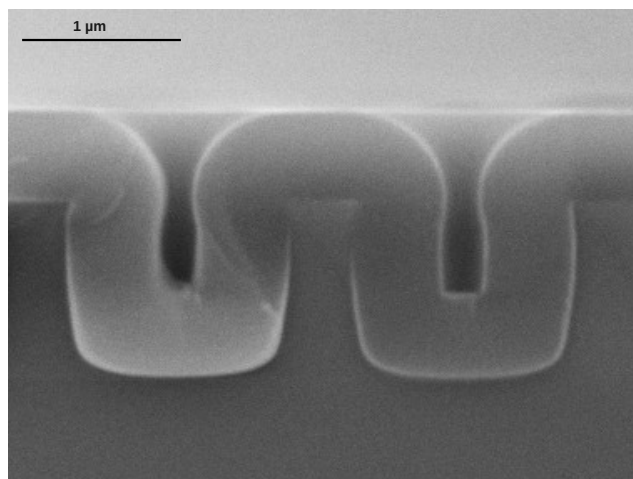
Figure 1.14: CVD coating of Al_2O_3 on Si wafer

The series of sequential steps in a CVD process that was developed by Spear in 1982 is depicted in Figure 1.15 and summarized by Yongdong Xu et al. as follows [125] :

1. The mass transport of the gaseous precursor species to the substrate,
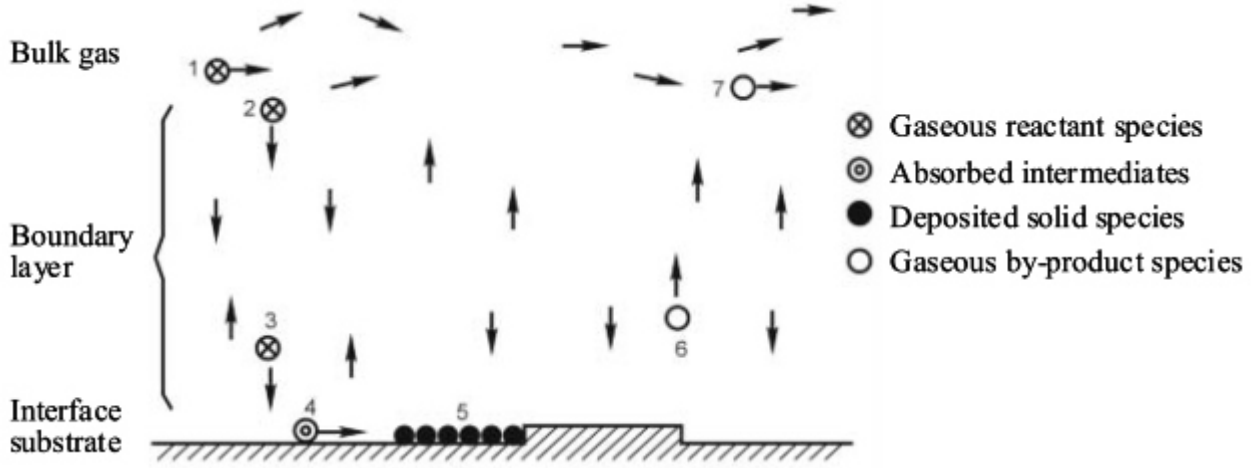
Figure 1.15: Sequence of steps in a CVD process [127]

2. Diffusion of the precursor species to the substrate or formation of intermediates in the gaseous phase,

3. Adsorption of precursor species or intermediates onto the substrate surface,

4. Surface migration, heterogeneous reaction, inclusion of coating atoms into the growing surface, and formation of by-product species,

5. Desorption of by-product species,

6. Diffusion of by-product species to the bulk,

7. Transport of by-product gaseous species away from substrate (exhaust gases).

The most important factors concerning growth rate of CVD coatings are the mass transport and the surface reactions. At high temperatures, another factor comes into play, and that is the thermodynamics of the precursor reaction.

The factors affecting the mass transport are: pressure gradient, temperature gradient and concentration gradient. The reaction zone is maintained at a temperature that is higher than that of the entering reactant gases; this gradient in temperature affects the momentum, heat and mass transport of the gases. The laws describing the aforementioned transport phenomena are, Newton's viscous law (equation 1.18), Fourier law (equation 1.19) and Fick's law (equation 1.21), respectively [128].

$$\tau = -\mu \frac{du}{dy} \tag{1.18}$$

$$q = -\alpha \frac{dT}{dy} \tag{1.19}$$

$$J = -D\frac{d\rho}{dy} \tag{1.20}$$

where,

$\frac{du}{dy}, \frac{dT}{dy}, \frac{d\rho}{dy}$ are the gradients of velocity, temperature and concentration, respectively.

μ, α, D are dynamic viscosity, thermal conductivity and diffusivity, respectively.

An Arrhenius plot is, typically, used to represent the kinetics of the CVD coating growth. In figure 1.16 the growth rate is plotted as a function of deposition temperature. There are three distinct regions in the plot attributed to three distinct regimes, namely, chemical surface reactions, mass transfer and thermodynamics, respectively [127]. The growth of TiO$_2$ by MOCVD in this study was conducted in the mass transfer regime.
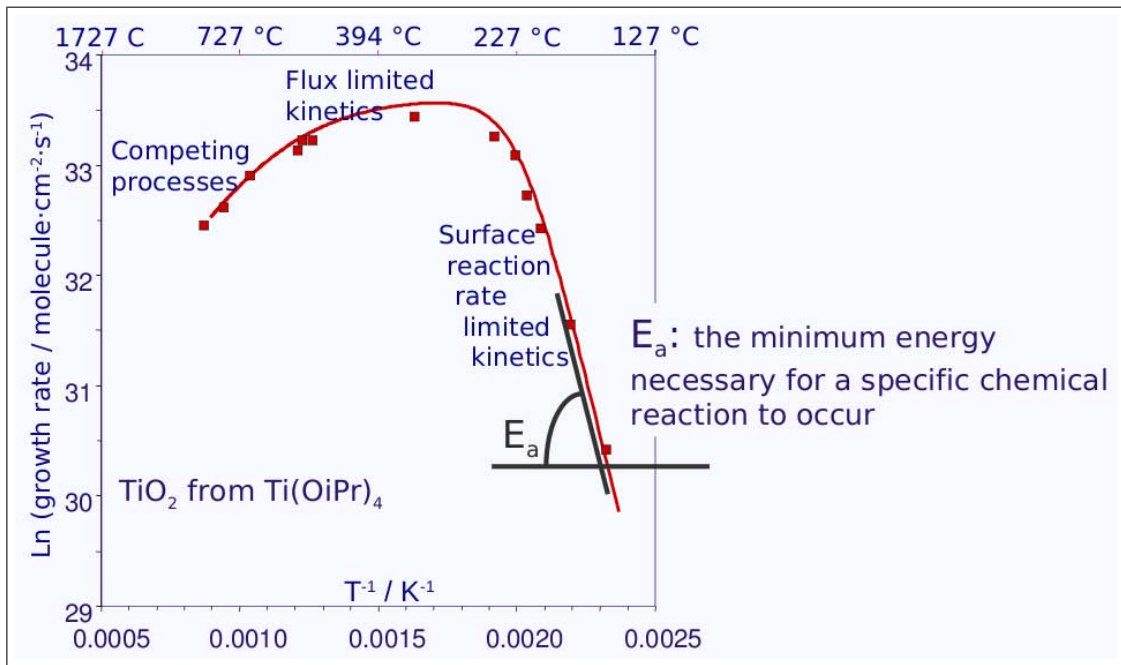
Figure 1.16: Arrhenius plot of different regimes in CVD [129].

1.2.5.1 General factors to consider while choosing a CVD system

The CVD method is classified into different fabrication categories (Figure 1.17) as a function of seven processing parameters, namely: pressure, temperature, wall temperature, precursor nature, deposition duration, activation manner, and gas flow state [130, 131, 132].

The *temperature* of the coating is a significant factor that has to be taken into account, before choosing the CVD system, since certain substrates cannot withstand high temperatures, for example: aluminium in semi-conductor processing.

The *pressure* of the reactor chamber affects the deposition rate and the uniformity of
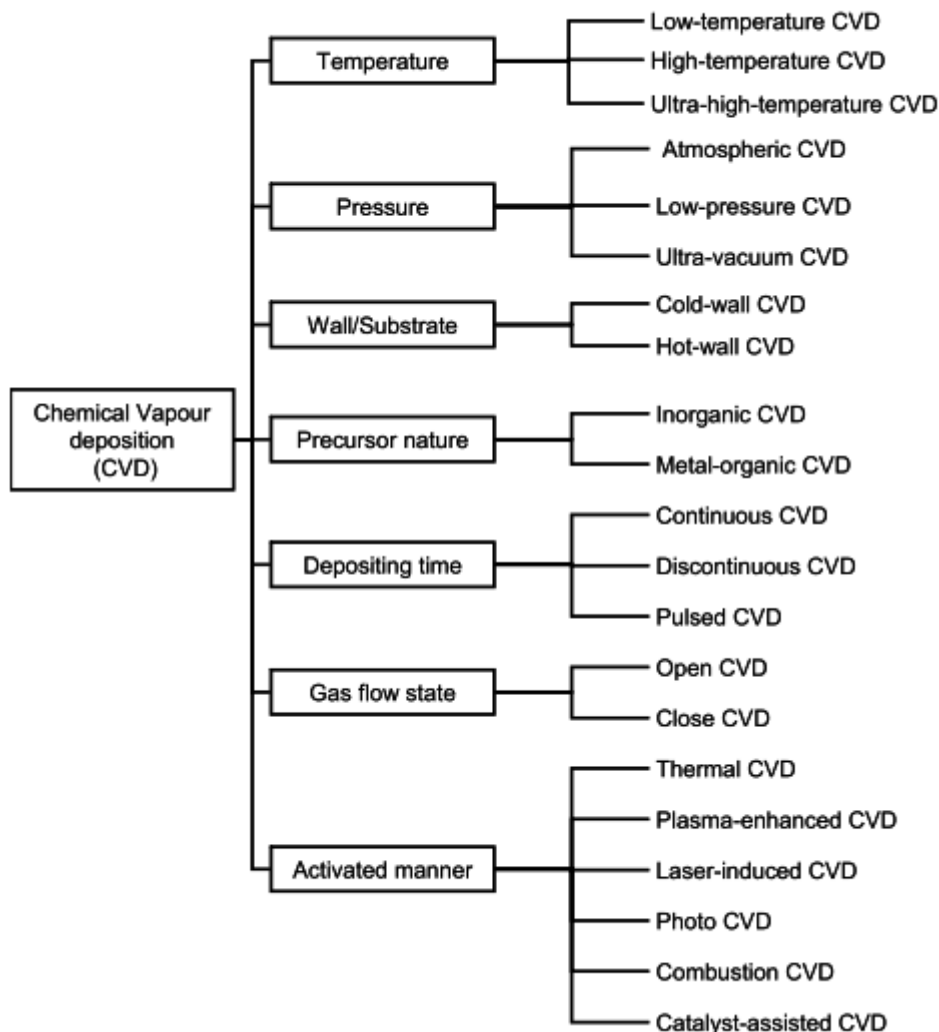
Figure 1.17: Sequence of steps in a CVD process [127]

the coating and hence is an important operational parameter to be considered during the CVD process.

The difference between a cold-wall and hot-wall CVD process configuration is that, in the former, only the substrates are heated, either inductively or resistively, while the walls of the reactor chamber remain cold, while in the latter, the entire reaction chamber is heated from the outside. The advantages of the cold-wall reactor over the hot-wall reactor is the economic use of precursor, homogeneity and uniformity of the coating and efficient use of energy [124].

The CVD process uses both liquids and solids as precursors. These precursors go through either an evaporation or sublimation process before entering the reactor chamber [127]. The precursor can be delivered into the reaction chamber in four ways:

1. Direct vaporisation by itself without carrier gas.

2. Transport by a carrier gas over the liquid surface.

3. Bubbling through the liquid.

4. Liquid injection.

The bubbling method is usually used as it is an easier and reliable method to obtain a uniform mixture of gases immediately. The temperature and liquid precursor level are controlled carefully to improve the reproducibility of the precursor gas flow. The carrier vapour flow rate is given by the following equation [127].

$$F_{vap} = \frac{p_{vap}P_{cyl}}{P_{cyl} - p_{vap}} \frac{F}{RT} \tag{1.21}$$

where,

F_{vap} - mole flow rate in moles/minute,

p_{vap} - saturated vapour pressure of the liquid precursor at bath temperature T_b,

P_{cyl} - total pressure in the precursor cylinder,

F = volume flow rate through the bubbler in litres per minute,

R = constant, and

T = 273 K

The gaseous reactants used in the CVD process are a critical factor and their transport to the substrate has to be controlled in a careful and timely manner. A variation in their transport affects the quality, the deposition mechanism as well as the deposition rate of the coating.

1.2.5.2 Effect of MOCVD process parameters on structural properties

In this study, the precursor used was TTIP and the reactor was a cold-wall reactor in a vertical geometry configuration. The precursor and set-up are detailed, at length, in Chapter 2.

The metal-organic chemical vapour deposition (MOCVD) process has a large number of process parameters that may be controlled to obtain coatings with desired properties [126]. The process parameters that are generally considered to have a significant impact on the growth rate and uniformity of MOCVD coatings are: reactor pressure, deposition temperature, reactant partial pressure, and gas flow rates [133]. Hence, to obtain coatings with controlled structural properties, it is essential to clearly understand the effect of the aforementioned process parameters on growth rate and uniformity.

The typical procedure, to determine the effect of the process parameters, was to conduct numerous experiments from which data was gathered and analysed [134]. This was not only time-consuming but also resulted in an uneconomical use of resources (precursor, carrier and dilution gases, etc.) [135]. To counter this problem, different models (empirical and semi-empirical) were developed, though confined by various restrictions, such as, small range of applicability and sensitivity to reactor design [136, 137]. It is therefore, imperative to develop robust models that can be applied over wider ranges of process parameters and that can be easily tailored to different reactor designs.

Nami et al.[133] have reported on the reaction-controlling mechanisms of TiO_2 coatings synthesized in an inverted vertical impinging jet MOCVD reactor, using TTIP as precursor. They varied the deposition temperature from 423 K to 960 K and ignored gas-phase reactions, since it was previously reported that gas-phase reactions were insignificant at temperatures below 823 K [138], though this might change, at higher temperatures. The impact of these gas-phase reactions is to reduce the growth rate, because with the increase in the number of gas-phase reactions, there is a corresponding decrease in the reactants reaching the substrate surface. If the walls of the reactor are not temperature controlled then the increase in susceptor temperature (deposition temperature) leads to an increase in the reactor wall temperature, thereby increasing the number of gas-phase reactions, finally, resulting in lower growth rate. Figure 1.18 shows that with the increase in the temperature the growth rate increases linearly [126, 133] and this is followed by a decrease at higher temperatures ($\sim$1000K), when the walls are not temperature controlled [133].
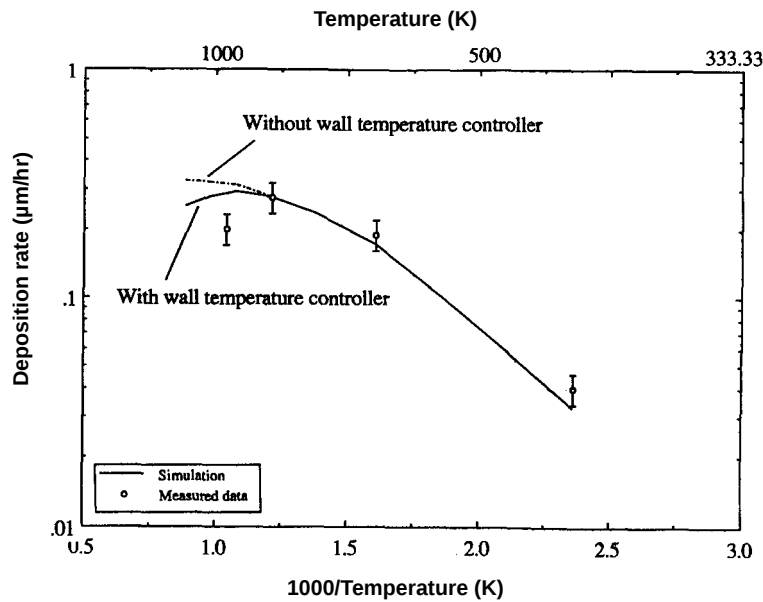
Figure 1.18: Dependance of film growth rate on deposition temperature [133]

In vertical MOCVD reactors, lowering the pressure leads to an increase in the gas inlet velocity, causing an increase in the molar fraction of the reactant species [133]. This does not translate into a higher growth rate since at low reactor pressures, the partial pressure of the precursor gas is low as well. At lower pressures, the reaction rate is dependant on the precursor concentration, while at higher pressures, it is controlled by the mass-diffusion, i.e. the quantity of reactant available on the substrate is the limiting factor. At constant deposition temperature, low pressures are, generally, desired for uniform films [139] as well as purer films, since lowering the pressures reduces buoyancy-driven flows [140]. This reduction in buoyancy flow is desirable since it increases the mass transfer rate of the reactant species to the substrate surface, Figures 1.19, 1.20 [139].
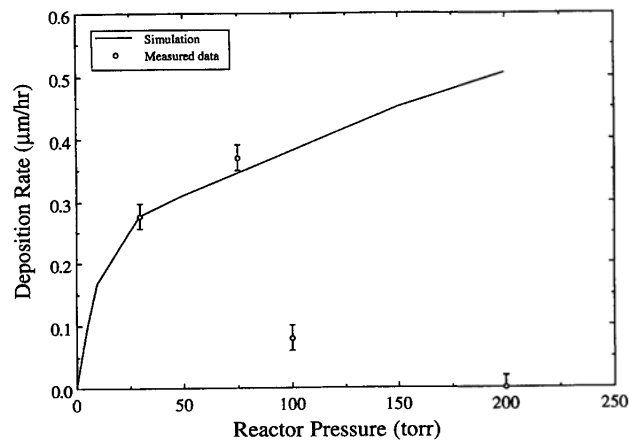
Figure 1.19: Dependance of film deposition rate on reactor pressure [133].
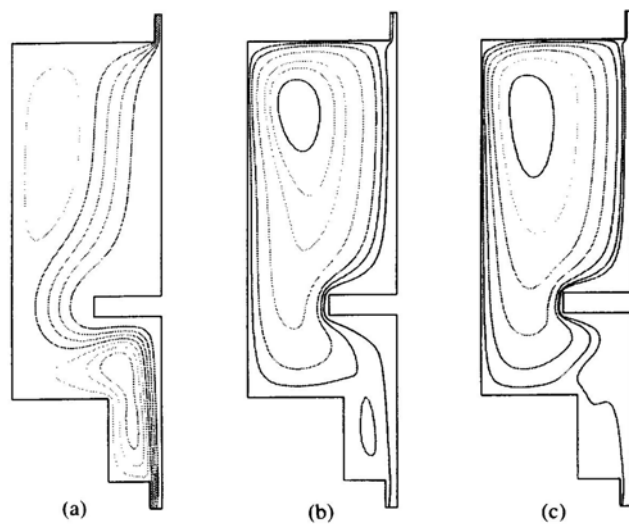
Figure 1.20: Flow patterns at different pressures, a) 5 Torr, b) 50 Torr, c) 100 Torr [133].

At constant molar fraction, an increase in the flow rate of the gas decreases the residence time of the precursor species to reach the substrate. This decrease in residence time allows for a greater concentration of the reactant species at the substrate surface, leading to an increase in growth rate (Figure 1.21) . While higher growth rate and uniformity have been reported at higher total flow rate ($\sim$ 3000 sccm), it should be stressed that a large part of the precursor exits the rector without having taken part in the deposition, and therefore, an increase in flow rate is not considered economically viable. On the other hand, it has been reported by Chou et al. [126] that at lower flow rates (at constant temperature and pressure), there is, in principle at least, a higher probability of the reactant species colliding with each other, thereby potentially increasing the film growth rate. This higher probability in collisions is due to the decrease in other species such as the carrier gas species that could, potentially, interfere with the collision of the reactant molecules.
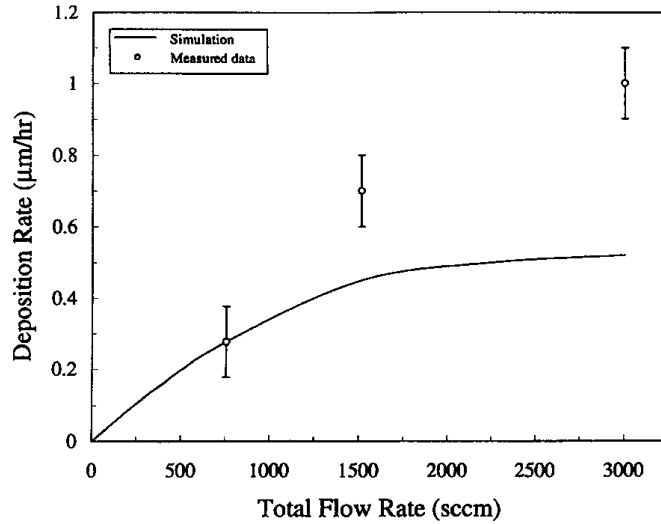
Figure 1.21: Flow patterns at different pressures, a. 5 Torr, b. 50 Torr, c. 100 Torr [133]

The effect of the partial pressure of TTIP on the growth rate may be conducted either by varying the reactor pressure or by varying the reactant inlet mole fraction. The effect of the viscosity of TTIP in the inlet gas mixture on the growth rate of TiO_2 was reported in [133]. The viscosity of TTIP was calculated using kinetic theory.

$$\mu = 2.37 \times 10^{-6} \sqrt{\frac{MT}{\sigma \Omega_\mu}} \tag{1.22}$$

where, σ = collision diameter, M = molecular weight and Ω_μ = collision integral

The effect of the TTIP viscosity on the TiO_2 growth rate at the different control regimes

(kinetic and mass controlled regimes) was similar. The increase in the mole fraction of the reactant species was higher at higher viscosities. And since the TTIP source temperature directly affects the viscosity, the growth rate could be controlled by controlling the source temperature.

1.3 Summary

In this chapter, we have discussed in some detail the different processes resulting from the photo-induced phenomena, in particular, heterogeneous photo-catalysis. We have then proceeded to detail the material under study, i.e. titanium dioxide: its various polymorphs and synthesis procedures. The synthesis procedures of interest in this study are the sol-gel process and the chemical vapour deposition process. The various factors affecting both processes have also been detailed. In the following chapter, we will give details on the precursor(s) used, experimental set-up for both synthesis processes and the statistical tools used to analyse the results.

Chapter 2

Set-up, Characterization, Statistical methods

Contents

2.1 Experimental set-up

2.1.1 Choice of precursor

The standard precursors used to produce TiO_2 are either titanium tetrachloride ($TiCl_4$) or titanium tetraisopropylorthotitanate (or isopropoxide), often denoted as TTIP with the formula of $Ti(O^iPr)_4$ or $Ti(OC_3H_7)_4$. For this study TTIP (Figure 2.1) was chosen over $TiCl_4$ because it is easier to work with, as it is less reactive with water, and also because of the elimination of the presence of Cl ions that are reported to be detrimental to the catalytic activity of the coatings [141] as well as being corrosive to the substrate in this study (stainless steel). The other advantage from the CVD point of view is its strong vapour pressure at low temperature which makes it easy to decompose in the operating conditions used in this study (Table 2.1), and also, as it contains oxygen, there is no necessity for a co-reactant during the CVD synthesis to form TiO_2 thin films [124]. The properties of titanium isopropoxide are mentioned in Table 2.2.
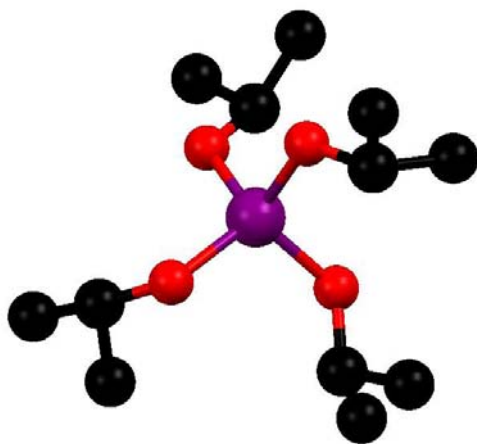
Figure 2.1: Structural formula of titanium tetraisopropylorthotitanate (TTIP).

Table 2.1: Boiling point of TTIP and $TiCl_4$

Precursor	Boiling point ($^\circ$C/Torr)
TTIP	58/1
TiCl$_4$	136/760

Table 2.2: Properties of titanium tetra-isopropoxide [124]

Provider	Aldrich
Purity	97%
Molar mass (g/mol)	284.2
Melting point (°C)	20
Boiling point (°C)	91.35 (5 mmHg); 50 (1 mmHg)
Density (g/cc at 25 °C)	0.995
$\Delta\mathbf{H}°_f$**(liquid) (kcal/mole)**	-377± 1.6
$\Delta\mathbf{H}°_{vapourisation}$**(kcal/mole)**	14.7
Entropy (15 °C) cal/mole °C	40.5

2.1.2   Preparation of substrate

Stainless steel 304L (SS-304L, Anodigrav) (10mm x 10mm x 0.4mm) was the substrate chosen for this study (both in CVD and sol-gel synthesis), as it has a good resistance to oxidation and also because previous studies in the laboratory were conducted on this type of substrate. Si(100) substrates (10mm x 10mm) were also used, but were restricted to MOCVD synthesis, as it's hydrophobic nature made it a difficult substrate to coat by the sol-gel synthesis. The Si(100) substrates were employed to aid in the determination of the polymorphic composition, roughness and thickness of the MOCVD coatings.

Typically, SS-304L substrates were polished with a 600 grit sanding paper, in an attempt to introduce roughness to the substrate to increase specific surface area. Some were also polished with 4000 grit sanding paper (in the case of sol-gel synthesis) for a 'mirror' finish, to conduct Atomic Force Microscopy (AFM) analyses. Substrates to be coated via the sol-gel route were heat treated in an oven for 30 minutes at a ramp rate of 10 °C/min, at specific temperatures (350 °C, 550 °C or 750 °C) depending on the temperature at which the coating was to be heated.

After the SS-304L substrates were polished, they were cleaned (in case of sol-gel coatings, after heat treatment) in an ultrasonic bath with ultra pure water (UPW), then in a commercial alkaline solution (Turco) for 20 minutes at 70 °C, then re-washed with UPW and finally, in absolute ethanol (Merck). They were then dried in an oven at 60 °C. The Si(100) substrates were cleaned in an ultrasound bath in ethanol and then dried in an oven at 60 °C.

2.1.3   Sol-gel: Preparation of stable sol

The motive behind choosing the sol-gel technique in this study was due to its ubiquitous nature and its various advantages: homogeneity, control over the microstructure, ease of

processing, low temperature and the ability to coat large and complex substrates.

The hydrolysis of titanium alkoxide precursors is the most commonly used route to synthesize titanium dioxide (TiO_2) coatings, by the sol–gel process. This route is further classified into two sub-routes, as a function of its processing parameters.

The most common of the two is the polymeric route, where the solvent is most often an alcohol and the hydrolysis is carefully controlled by using a limited amount of water [142, 143, 144, 145, 146, 147, 148, 149, 150, 151]. An acid catalyst (typically, HCl or HNO_3) is added and the alkoxide is complexed prior to hydrolysis, thereby decreasing the reaction rate. The shape and size of the polymeric units are determined by the relative rate constants of the hydrolysis and polycondensation reactions. With this method amorphous films are obtained, which can become crystalline with heat treatment.

The second sub-route uses water as the solvent, which is in large excess with respect to the alkoxide. In these conditions hydrolysis is fast, producing ultrafine primary particles (2 to 8 nm) [152]. These nanoparticles agglomerate very rapidly, giving large aggregates of macroscopic dimensions [153]. Peptization by means of an inorganic acid (either HCl or HNO_3) is used to break down the aggregates and produce a colloidal suspension consisting of particles on the order of 15-100 nm. At this point, the nanoparticles are crystalline and predominantly anatase with 10–30% of brookite [154]. This second route uses a cheap and non-toxic solvent (water) and gives crystalline films with potential applications for coating substrates with low thermal stability (polymers). This route was further explored in this study.

2.1.3.1 Choice in porogen

Porous materials are often synthesized by the addition of porogens such as alkyl phosphate anionic surfactants, quaternary ammonium cationic templates, polyethylene glycol and primary amines. In this study, PEG, $C_{2n}H_{4n}+2O_{n+1}$ (Sigma-Aldrich) (Figure 2.2) was used because it is a hydrophilic polymer forming crosslinks with hydrogels via different chemistries [155].

The other porogen chosen for this study was Pluronic F127 (Sigma-Aldrich) (Figure 2.3). It is widely used in the synthesis of mesoporous oxides because of its low toxicity.

2.1.3.2 Experimental set-up: Sol-gel

TiO_2 sols were prepared by the hydrolysis of a titanium alkoxide in a large excess of acidified water (H_2O/Ti $\sim$ 90). In a standard procedure titanium (IV) isopropoxide (TTIP),
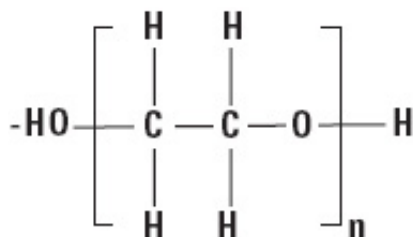
Figure 2.2: Structure of polyethylene glycol [156]
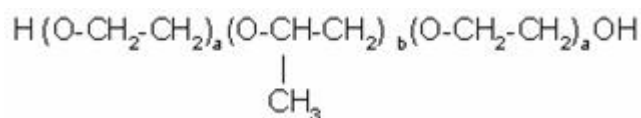
Figure 2.3: Structure of Pluronic F127 [157]

previously dissolved in anhydrous isopropyl alcohol ($C_3H_8O/Ti = 3.5$) was added quickly, under vigorous stirring to hot water (70 °C) acidified with nitric acid ($H^+/Ti= 0.2$). A white precipitate was obtained and the mixture was stirred for 16 hours at 80 °C. The white suspension changed, gradually, to a translucent sol by peptization. During the first 6 hours, the reaction flask was kept uncovered in order to allow the isopropyl alcohol to evaporate (the boiling point of the azeotrope isopropanol-water [87.4% – 12.6%] is 80.3 °C).

At the end of peptization, the pH of the sol was approximately 1.4 and the molar concentration of Ti was in the range of 0.6–0.65 M. This is close to the expected concentration if the isopropyl alcohol had totally evaporated (0.62 M). Henceforth, this procedure will be referred to as "standard".

In certain syntheses, TTIP was used pure without prior dilution in isopropyl alcohol, while in the others TTIP was partially complexed by acetylacetone (acac H/Ti= 0.5) before hydrolysis. Sols containing porogen (PEG 2000 or Pluronic F-127) were prepared by direct addition of the porogen into the sol followed by gentle stirring overnight at room temperature.

Coatings by sol-gel: Tape-casting

The coatings were produced on the polished and cleaned SS-304L substrates by a simple tape casting technique. The thickness of the coating was defined by the use of an ordinary adhesive tape as shown in Figure 2.4.

Porogens (PEG 2000 and Pluronic F-127) were added, separately, to the mother sol (MS) in the following ratio ([EO]/[Ti] = 0.5).

To test the effect of ultrasonication on the final photocatalytic activity of the coating,
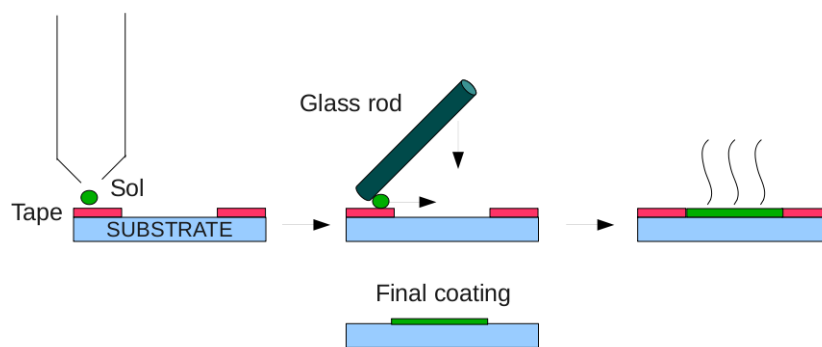
Figure 2.4: Coating by tape-casting

the sols were placed in an ultrasonic bath for 15 minutes and then used to coat the SS-304L substrates immediately.

A drop of the sol was deposited with a pipette at one masked end of the substrate and then spread over the entire unmasked area of the substrate with the aid of a glass rod. The sample was then allowed to dry at room temperature, before being heat treated. The dry samples were transferred to a furnace and heat treated at the required temperature (350 °C or 600 °C) for 3 hours at a ramp rate of 1 °C/min.

The samples obtained by this method were eventually rejected since they exhibited poor adhesion (Appendix I).

Coatings by sol-gel: Dip coating

The coatings obtained from the tape-casting process had problems with adhesion, possibly due to the very large thickness of the film, and hence, to overcome this, a dip-coating technique was used. The following parameters were used to produce thin films TiO_2 coatings; a withdrawal rate of 10 mm/min, followed by air drying and then heat treatment in an air furnace at specific temperatures (350 °C, 550 °C, 750 °C) for 3 hours at a ramp rate of 1 °C/min.

2.1.4 CVD: Set-up of MOCVD reactor

A cold-wall vertical reactor with an outer-diameter of 50 mm, an inner-diameter of 46 mm and a length of 240 mm was used (Figure 2.5). The mass flow of the nitrogen carrier gas was regulated by mass flow meters (MKS and Brooks).

The temperature of the coating was regulated with the aid of a K-type thermocouple, attached to a HF induction regulator, inserted into the core of stainless steel substrate holder, 2 mm under the substrate. The precursor (TTIP, Aldrich, 97%) was filled into a bubbler apparatus, in a glove box, before being placed under nitrogen in the MOCVD
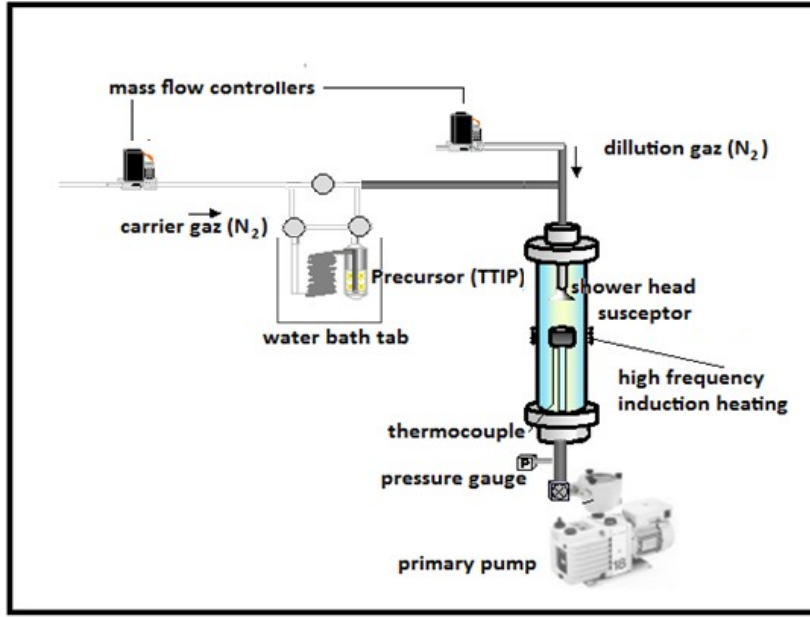
Figure 2.5: Schematic of cold-wall MOCVD reactor

set-up. The bubbler containing the precursor was placed in a temperature-regulated water bath, to obtain the required vapour pressures. Nitrogen was used as both the carrier gas, as well as the dilution gas. The gas lines carrying the reactant species were heated at 70 °C by heating cords to prevent re-condensation of the precursor.

The pressure was regulated with the help of the pressure valve (MKS) attached to the primary pump. Before and after each experiment the primary pump was switched on to evacuate the reactor. This was done to maintain the same atmosphere before each experimental trial.

The coefficients in the Clausius-Clapeyron equation which take into account the change in the saturation vapour pressure of TTIP as a function of temperature were established using equation 2.1, determined during the PhD thesis study by F. Duminica [124].

$$logP_{prec}(torr) = 9.465 - \frac{3222}{T(K)} \tag{2.1}$$

Once the saturation vapour pressure was calculated at a particular temperature (temperature of water bath in set-up) (Figure 2.6), the molar fraction was calculated by equation 2.2.

$$\chi_{prec} = \frac{P_{prec} \cdot Q_{prec}}{P_{reactor} \cdot Q_{N_2}} \tag{2.2}$$

where, χ_{prec}: mole fraction of precursor, P_{prec}: precursor pressure Q_{prec}: precursor gas
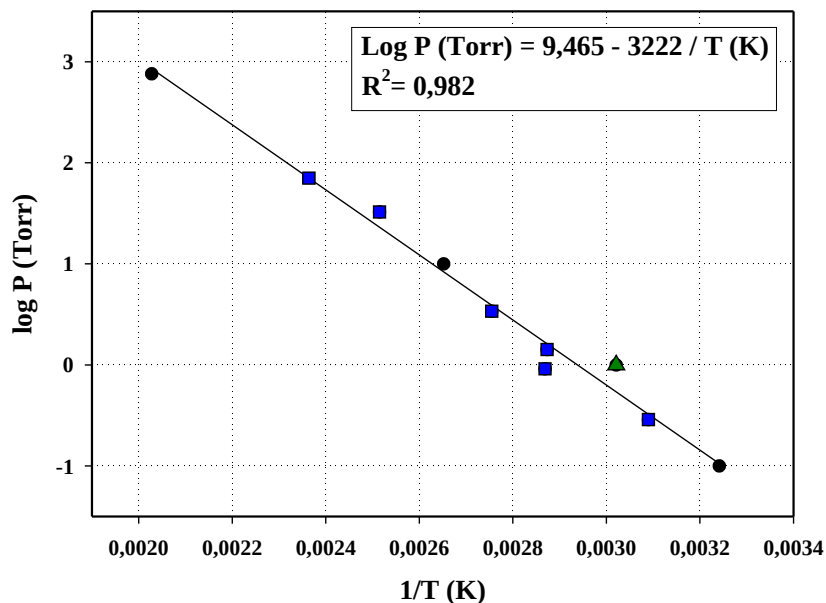
Figure 2.6: Vapour tension of TTIP as a function of temperature. ● = The MERK Index, Eleventh edition, 1989,1492; ▲ = INORGTECH, Oxide and nitride precursors, 2001; ■ = data from [124]

(carrier gas) flow rate $P_{reactor}$: reactor pressure Q_{N_2}: total gas (carrier and dilution) flow rate

2.1.5 Photocatalysis measurement set-up

The coatings produced by both sol-gel and CVD processes were tested for their photocatalytic activity. The indicator used to test the photocatalytic activity was an aqueous solution of methylene blue. This indicator was chosen because it is a commonly used dye in the dyeing and printing industry, which produces toxic effluents that cause potential harm to the natural environment. It is also a common indicator to test photocatalytic activity by other research groups [158]. The coatings were first immersed in 10 ml (in a quartz tube) of the methylene blue (MB) solution (10^{-5}M) and placed in the dark for 60 minutes. This was carried out by a simple process of covering the quartz tube with a beaker wrapped in aluminium foil paper. This was done to allow for the adsorption-desorption of the MB solution. The solution was stirred with the help of a magnetic stirrer. After the 60 minutes, the absorbance of the MB solution was measured with the help of a UV-Vis spectrometer (Perkin-Elmer Lambda 19). Then the quartz tube was placed in an oven fitted with a UV lamp ($\lambda = 360$ nm). This lamp was placed over the mouth of the tube at a distance of 12 cm from the coating with a power density of 1 mW/cm². The coating was irradiated for 60 minutes by the UV-lamp, under constant stirring. The temperature of the

oven was maintained at 25 °C (±5°), by a circulating current of air. After the 60 minutes of UV-radiation, the methylene blue absorbance was measured again. When introduced into the Beer-Lambert law (equation 2.3) the difference in the absorbance measurements at ∼664 nm (Figure 2.7) gives the reduction in the concentration of the MB solution due to the UV-radiation. Finally, the photocatalytic (PC) activity was calculated by equation 2.4.

$$A = \varepsilon l C \tag{2.3}$$

where,

A: absorbance; ε: molar absorptivity; l: path length; C: concentration of solution.

$$PC\ activity = \Delta C / C_{after\ dark} \tag{2.4}$$

where,

Δ C: $C_{after\ dark}$ - $C_{after\ UV}$
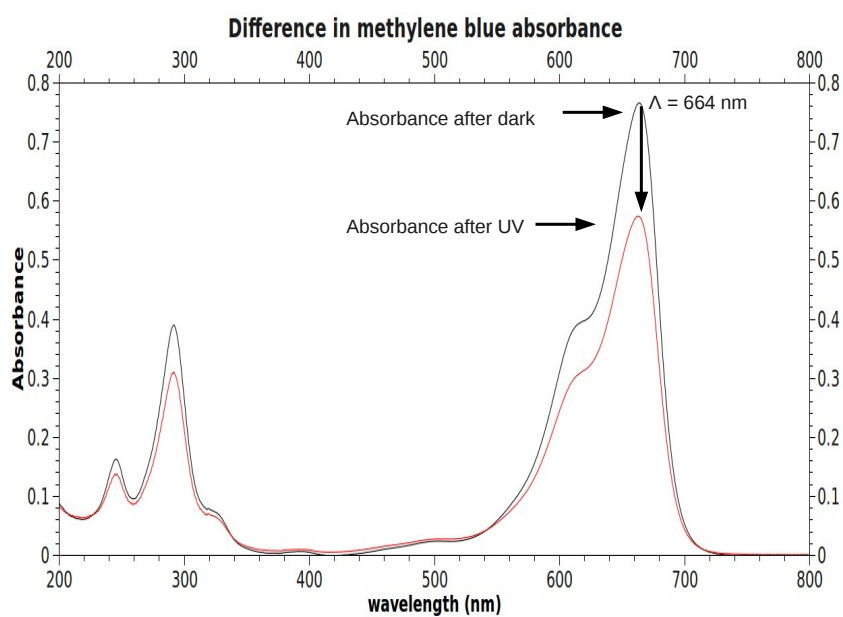
Figure 2.7: Difference in absorbance due to UV light used to calculate difference in concentration

2.2 Characterization techniques

2.2.1 Rheology

In order to measure the viscosity of the sols rheology measurements on the sols were conducted with a rheometer (Anton Paar Physica MCR) fitted with a cone and plate device. The dimensions corresponding to the geometry were 50 mm for the diameter and 1° for the angle. The minimum distance between the plate and truncated cone was 0.05 mm.

Rheograms were recorded at 20 °C, over a range of 1–1000s-1, with a total time period of 300 seconds, for both the increasing and decreasing shear-rate sweeps. For each sample, a minimum of three measurements was performed. Frequently, at lower shear rates (<10s^{-1}), some fluctuations in viscosity were observed, especially in the case of the less viscous sols.

2.2.2 Zeta potential and particle hydrodynamic diameter

Electrophoretic mobility and particle hydrodynamic diameters were determined on a Malvern Zetasizer 3000 using a He–Ne laser as the light source (k= 633 nm). The zeta potential of the sol was calculated from the electrophoretic mobility using the Henry equation and the Smoluchowski approximation. Samples were prepared by diluting the sols with acidified water (HNO_3). The initial pH was close to 2.0. It was then increased to the required value by addition of NaOH. No electrolyte was added and as a result the ionic strength varied with pH. Particle sizes were measured by photon correlation spectroscopy (PCS). All size measurements were conducted at 25 °C, with a scattering angle of 90°. To control the effect of multiple scattering and particle interaction, analyses were performed at several dilutions in order to verify that the measured size was independent of the dilution.

2.2.3 X-ray diffraction (XRD)

2.2.3.1 Powder X-ray diffraction (PXRD): TiO$_2$ powders by sol-gel synthesis

The crystal structure of the powders prepared by the sol-gel synthesis was investigated by powder X-ray diffraction. Data was collected, at room temperature,with a Bruker AXS D4 (θ–2θ) diffractometer, in the Bragg–Brentano geometry, using filtered Cu Kα radiation and a graphite secondary-beam monochromator. Diffraction intensities were measured by scanning from 20 to 80° (2θ) with a step size of 0.02°(2θ).

Crystalline structures were refined by the Rietveld method [159] with the FullProf software [160]. The peak profiles were modelled by pseudo-Voigt functions. The parameters refined were zero shift (2θ), background, scale factor, unit cell parameters, peak shapes,

overall isotropic thermal factors and U, V, W profile parameters (for brookite, only W was used). The quality of the fit was determined visually by inspection of the difference plot and statistically by the goodness of fit (χ^2) defined by :

$$\chi^2 = \Sigma\omega_i \frac{(\psi_{i0} - \psi_{ic})^2}{(N - P)} \tag{2.5}$$

where, ω_i is the weight assigned to each observation,

$\psi_{i0} - \psi_{ic}$ are the observed and calculated intensities at the ith step respectively,

N - number of points used in the refinement,

P - number of least-squares parameters refined.

The refined FWHM (full-width at half-maximum) of the lines was used to compute, by the Scherrer's equation, the average crystallite size [161]. The instrumental broadening contribution was evaluated by using a highly crystalline rutile sample as the standard.

2.2.3.2   XRD: Coatings by sol-gel and CVD processes

XRD analyses of the coatings were performed on a Seifert XRD 3000TT, fitted with a graphite monochromator. The analyses were performed using the grazing incident XRD configuration. The incident beam was set at an angle of 3° with a step of 0.4° and a dwell time of 1 second. For thin films (sub-micron thickness) this configuration is commonly used in order to reduce the contribution of the substrate.

The crystallite size of the coatings for both CVD and sol-gel coatings were determined using the Williamson-Hall plot. The Williamson-Hall plot is a method used to determine the crystallize size and strain by considering the integral breadth of a reflection (β) as a function of 2θ. The curves are constructed by plotting (β_{obs}-β_{inst}) cosθ in radians versus 4 sinθ. In this study, the Williamson-Hall plot was obtained for the Lorentzian peak shape. Once a linear fit to the data was obtained the crystallize size was determined from the y-intercept of the fit, equation 5.7, while the strain was determined from the slope of the fit, equation 2.7

$$Intercept = \frac{\lambda}{D} \tag{2.6}$$

$$slope = strain \tag{2.7}$$

2.2.4 Specific surface area, pore size distribution, density

The specific surface areas were computed from adsorption isotherms, using the Brunauer-Emmett-Teller (BET) method [162]. The adsorbate used was nitrogen and the isotherms were recorded at 77 K, with a Micromeritics ASAP 2010 M and a Tristar II 3020. The pore size distributions (PSD) were computed from the nitrogen desorption isotherms by the NLDFT method [163] (with Quantachrome Autosorb-1 software using silica equilibrium transition kernel at 77 K, based on a cylindrical pore model).

Skeletal densities of TiO_2 powders were determined using a gas pycnometer (Micromeritics AccuPyc 1330) working with helium. Each experimental value was the average of 10 successive measurements on the same sample.

Analyses were performed on coatings using Krypton at 77.4 K, as the saturation pressure of Kr, at this temperature, is 1/300 times that of nitrogen, it gives a higher accuracy, but the lack of sufficient mass of coating made it difficult to obtain reliable values, hence, further analyses using this technique were abandoned.

2.2.5 Electron microscopy

TiO₂ powders: Conventional Transmission electron microscopy (TEM) observations were performed on a JEOL 1400 operating at 120 kV. Samples of the sol were prepared by dipping a carbon-coated grid in a sol diluted 50 times by water. Then the grid was allowed to dry for 48 hours at room temperature.

Scanning electron microscopy (FEG-SEM) analyses were performed, with a JEOL JSM-6700F, on small glass pieces cut from coated substrates.

Coating: The morphology of the coatings were examined under a scanning electron microscope (LEO-435). The accelerating voltage was, typically, fixed at 15 kV and the working distance at 10 mm. In addition, the thickness of the coatings were also determined using cross-sections of the samples. This was used instead of reflectometry analyses since the coatings were, under certain coating conditions, too thick ($>10\mu$m) to be analysed.

The JEOL JSM-6700F was also used to examine the coatings by the sol-gel and CVD processes, at high resolution.

2.2.6 Atomic force microscopy

The AFM technique is a high resolution (few microns to sub-nanometre scale) imaging technique that is frequently utilized these days, as it can image, both, conducting, as well as, non-conducting surfaces. The added advantage to this technique is it does not require vacuum conditions to work. Two modes of imaging are commonly used; contact mode and

tapping mode. The contact mode is, typically, used for imaging hard and flat surfaces. The disadvantage with this mode is the tip of the AFM probe may cause deformations on the surface of the sample, this could potentially reduce the resolution of the image, as the tip comes into further contact with the sample surface. The tapping mode was developed to reduce the problems faced while using the contact mode. In this mode, the tip of the AFM probe oscillates at a frequency close to it's resonant frequency, this brings the tip into contact with the sample surface, intermittently, thereby reducing the lateral forces that arise during the contact mode [164].

In this study, all AFM measurements were performed on a multi-mode AFM (Agilent 5500) in tapping mode with a n-doped Si tip, at ambient conditions. In the case of coatings by CVD, the coatings on Si susbtrates were imaged (SS substrates, polished with 600 grit sandpaper, was too rough for AFM analysis), while in the case of sol-gel samples, the SS samples (polished with 4000 grit sandpaper) were imaged. Topography scan areas of 1 μm$\times$1 μm and and 10 μm$\times$10 μm, were imaged for each sample. The 10 micron topography scan (more representative) of each sample was then analysed using Gwyddion software [165, 164], to determine the roughness parameters as well as the surface area of the sample. Of all the roughness parameters obtained, the root mean square roughness (S_q) was considered in this study. This value represents the standard deviation of the pixel height data (equation 2.8).

$$S_q = \sqrt{\frac{\Sigma(Z_i - Z_{ave})^2}{N}} \tag{2.8}$$

2.3 Statistical methods

2.3.1 CVD experimental set-up using DoE

The control of various structural properties of CVD coatings requires a good understanding of the impact of individual process parameters. As mentioned in Chapter 1, this is typically performed, empirically, from results obtained from numerous experimental trials or from computational models that have, either, a limited range of applicability, or are limited by their approach, for example, changing one parameter at a time. All these methods are inevitably costly, time-consuming, or both [133]. Therefore, in an attempt to overcome the above mentioned obstacles, a statistical tool called Design of Experiment (DoE) was utilized here, for the first time, to our knowledge, in the MOCVD synthesis of TiO_2.

Table 2.3: Comparison of experimental conditions utilized in previous studies with current study*

Reactor/geometry	χ (10^{-6})	T_c $(^\circ C)$	P (Torr)	Flow rate (sccm)
Hot-wall/horizontal	76-1035	300-600	1,20	600
Cold-wall/vertical	10-10000	400-700	10,760	30-5000
Hot-wall/horizontal	76-9000	300-600	1-20	595-650
*Cold-wall/vertical	232-2710	350-600	2.5,20.	600

Table 2.3 reports the MOCVD experimental conditions exploited by previous studies in CIRIMAT, Toulouse [124, 166, 167]. The present study encompasses the synthesis conditions of the previous three studies, except for pressure, since at lower pressures (lower than atmospheric pressure) there is better control of coverage of complex geometries. The difference between the previous studies and this study is in its experimental approach. The trends that were empirically obtained over 20 experiments is being quantitatively determined in $\leqq 15$, therefore this approach is expected to be more efficient, as well as, quantitative.

The terms that are important in a DoE are,

1. Factors - refers to the process parameters that are under investigation

2. Response - refers to a particular property (example: thickness of coating) that is of interest.

3. Effect - quantitative representation of the significance of the factor on the response, i.e. if the effect of a particular factor has a relatively high value, then it is more significant on the response than the other factors under investigation.

4. Experimental domain - the range (of the factors) under investigation

The objective of a DoE is to,

1. Screen the factors that are the most important and rank them in a hierarchical order.

2. Optimize the coating properties mathematically - it allows to predict the system response, regardless, of the values of the operational parameters, within the range the model was established. Therefore, it might be used to specify the right operational parameters values to obtain the desired response.

3. Determine the interaction between the operational parameters.

There are different types of DoE and the choice of a DoE depends on the objectives of the experiment and the number of factors to be investigated (Table 2.4) [168].

1. A *Comparative design* is chosen if there is one or several factors under investigation, but the primary goal of the experiment is to make a conclusion about one important factor, and the question is whether or not that factor is "significant".

2. The primary objective of a *Screening design* or main effects design is to select the few important main effects from the many less important ones.

3. The *Response Surface (method) design* is used to estimate interaction, as well as, quadratic effects. This gives an idea of the (local) shape of the response surface and hence is termed as response surface method (RSM) designs.

4. A *mixture design* is implemented when the factors chosen are proportions of a mixture and the objective is to determine the "best" proportions of the factors in order to maximize (or minimize) a response.

5. A *regression design* is used when unbiased and minimum variance model parameter estimates are required to model a response as a mathematical function of a few continuous factors.

For this study, the Screening design was chosen. The first step in a DoE is to determine the objectives of the experiment. This is followed by identifying the process parameters (X) and their operating range within which the parameters should be varied and then choosing an appropriate process response model (Y_{model}). A model establishes the connection between the response and the factors, taking into account the interactions amongst these factors. Generally, in all the models, the interactions between more than two factors are considered insignificant [169, 170].

Table 2.4: DoE design selection guide

Number of factors	Comparative objective	Screening objective	Response surface objective
1	1-factor completely randomized design	-	-
2 - 4	Randomized block design design	**Full or fractional**	Central composite or factorial Box-Behnken
>5	Randomized block design design	Fractional factorial or Plackett-Burman	Screen first to reduce number of factors

The determination of the model is based on the resolution of a matrix equation of the form :

$$Y = X.a \tag{2.9}$$

There are two types of models : first-order models (equation 2.10) and second-order models (equation 2.11).

$$Y = a_0 + a_1 X_1 + a_2 X_2 + a_3 X_3 + a_{12} X_1 X_2 + a_{13} X_1 X_3 + a_{23} X_2 X_3 \tag{2.10}$$

$$Y = a_0 + a_1 X_1 + a_2 X_2 + a_3 X_3 + a_{12} X_1 X_2 + a_{13} X_1 X_3 + a_{23} X_2 X_3 + a_{11} X_1{}^2 + a_{22} X_2{}^2 + a_{33} X_3{}^2 \tag{2.11}$$

The higher the model order, the higher the number of coefficients 'a' to establish, and therefore, the higher the number of runs to perform. In our design, we start from a first-order model so as to prioritize the factors. If the model is not validated after statistical tests, it is either completed with additional experiments, in order to improve the coefficients 'a', or the model order has to be increased. The effects are estimated by equation 2.12.

$$\hat{a} = (\bar{X} \cdot X)^{-1} X \cdot Y \tag{2.12}$$

where, $\bar{X}$ is the transpose of matrix X.

2.3.1.1   Fractional factorial design

When faced with a large number of experimental trial runs, one of the solutions is to use a fraction of the full factorial design. For the purpose of completing the study in a timely manner, a fractional factorial DOE was chosen.

When a fractional factorial design is used, the effects of the individual process parameters and their interactions are aliased with each other . This means that the value of the effect (a_i) is a result of not only the main effect (a_i) itself, but also biased by other interactions.

2.3.1.2   Set-up of DoE

The setting up of a DOE is based on the following steps,

1. choice of the parameters and responses and the corresponding range in which they should be varied,

2. choice of plan type, required by the goal (screening or optimization),

3. experimental matrix : list of experiments to perform,

4. resolution of the plan to prioritize the factors and establish the model,

5. validation of the plan with statistical tests.

After careful review of experimental results from previous studies ([124, 166], the following four parameters were chosen, to be varied: distance between the substrate and the precursor entry-port in the reaction chamber (d), coating/deposition temperature (T_c), reactor pressure (P), precursor temperature (T_p) (Table 2.5). The distance parameter values were fixed at the upper and lower limits of the induction ring that heated the substrate. The coating temperature values were fixed based on the phase of TiO_2 required (350 °C: anatase; 600 °C: mixture of anatase and rutile). The pressure of the reactor chamber was fixed at the values similar to those used in previous studies at CIRIMAT (refer Table 2.3). The precursor temperature range was fixed at values corresponding to molar fractions that resulted in different morphologies. The duration for the coating for all the experiments, in the CVD section, was fixed at three hours; this value was determined to be ideal, by trial and error, as it yielded sufficient coating for analysis. The mass and the thickness were not kept constant because the kinetics of the growth rate were unknown. The constant operational values used in this study for synthesizing TiO_2 coatings by MOCVD are reported in Table 2.6.

Table 2.5: Operational parameters varied in DoE

Parameters	Designation	Lowest value	Highest value
Distance (mm)	d	50	70
Coating temperature (°C)	T_c	350	600
Reactor pressure (torr)	P	2.5	20
Precursor temperature (°C)	T_p	37	42

Table 2.6: Constant operational parameters in MOCVD

Duration of coating	180 min
Molar fraction	0.00034 -0.0027
Carrier gas (N_2) flow	20-25 sccm
Dilution gas (N_2) flow	570-580 sccm
Temperature of carrier pipes	70 °C

For a two-level, full factorial DoE with four factors, i.e. 2^4 design, there would be a total of 16 experimental runs. In the interest of time, this was reduced to a 2^{4-1} design, leading to a total of 8 experimental runs, Table 2.7. The assumption, here, is that some of the information obtained from a full plan is not useful since interactions between more than 2 factors are taken into account, whereas, these interactions are assumed to be insignificant.

The fractional factorial model for this design is as follows:

$$Y = a_0 + a_d d + a_{T_c} T_c + a_P P + a_{dT_c} dT_c + a_{T_c P} T_c P + a_{dP} dP + a_{dT_c P} T_p \qquad (2.13)$$

where, Y- response; d, T_c, P, T_p - factors ; a' - alias (since a fractional plan is used, the effect of the factor interactions are biased by other effects)

Table 2.7: The 2^{4-1} design table with reduced values

Trial run no.	d	T_c	P	T_p=dT_cP
1	-1	-1	-1	-1
2	1	-1	-1	1
3	-1	1	-1	1
4	1	1	-1	-1
5	-1	-1	1	1
6	1	-1	1	-1
7	-1	1	1	-1
8	1	1	1	1

In Table 2.7, the reduced values -1 and 1 represent the lowest and highest values of the operational parameters. The value for the 4th factor (T_p) is generated by the Box-Hunter generator (equation 2.14), where, the product of all the factors in each run (reduced value) should equal 1. When we multiply T_p (column multiplication) on both sides of equation 2.14, we get the defining relation of this design (equation 2.15).

$$T_p = d.T_c.P \tag{2.14}$$

$$T_p.T_p = I = d.T_c.P.T_p \tag{2.15}$$

With this relation we can determine the complete confounding pattern for the design, (i.e. $I = d.T_c.P.T_p$; $d.T_c = P.T_p$; $d.T_p = P.T_c$, and so forth), keeping in mind that interactions between more than 2 factors are discarded. The alias for each factor is broken down into its constituent effects and interactions are negligible when compared to effects below (equation 2.16 - 2.23).

$$a_d = a_d + a_{T_cPT_p} = a_d \tag{2.16}$$

$$a_{T_c} = a_{T_c} + a_{dPT_p} = a_{T_c} \tag{2.17}$$

$$a_P = a_P + a_{dT_cT_p} = a_P \tag{2.18}$$

$$a_{dT_c} = a_{dT_c} + a_{PT_p} \tag{2.19}$$

$$a_{dP} = a_{dP} + a_{T_cT_p} \tag{2.20}$$

$$a_{T_cP} = a_{dT_p} + a_{T_cP} \tag{2.21}$$

$$a_{dT_cP} = a_{T_p} + a_{dT_cP} = a_{T_p} \tag{2.22}$$

$$a_0 = a_0 + a_{dT_cPT_p} = a_0 \tag{2.23}$$

This model is a plan of resolution III [1], therefore, aliasing is not a hindrance in the determination of the pure effects of the factors. On the other hand, the calculation of the interactions of the 1st order is difficult. To aid in the determination of the effects of these interactions, an assumptions is made, wherein, the effect of one of the 4 factors is negligible and, therefore, for the first approximation, the interactions with this factor is neglected. i.e., if 'd' is neglected in equation 2.19, the final equation becomes,

$$a_{dT_c} = a_{PT_p} \tag{2.24}$$

Once the design table (Table 2.7) was set up, the -1 and 1 were replaced with the real values for the operational parameters, $d.T_c.P.T_p$, as shown in Table 2.8. The responses that were studied were the properties of the coating;

1. mass

2. roughness

3. thickness

4. polymorphic composition

5. crystallite size

Table 2.8: The 2^{4-1} design table with real values

Trial run no.	d	T_c	P	$T_p=dT_cP$
1	50	350	2.5	37
2	70	350	2.5	42
3	50	600	2.5	42
4	70	600	2.5	37
5	50	350	20	42
6	70	350	20	37
7	50	600	20	37
8	70	600	20	42

2.3.1.3 Validation of model

This step is crucial to evaluate the deviation of the model from experimental data, the error (quantitative) that the model commits in predicting the system's comportment. This is important because of the various assumptions made in this study, such as,

---

[1]Resolution is a term that is used to describe the degree to which the main effects have been aliased, typically, resolution V is excellent, resolution IV is adequate and resolution III is economical

1. first order model

2. neglecting the least significant factor to aid in the calculation of the interactions

To validate the degree of the model (first-order), we proceed on the principle that for a finite number of experiments, the system response follows the Student's t-distribution. Using this law, the first step is to evaluate the following deviations,

1. error in measurement - standard deviation of 'n' measures conducted on a single sample, σ_m

2. experimental error - standard deviation of the measures of 'n' experiments performed under similar conditions, σ_e

To validate this model and estimate the experimental error, at least 3 experimental runs have to be performed in the centre of the experimental domain, this is to avoid favouring one parameter over another, and the average response of these 3 runs ($Y_{experimental}$) is compared to the value predicted by the model (Y_{model}). The model is validated if Y_{model} lies in the range of $Y_{experimental} \pm 3\sigma$, where, $\sigma = \sigma_e + \sigma_m$. This criteria is based on the fact that the measures conducted on 'n' samples synthesized under similar conditions are a part of a Gaussian curve and centred around an average 'A' of these measures. It is estimated that there is a probability $\geq 99\%$ that an additional measure will fall within the interval of $A \pm 3\sigma$.

Due to problems caused by the change in the precursor batch (detailed in Appendix II), the experiments at the centre could not be repeated 3 times. Thus, the estimation of the error associated with the experiment and model (degree) validation could not be performed at the same time. Therefore, in lieu of the normal validation procedure, two experiments, with almost similar experimental conditions, were used to validate the model. The evaluation of the error associated with the experiment was in turn carried out using other experiments (not at the centre). From a statistical point of view this approach is questionable, due to the low number of repetitions, but, it nevertheless gives an approximation of the experimental error.

Also, due to the low number of experimental runs performed to estimate the experimental error in the test domain the criterion $A \pm 3\sigma$ may not be applied. This reasoning is based on the Student's t-distribution which evaluates the tolerance interval associated with the probability of finding the additional measure in this interval taking into account numerous measurements. In this study, 3 similar experimental runs were rarely performed, often times, 2 different experimental runs were repeated twice, hence, an analysis of the Student's t-distribution may not be relevant.

We will, therefore, simply calculate the relative difference between the model and experimental values and compare it to the total standard deviation ($\sigma = \sigma_m + \sigma_e$). This is certainly not statistically conclusive, but, it gives an approximation of the error made by the model. This is sufficient to achieve our goals:

1. screening factors

2. correlations between process parameters and coating characteristics

In the future work of this thesis, a rigorous statistical study into the variance in the process, to stringently evaluate the experimental error, will be considered. If the degree of the model is not validated, then further experiments must be conducted at different reduced values (to increase the experimental domain), which would be considered a model of second order.

2.3.2 Principal component analysis (PCA)

Principal component analysis (PCA) is a tool from the field of applied algebra and is frequently used as an analytical tool to 'demystify' complicated data. Large data, as well as, clouded data pose a fundamental problem to the advancement in many fields of research. The goal of PCA is to filter the unclear data from the data set, and in doing so, reveal the various, sometimes hidden, interactions between the data points [171].

PCA transforms complicated or large data sets into a new coordinate system consisting of 'principal components'(PC). These new set of coordinates are obtained from the raw data, in this case the coating properties under investigation. The raw data is converted to a standardised set of data for easier comparison, by the following mathematical transformation.

$$X_i = \frac{(V_i - m)}{\sigma} \tag{2.25}$$

where,

X_i: raw data, m: mean, σ: standard deviation

Once the raw data has been standardized, this new standardized data is then compared with each other (for example: mass versus thickness, thickness versus roughness, etc.). A correlation matrix is set up with the regression coefficients of the above-mentioned comparison process (an example is showed in Table 2.9).

From this matrix diagonalisation, a new set of coordinates are obtained called the 'principal components'. These principal components are then used to obtain different types of information.

Table 2.9: An example of a correlation matrix obtained during the PCA analysis. X_1, X_2, X_3: coating properties (standardized), r_{ij}: regression coefficient

	$\mathbf{X}_1$	$\mathbf{X}_2$	$\mathbf{X}_3$
$\mathbf{X}_1$	1		
$\mathbf{X}_2$	r_{12}	1	
$\mathbf{X}_3$	r_{13}	r_{23}	1
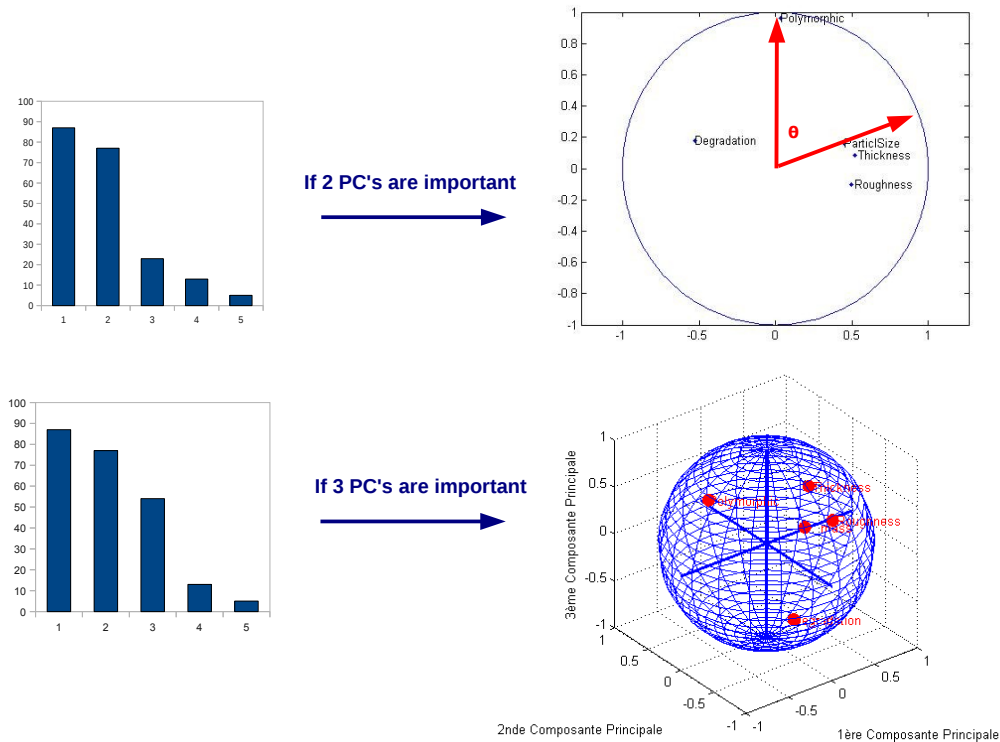
Figure 2.8: Interpretation of PCA plot

1. Score plot: Here the samples are plotted as a function of the new coordinate system and in this study it helped to group samples with similar characteristics.

2. Data plot: Here the raw data is plotted as a function of the principal coordinates. Depending on the number of important principal components, the plot is either a 2 dimensional plot or a 3-dimensional plot, Figure 2.8.

   If it is a 2-D plot, vectors should be drawn from the centre, and if there is, approximately, $\sim 90°$ difference between the vectors, then the two variables are not correlated, while a difference of $\sim 180°$ means that the two variables are anti-correlated and if the angle is small (approximately $0°$ - $30°$)between the two vectors then they are strongly related. In a 3-D plot, the 3^{rd}PC is included as well, since it is significant. Here if the variable points

are closer to the circumference of the sphere they are considered significant. To facilitate interpretation, the different views (2-D) of the 3-D plot are analyzed. These views are interpreted in the same manner as the 2-D plot.

Chapter 3

TiO$_2$ synthesis: sol-gel

Contents

In this chapter, we begin with a discussion on the parameters affecting the stability of the sol synthesized in this study. This is followed by the different characterizations performed on the sol to verify its stability as well as to determine the different properties of this sol.

Hydrolysis of titanium alkoxide in a large excess of water, followed by peptization, is a fast and easy method to prepare colloidal dispersions of titania nanocrystallites in water [152, 154, 172, 110, 173, 174, 175, 176]. The main parameters which have been recognized as effective to control the size and the stability of the colloids are the water/alkoxide and acid/alkoxide ratios, the temperature, and the alcohol concentration.

3.1   Parameters affecting sol stability

3.1.1   Effect of water/alkoxide ratio

Besides obtaining a stable sol, the goal was also to synthesize a sol that would produce powder (on drying the sol) with high specific surface area which would eventually be used for photocatalysis. This is done by maximizing the hydrolysis rate with respect to that of condensation. This is achieved by using a large excess of acidified water because titanium (IV) isopropoxide is monomeric and very reactive; it can be rapidly and completely hydrolyzed under acidic conditions, before condensation starts [177]. The optimum ratio of water to alkoxide appears to be in the range of 50–100 ; it was shown that above 200, the effect of dilution on particle size becomes negligible [176] and using a ratio larger than 100, leads to stable but highly diluted sols which will then require preliminary concentration before being used for coatings. On the other hand, for values lower than 30, some OR groups could persist due to incomplete hydrolysis [178]. The nanoparticles formed by this rapid hydrolysis have high surface energy and they agglomerate rapidly, producing large particles, leading to precipitation. These particles are amorphous due to fast nucleation rate, the particle growth is governed by kinetics leading to the formation of a less stable phase [179]. But this phase is also the most soluble and will be progressively replaced by crystalline phases, such as: brookite, anatase and rutile.

3.1.2   Effect of acid/alkoxide ratio and temperature

The rate of the crystallization process depends on the pH and temperature which govern the solubility. Peptization starts immediately if acidified water is used, or after the post addition of acid. As the PZC is close to neutrality, acid addition results in protonation of surface hydroxyls, increasing the electrostatic surface charge density of the particles, and

decreasing the interfacial tension [180, 181, 182]. This causes the fragmentation of primary particle agglomerates and also, as the colloidal particles bear the same electric charge, this prevents their re-aggregation because they mutually repel each other. In contrast to hydrolysis, peptization is a slow process that exhibits first-order kinetics with time constants of several days [153]. Kinetics studies have shown that the peptization is slow because it is the result of the simultaneous action of two competing mechanisms, the fragmentation of agglomerates, which is aided by the peptizing agent, and the reagglomeration of the fragments, which is driven by insufficient stabilization of the suspension [153, 110, 173].

Peptization time can be reduced by increasing either the temperature or the acid concentration [179]. However, this has negative side effects. Decreasing the pH and increasing temperature increases the TiO_2 solubility, leading to the growth of larger particles at the expense of smaller ones, by a classical dissolution-reprecipitation mechanism (Ostwald ripening). Moreover, secondary particles are formed by the epitaxial self-assembly of primary particles [152]. Another side effect of increasing the TiO_2 solubility is the progressive transformation of metastable crystalline phases, like brookite and anatase, into rutile which is the stable phase. Thus, to prepare highly stable sols it is mandatory to use an acid concentration close to the minimum amount required for peptization. If needed, the peptization time can be reduced by ultrasonication.

At this point a question arises, what is the best peptizing agent, HCl or HNO_3? Isley and Penn have shown that using HCl increases the amorphous content [154]. On aging, this amorphous phase will recrystallize into stable rutile. This was used as a method to prepare nanocrystallites of rutile [183]. On the other hand, HNO_3 is easily decomposed by heating above 300 °C, while it is far more difficult to remove chloride ions without extensive washing. Thus, except if the rutile phase is desired, HNO_3 is the better choice.

3.1.3 Effect of alcohol

Another important parameter, often neglected, is the presence of alcohol. Vorkapic and Matsoukas have shown that alcohols have a negative effect on the peptization [110]. They explain this effect by the decrease of the dielectric constant of the solvent leading to an enhanced rate of re-aggregation. It is also possible that alcohol stabilizes the amorphous phase formed just after the hydrolysis. Consequently, removal of the alcohol reduces the peptization time and stabilizes the sol. The presence of alcohol cannot be avoided since, even if no alcohol is added to dilute the alkoxide, four moles of isopropanol per mole of TIP are formed as a product of hydrolysis. Probably the easiest way of removing isopropanol is evaporation, by conducting the peptization in an open flask at a temperature close to the boiling point of the azeotrope isopropanol-water (80.3 °C). It is very common to dilute

the alkoxide in isopropanol prior to mixing with water in order to reduce the relatively high viscosity of the TTIP. This is expected to provide more homogeneous nucleation and reduce the growth process. However, we observed negligible differences in crystallite size when isopropanol was not added.

3.2 Optimized conditions for stable sol

Therefore, in order to produce highly stable hydrosols composed of ultra-fine crystallites, the optimized synthesis conditions are:

1. $H_2O/ Ti = 50 - 100$

2. HNO_3 as catalyst and peptizing agent with $H^+/Ti = 0.2$,

3. hydrolysis temperature in the range of $50 - 70$ °C,

4. peptization temperature close to 80 °C allowing isopropanol to evaporate.

These sols were made up of small aggregates (~ 100 nm) of anatase ($\sim 90\%$) and brookite crystallites ($5 - 6$ nm).

It is also possible to prepare stable sols, composed solely of anatase crystallites (4 nm), by partially complexing the TTIP with acetylacetone before hydrolysis. Acetylacetone (Acac) reacts with titanium alkoxides to form mixed complexes which are more difficult to hydrolyse than alkoxy group [177]. Upon hydrolysis, alkoxy groups quickly react, while all Acac ligands cannot be cleaved, even in presence of a large excess of water [184]. This inhibits condensation and either molecular clusters or colloidal particles can be synthesized depending on the relative importance of complexing (AcacH/Ti) versus hydrolysis (H_2O/Ti) [185]. Slowing down the condensation favours anatase formation (marginally more stable than brookite) and gives smaller crystallites.

3.3 Characterization of TiO_2 sol

3.3.1 Polymorphic composition and crystallite size by XRD

The effect of peptization time on the crystalline structure of the particles is revealed by the XRD patterns of several samples taken from the same sol at different time intervals (Figure 3.1). These patterns were recorded with powders obtained after drying the sol samples at 40 °C. The first one (labelled t = 0) was taken at the end of hydrolysis and it was almost completely amorphous. After 1hour, even if the main lines of anatase were identified,

the nanoparticles were still predominantly amorphous. After 4 hours the particles were nanocrystalline and there was very little difference with a sample taken 6 days after the synthesis. These patterns correspond to a mixture between two TiO_2 polymorphs, anatase (tetragonal, I41/amd, ICDD PDF ♯ 01-073-1764) and brookite (orthorhombic, Pbca, ICDD PDF# 00-029-1360). Comparison between the patterns of samples taken 6 days and 6 months after the synthesis (not shown in Figure 3.1) revealed negligible differences. Thus the size and the crystal structure of the nanoparticles are not modified by ageing which is proof of the high stability of these sols.
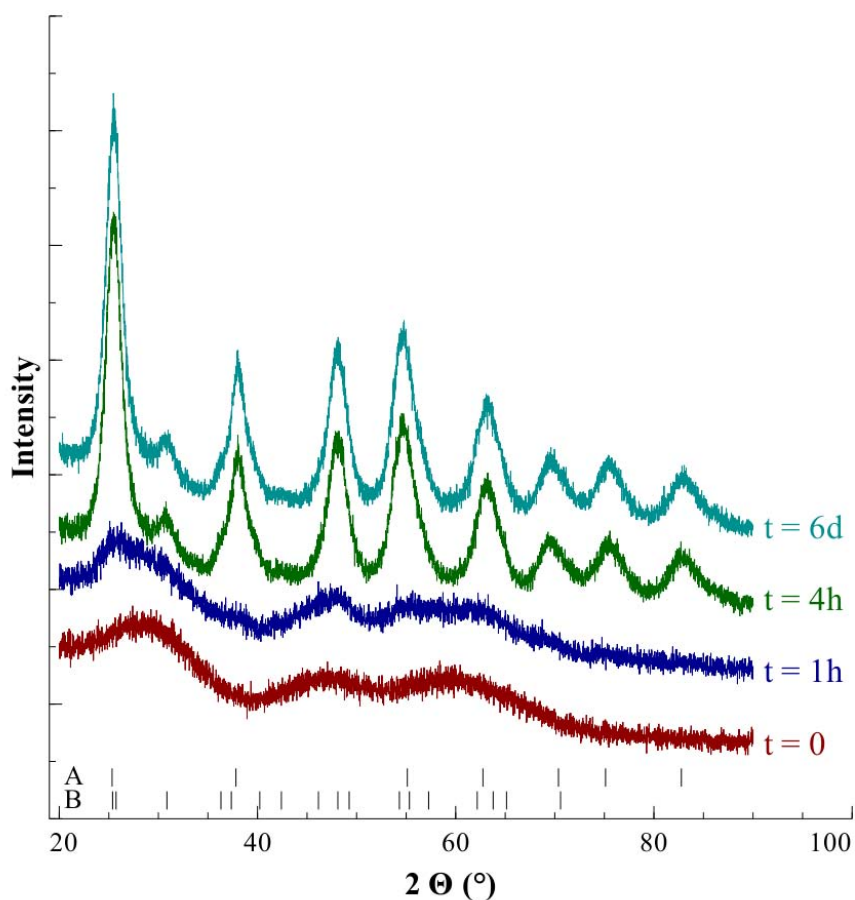
Figure 3.1: Effect of peptization time on the XRD patterns of sols dried at 40 °C. Patterns for t= 4 hours (4h) and t= 6 days (6d), correspond to a mixture between two titania polymorph, anatase, A (tetragonal, I41/amd, ICDDPDF# 01-073-1764) and brookite, B (orthorhombic, Pbca, ICDD PDF# 00-029-1360)

Rietveld refinements of the diffraction patterns give information on the phase composition, the cell parameters and, from the peak width, the crystallite size of each polymorph. For powders prepared in standard conditions and dried below 100 °C, the anatase fraction in the mixture was close to 90%. The anatase cell parameter 'a' was larger (3.80 Å)

than the value reported for bulk crystal (3.78$\mathring{A}$), but the parameter 'c' was lower (9.47 $\mathring{A}$ instead of 9.49 $\mathring{A}$). This has already been observed by Bokhimi et al. [186]. For brookite, 'a' and 'b' parameters were close to the values reported for bulk crystals, while 'c' was significantly larger (5.20 $\mathring{A}$ instead of 5.14 $\mathring{A}$). Anatase crystallites had a size close to 5 nm, while the size of brookite crystals appeared slightly larger (5.6 nm). Upon calcination up to 300 °C , the crystallite growth remained small (30%). Above this temperature, it increased faster; the size at 500 °C was twice that at 300 °C. Calcination increased the proportion of brookite (∼17%) as well, and then at 500 °C, 12% of rutile was formed. This data was in agreement with the study by Zhang and Banfield, who observed that anatase transforms to brookite and/or rutile, and then brookite further transforms to rutile [187].

When acetylacetone was added (acac H/Ti= 0.5) the peaks of brookite were no longer visible in the XRD pattern, the crystallite size decreased to 4 nm, and 'c' parameter became close to the value reported for bulk crystals. Conducting hydrolysis with pure water (no peptization) decreased, marginally, the brookite fraction (∼10%) and increased, imperceptibly, the crystallite size (∼20%). Using undiluted TTIP had no significant consequence on either the crystalline structure or the composition. The polymer (F127 and PEG2000) addition had a negligible effect on the cell parameters, though, there was a decrease in both the proportion of rutile, as well as, the crystallite size. Nevertheless, these stabilizing effects decreased when the EO/Ti ratio exceeded 1.5; both PEG2000 and F127 gave similar results.

It should be highlighted that long term ageing affects the particle organization, but does not change either the primary particle size or the polymorphic composition. This is confirmed by the perfect overlapping of the XRD pattern recorded on a fresh sol with the pattern recorded 6 months latter.

3.3.2 Peptization influence on particle size by TEM

The effect of peptization time on particle morphology was followed using the TEM. Similar to XRD analysis, the TEM was conducted on samples taken from the same sol at different time intervals. The sample taken, immediately, at the end of hydrolysis (t = 0) was composed of large particles (∼300 nm).

The top image of Figure 3.2 shows a part of these particles. They have a "cloudy" aspect which is in agreement with their quasi amorphous structure revealed by XRD. However, at some of their edges, facets are barely visible. After 4 hours (t = 4), the sol was still essentially composed of large particles (100 – 200 nm), but at this point, nanocrystalline structures are clearly visible with particle size of 4 – 5 nm. At the end of the peptization, after 16 hours, the sol contained small chain-like agglomerates having core size of 25 – 50
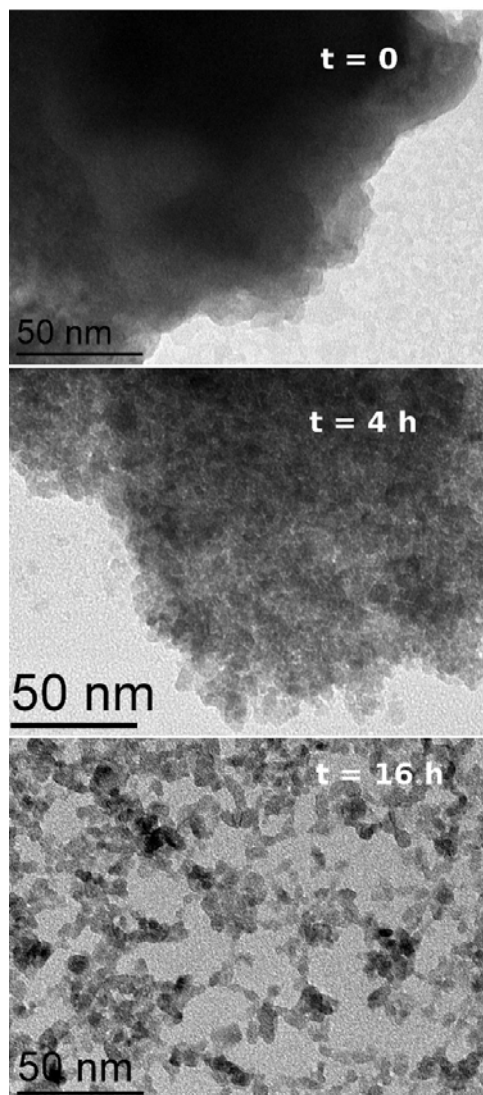
Figure 3.2: TEM images of TiO$_2$ sol at different intervals during the peptization process

nm. These agglomerates were composed of loosely packed crystallites of 5 – 6 nm. This size corroborated with the average size calculated by the Scherrer's equation from the peak width of the XRD patterns.

3.3.3   Relation between ζ-potential and pH by Zetametry

The dependence of the ζ-potential on the pH is shown in Figure 3.3. When the pH was increased the ζ-potential decreased quickly to the isoelectric point (IEP), which is approximately 5.4. This value corroborates with those values reported in literature [172, 188, 189, 190, 191, 192, 193]. When the pH was increased towards the IEP, two effects participated resulting in the decrease of the electrophoretic mobility. First, the particle surface charge

density decreased, second, as no electrolyte was added before the electrophoretic mobility titration, the ionic strength increased with pH and there was a compression of the double layer which also reduced the mobility of the particles. When the pH was increased to above the IEP, the effects opposed each other, as both the ionic strength and the particle surface charge density increased.
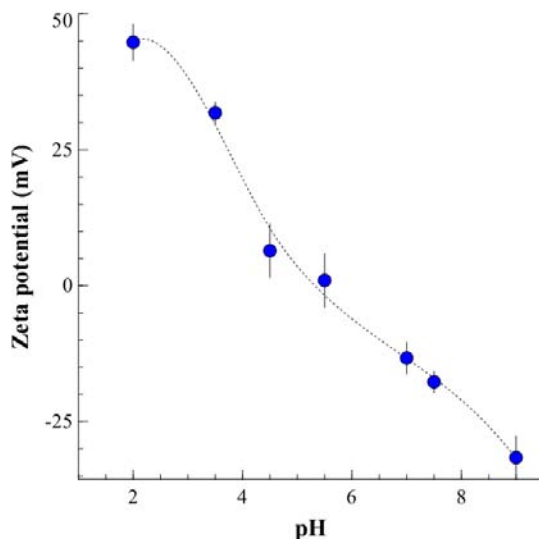
Figure 3.3: Dependence of the ζ-potential on the pH. The dotted lines are shown for visual aid

3.3.4 Particle size distribution by dynamic light scattering (DLS)

The mean hydrodynamic diameter of particles, measured on freshly prepared sols by dynamic light scattering, was found to be within the range of 300–500 nm. After a few days of ageing the particle diameter decreased to ∼100 nm. This change could be visually noticed; Freshly prepared sols were milky and on ageing became translucent. Our experimental data corroborated with electron microscopy images, as well as values reported in literature for sols prepared by hydrolysis of titanium alkoxide in large excess of acidified water [153, 172, 194, 110]. As reported in literature [172], when the sols were ultrasonicated a marked decrease in particle size (down to 20 nm) was observed.

3.3.5 Rheological behaviour inferences

The knowledge of the rheological behaviour of sols is important, in order to, control the thickness of the coatings. Moreover, it gives important information on, the interaction between the particles, as well as, aggregate morphology. Rheograms were measured by increasing and then decreasing the shear rate. For each rheogram, the curves obtained

during reversible shear rate-shear stress paths overlapped, i.e. no hysteresis was observed in any of the studied sols. Moreover, none of the sols exhibited Bingham plastic behaviour (yield stress can always be approximated to zero). The fitting of the experimental data was done by the power law rheological model [195],

$$\sigma = K\gamma^n \qquad\qquad (3.1)$$

where,

σ- shear stress (Pa),

γ - the shear rate (s^{-1}),

K - consistency coefficient, and

n - power law index.

When the sols exhibited Newtonian behaviour this model had an excellent agreement with the experimental data. Indeed, the least square fitting of experimental data with the model always gave correlation coefficients higher than 0.9999. The effect of ageing, PEG addition and ultrasonication, on K and n parameters, are highlighted in the graphs presented in Figure 3.4. Freshly prepared sols showed a shear thinning behaviour, with n close to 0.75. On ageing, this behaviour subsided as n tends toward 0.95. Ageing had a strong effect on K, which was reduced to a third of its original value six days after the synthesis.

Figure 3.4(a) reveals a linear relationship between K and the logarithm of time. Figures 3.4(c, d) show that the first addition of PEG induces significant decrease ($\sim$50%) of K and a smaller increase ($\sim$10%) of n on a fresh sol. This effect decreased and even vanished completely upon aging. Figure 3.4(e) shows that ultrasonicating the sol for 30 min strongly decreases K (about 40 times). Irrespective of the age of the sol, the value of K after ultrasonication remained the same. Figure 3.4(f) shows that, after ultrasonication, n becomes close to 1. The best-fit parameters obtained with a sol prepared without diluting the TTIP with isopropanol before hydrolysis were similar to those found for a sol prepared in standard conditions. Thus, although it accelerated the peptization, conducting the hydrolysis with undiluted TTIP did not seem to modify the aggregation of the particles in the sol. Finally, the best-fit parameters for a sol prepared with addition of acetylacetone to TTIP prior to hydrolysis showed that this sol exhibited Newtonian behaviour and low viscosity.

The shear thinning behaviour observed with freshly prepared sols, is because primary particles have a strong tendency to form aggregates with a chain-like structure. The packing density of these clusters decreases from the center to the edges and it seems probable that the outer edge particles could be disconnected from such aggregates at high shear rates.
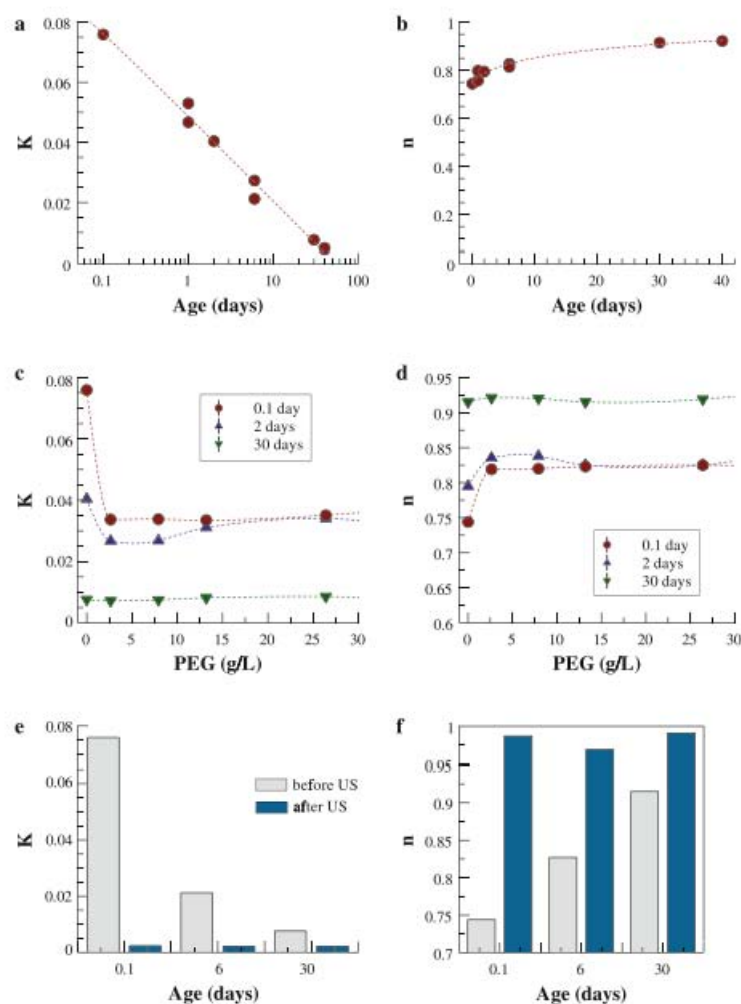
Figure 3.4: Best fit parameters n and K obtained by fitting experimental flow curves by the power law rheological model (Eq. 3.1). **a** and **b**: effect of ageing **c** and **d**: effect of PEG addition **e** and **f**: effect of ultrasonication. Rheometer temperature=20 °C. The size of the symbols is large than the standard deviation. The dotted lines are shown for visual aid

The decrease of viscosity on ageing is explained by a progressive reorganization of the aggregates towards a more compact packing because the slow peptization will gradually increase the surface charge of the particles decreasing the sticking probability. It was observed that when PEG was first added, it induced a marked decrease of the sol viscosity (Figure 3.4). This effect has been already reported both for PEG 2000 [196] and Pluronic F-127 [197]. It was explained by assuming that polymer adsorption on the titania particles induces a stabilization by steric effect which in turn decreases the sticking probability, and leads to progressive reorganization of the aggregates toward a more compact packing. This also explains the decrease of this effect which, upon ageing vanishes completely .

Addition of acetylacetone to TTIP, prior to hydrolysis, gives a sol composed only of

anatase crystallites, having a viscosity similar to an aged sol, and exhibiting Newtonian behaviour. This is consistent with small and compact aggregates and can be explained by adsorption on the surface of anatase crystals, of acetylacetone released during the hydrolysis of the complex. Ultrasonication is a very efficient way to break the aggregates (Figure 3.4). The final aggregate size is the same, irrespective of the age of sol, and the low viscosity observed is in agreement with the particle size given by DLS (~ 20 nm) which corresponds to aggregates containing just a few primary particles. This was already reported by Xu et al. [198].

3.4   Characterization of TiO$_2$ powder

3.4.1   Density

The densities of selected powder, measured with a helium pycnometer, are reported in Table 3.1. The densities of the powder calcined at low temperature (70 °C) were significantly lower ($\rho \sim 3.0$) than the value calculated from the crystal cell parameters ($\rho \sim 4$) for a mixture containing 70% anatase ($\rho = 3.90$) + 30% brookite ($\rho = 4.12$).

Table 3.1: Effect of calcination temperature and polymer concentration on the density of titania powder

Calcination temperature (°C)	PEG (g/l)	BET specific surface area (m^2/g)	Experimental density (g/cm^3)	Relative error (%)	Crystal phases	Crystal density (g/cm^3)
70	0	228	3.278	0.21	A,B	3.90
70	0	196	3.016	0.02	A,B	3.90
200	0		3.190	0.20		
300	0	138	3.510	0.04	A,B	3.94
500	0	63	3.736	0.12	A,B,R	3.97
500	31	124	3.617	0.06	A,B,R	3.94
500	36	131	3.555	0.03	A,B,R	3.94
500	46	117	3.610	0.02	A,B,R	3.95
500	64	101	3.701	0.31	A,B,R	3.95
800	0	1	4.203	0.05	R	4.25

The density increased with the temperature of thermal treatment (Figure 3.5), however even after calcination at 500 °C, the experimental densities were still lower than the values calculated from cell parameters. The addition of PEG did not seem to have a significant effect on the density, but good correlation was observed between density and specific surface

area, Figure 3.5(b). Non-peptized sols gave powders having higher density than peptized sols (first row in Table 3.1).
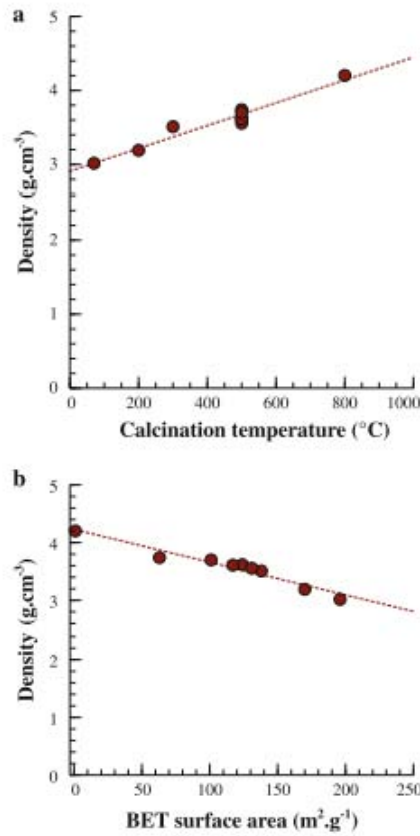
Figure 3.5: Correlation between density of titania powders and (a) calcination temperature (b) specific surface area (BET). The size of symbols is larger than the standard deviation. The dotted lines are shown for visual aid

It was noted that the experimental density of the powders obtained was lower than the crystal density, Table 3.1. One cause could be the presence of closed porosity. However, the good correlation observed between experimental density and the BET specific surface area, Figure 3.5(b) suggests that experimental density is lower because of the presence of a layer at the surface of the particles, containing adsorbed water and hydroxyl groups. The global density(ρ), of this material will be:

$$\rho = \frac{m_{layer} + m_{crystal}}{V_{layer} + V_{crystal}} \tag{3.2}$$

For 1 g of material ,

$$m_{layer} + m_{crystal} = 1 and, V_{crystal} = \frac{m_{crystal}}{\rho_{crystal}} \tag{3.3}$$

which leads to,

$$\rho = \frac{1}{V_{layer} + \frac{1-m_{layer}}{\rho_{crystal}}} \qquad (3.4)$$

We can consider that m$_{layer}$ is the mass loss obtained by thermal analysis (though a part of this has been attributed to the removal of hydroxyl groups inside the particles, which also contributes to the lowering of density). For a non-peptized sample, it corresponds to water, and V$_{layer}$= m$_{layer}$ $\sim$ 0.08g (8%) which leads to $\rho \sim$ 3.23. This is close to the experimental density ρ_{exp} = 3.28. For a peptized sample, the mass loss is given by thermal analyses, the sum of water and nitrate decomposition, and m$_{layer}$ $\sim$ 0.23g (23%). However, we do not know the density of this layer containing water and nitrate. Assuming that V$_{layer}$ = m$_{layer}$, leads to $\rho \sim$ 2.37, which is obviously very low when compared to the measured density ($\sim$ 3.0).

From the pore volume of the powders, V$_{pore}$ and their density(ρ) it is possible to calculate their porosity by the relation:

$$\epsilon = \frac{voulume\ of\ pores}{total\ volume} = \frac{V_{pore}}{V_{pore} + \frac{1}{\rho}} \qquad (3.5)$$

3.4.2   Adsorption isotherms for specific surface area and porosity

Specific surface area and pore size distribution were computed from the nitrogen adsorption isotherms recorded at 77.4 K. The specific surface areas were calculated using the Brunauer-Emmett-Teller (BET) method [162] and the pore size distributions (PSD) were computed with software based by the NLDFT method [163]. The experimental values obtained with powders calcined at various temperatures are reported in Figure 3.6.

Calcination temperature (°C)	BET			Isotherm		Porosity	NLDFT		
	Surface area (m^2/g)	C	CC	Pore vol (cm^3/g)	D_h (nm)		Fit error (%)	S_{cum} (m^2/g)	V_{cum} (cm^3/g)
50	236	181	0.99987	0.12	2.0	0.27	0.23	236	0.11
100	237	150	0.99996	0.12	2.0		0.57	249	0.11
200	223	60	0.99997	0.13	2.3	0.29	0.57	203	0.12
300	221	33	0.99996	0.14	2.5	0.33	0.40	169	0.14
400	124	55	0.99994	0.13	4.2	0.32	0.47	98	0.13
500	62	61	0.99998	0.08	5.2	0.24	0.71	58	0.08

Figure 3.6: Effect of the calcination temperature on the textural characteristics of powder samples prepared in standard conditions

The isotherms and their corresponding PSD are plotted in Figure 3.7. Powders heated at low temperature contained small mesopores and 30% of micropores, with pore sizes no

larger than 5 nm. Above 300 °C these micropores were eliminated, the pore distribution became almost symmetrical, in the range of 3 - 6 nm. The micropore elimination was accompanied by a small decrease in specific surface area and a significant decrease of the BET C constant. The increase of the average pore size (from 3 to 4 nm) produced an increase in the pore volume.
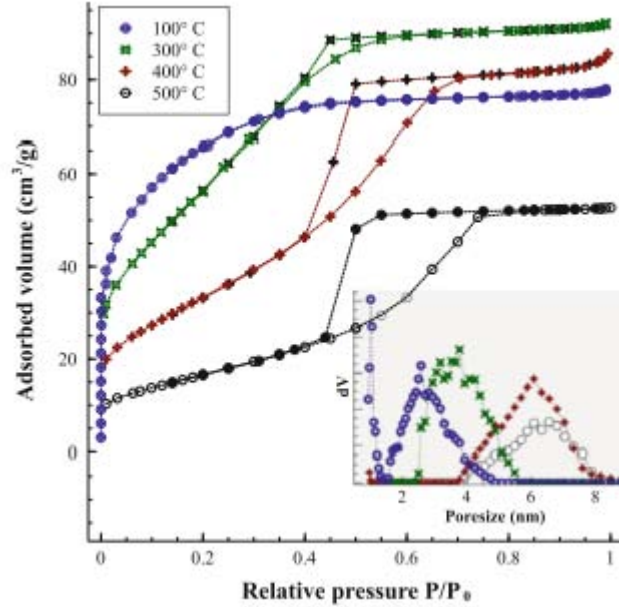
Figure 3.7: Effect of calcination temperature on N2-adsorption isotherms (bold symbols correspond to the desorption branch) and PSD (inset graph) computed from N2-adsorption isotherms by the NLDFT method [163] (with Quantachrome Autosorb-1 software using silica equilibrium transition kernel at 77 K, based on a cylindrical pore model)

Heating above 300 °C, produced first, a shift of the PSD towards larger pores (at 400 °C), then followed by a decrease in the porosity. Both these effects induced a significant decrease in specific surface area. The specific surface area S_w (in m²/g) of a material composed of spherical particles, all having the same diameter D (in nm), was calculated by the equation:

$$S_w = \frac{6000}{\rho D} \tag{3.6}$$

where, ρ - density of the crystallites (in g/cm³).

Using the cell parameters, the crystallite size and the polymorph composition obtained from the analysis of XRD patterns, it was possible to calculate the specific surface area. When these calculated values, spanning a range from 0 to about 200 $m^2 g^{-1}$, were plotted against the BET surface area for a set of 25 powders, surprisingly despite the large approximation inherent in this kind of calculation, a linear correlation was observed (coefficient

Peptization time (min)	BET			Isotherm		NLDFT		
	Surface area (m^2/g)	C	CC	Pore vol cm^3/g	D_h (nm)	Fit error (%)	S_{cum} (m^2/g)	V_{cum} (cm^3/g)
0	34	179	0.99971	0.08	9.4	0.44	30	0.05
60	122	167	0.99956	0.09	3.0	0.13	109	0.08
240	238	51	0.99993	0.15	2.5	0.33	202	0.14

Figure 3.8: Effect of the peptization time on the textural characteristics of powder samples
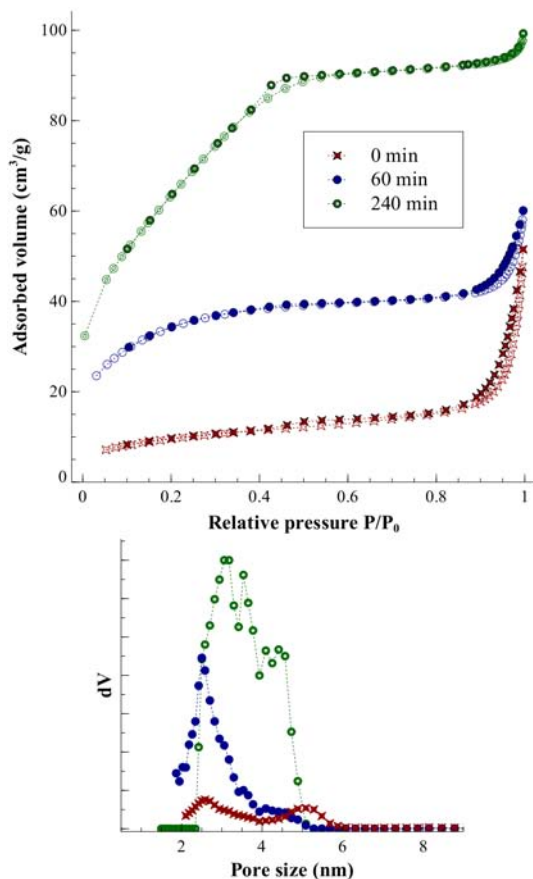
Figure 3.9: Effect of peptization time on:(a) N2-adsorption isotherms (bold symbols correspond to the desorption branch).(b) PSD computed from N2-adsorption isotherms by the NLDFT method (with Quantachrome Autosorb-1 software using silica equilibrium transition kernel at 77 K, based on a cylindrical pore model)

correlation= 0.988). The slope of the regression line was approximately 0.76, which possibly meant that only 76% of the crystallite surface was accessible to adsorbent molecules. In parallel to the XRD study reported earlier, the effect of peptization time on the surface and porosity of the powder had also been examined. However, it should be mentioned that the samples were all degassed at 300 °C before the adsorption analysis. The main results are summarized below in Figure 3.8.

The isotherms and their corresponding PSD are shown in Figure 3.9. The first sample, taken at the end of hydrolysis, contained only a few small mesopores, in the range of 2–6 nm. The main nitrogen uptake (66%) was observed above a relative pressure of 0.9, which corresponded to slit pores with pore size larger than 20 nm. This porosity probably resulted from the stacking of the large particles observed on TEM images (Figure 3.2). After 60 min of peptization, small mesopores were formed, with a sharp peak centered at 3 nm. At this point, significant adsorption (30%) above the relative pressure of 0.9 was still observed. After 240 min, there was a strong increase in the volume of mesopores associated with a shift towards larger dimensions. The adsorption above the relative pressure of 0.9 was still present, but it represented only 6% of the total pore volume.

The powder resulting from the drying of the peptized sols at low temperature (<100 °C), have a pore volume of 0.12 cm³/g (Figure 3.6) and a density of 3 g/cc (Table 3.1). This gives a porosity of 0.27. This value is very close to the porosity of a material resulting from the close packing of spherical particles (0.26). In addition, the pore size distribution is also in very good agreement with a similar material having a spherical shape with a diameter of 6 nm, since we observed two peaks at about 1 and 2.5 nm (Figure 3.7), corresponding, respectively to the tetrahedral (6 x 0.225 $\sim$ 1.4) and octahedral (6 x 0.414 $\sim$ 2.5) holes. Thus, as already reported by Xu and Anderson [172, 198], during the drying stage, the particles arrange themselves to form a compact material. Due to electrostatic repulsion, which reduces sticking probability, particle aggregation follows a reaction-limited model and produces dense aggregates. When the powders are heated in air, there is an increase in porosity up to a temperature of 300 °C ($\epsilon = 0.33$) because of the loss of weakly bonded water, as well as, dehydroxylation, during reorganization of the particles. However, the gain in porosity remains limited. Above 300 °C the surface hydroxyls, which prevent direct contact between crystallites, are almost eliminated. A progressive growth of the crystallites occurs inducing a reorganization of the particles accompanied by shrinkage in the porosity. Finally, without additives, it would be quite difficult to obtain porous films from aqueous sols stabilized by electrostatic repulsion since they always give compact films on drying. Xu and Anderson [172] have shown that, in reducing the repulsive energy by increasing the pH, the mechanism of aggregation follows a diffusion-limited model, resulting in spongy structures with porosity which can exceed 0.5. This of course, leads to unstable sols due to the reduction in repulsive energy. To prepare coatings with controlled porosity from stable hydrosols, a strategy comprises of adding a porogen which adsorbs at the surface of the particles. During the drying step, the porogen will coat the particles and with a suitable calcination process, the porosity left by polymer removal can be retained.

As the coordination number is decreased, thermal stabilization is improved [199]. For example, addition of polyethylene glycol (PEG) in titania hydrosols can significantly im-

prove the surface area and the porosity of the powders obtained after calcination [183, 200]. Addition of PEG induces an increase in the number of pores, a shift towards larger pore size, and a broadening of the pore size distributions. But, there is an optimum value for the amount of PEG, above which, the porosity and the surface area decrease [201]. Furthermore, another advantage of addition of PEG is the elimination of the film cracking and peeling off the substrate that is very often observed, especially on steel substrates, as soon as the film exceeds a certain critical thickness [150, 200]. If the porogen is a non-ionic surfactant, like block copolymers, self-assembly (spontaneous formation of complex hierarchical structures from pre-designed building blocks can occur. This allows an even better control of the porosity. For example, addition of Pluronic F-127 provides higher surface area and porosity than an equivalent amount of PEG2000 [201]. The SEM images presented in Figure 3.10 shows the strong textural differences between coatings synthesized by dip-coating (glass substrate) the sols containing either PEG2000 or F-127. With the copolymer, the large porosity resulting from the formation of micelles is clearly visible. Another advantage of polymer addition occurs when the polymer is strongly anchored to the surface of the particles because the sol stability is improved through steric stabilization [202].

3.4.3   Thermal analysis

Figure 3.11 shows the thermogram recorded for a powder dried at 40 °C prepared without acid addition.The total mass loss is about 8%. Mass spectrometry analysis of the evolved gas reveals only traces of carbon species (CO_2), thus, the mass loss is essentially a loss of water. DTG curve shows that the dehydration process occurs in two steps at least. However, a far better fit of the DTG curve is obtained if a third peak is added. Based on the shape of the first peak, Gaussian-type peak was used for the fitting; the peak parameters are reported in Figure 3.12. As all the peaks start at the beginning they most likely correspond to parallel processes. The first peak has a maximum at 106 °C and ends just after 200 °C. In this experiment it corresponds to a mass loss of less than 3%, however, the area of this peak is closely related to the drying time and temperature. This low temperature dehydration is usually attributed to the removal of weakly adsorbed water.

The second process, representing a mass loss of 2.9%, gave a broader peak with a maximum at 185 °C which ended at ~ 350 °C. The water released in this step corresponded to the dehydroxylation of the particle surface. A quick decrease in surface area and porosity was observed from a temperature close to the elimination of these hydroxyl species, Figure 3.6. From the amount of water lost in this step, the number of hydroxyl group per Ti atom
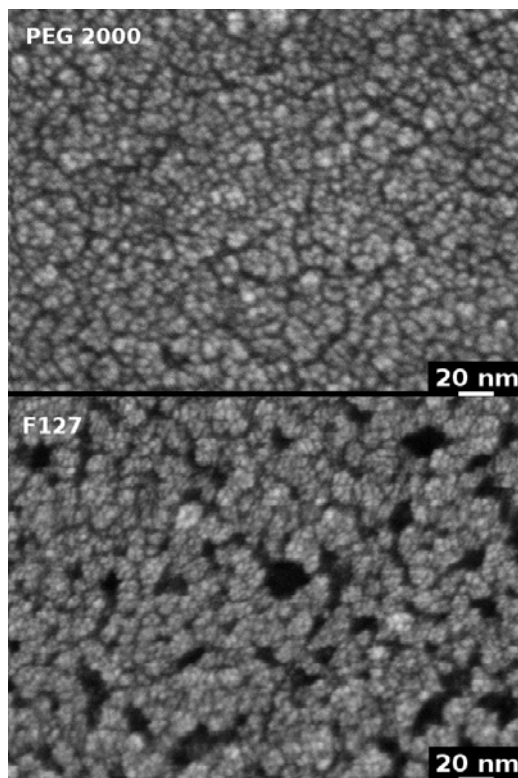
Figure 3.10: SEM images of the top surface of a glass plate coated with a TiO$_2$ sol containing PEG 2000 (top) and Pluronic F127 (bottom). In both cases the amount of polymer corresponds to EO/Ti= 1
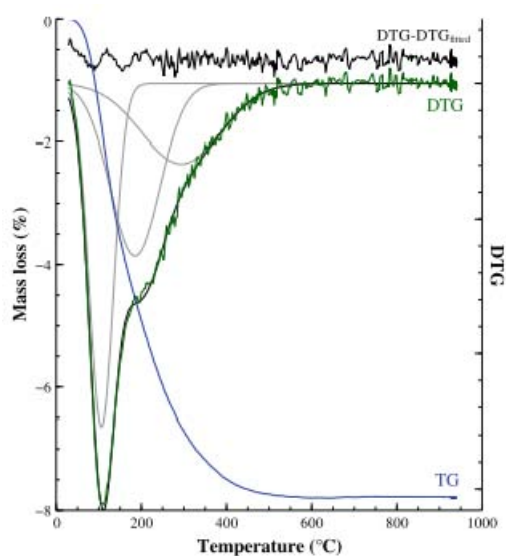
Figure 3.11: Thermogravimetric analysis of a powder dried at 40 °C and prepared without acid addition. This plot shows the experimental TG and DTG curves as well as the best fit of the DTG curve by three parallel dehydration processes. The top curve corresponds to the difference between the experimental curve and the sum of peaks.Gaussian-type peak was used for the fitting

was calculated; we found OH/Ti ~ 0.28. Now from this value and the specific surface area, an approximate surface OH density was calculated. Using a surface area of 330 m^2/g (value calculated with equation 3.6 for particles having a density of 3 g/cm^3 and a diameter of 6 nm) we found 6.3 OH/nm^2. This value corroborated with those already reported for large surface area titania ($\sim$6 OH/nm^2) [203].

The third process gave a very broad peak (FWHM $\sim$ 220 °C). Its maximum was close to 300 °C and it ended at 550 °C. We attributed this peak to the slow removal of the hydroxyl groups trapped inside the particles. This is a limited diffusion process which ends with anhydrous titania. As already reported in a previous study [197], the removal of these remaining defects corresponded precisely to the temperature, where the exothermic crystallization into rutile, from the metastable anatase and brookite phases was observed. The presence of OH groups inside the crystalline structure had already be related to the titanium deficiency given by the Rietveld refinement [186]. It could also explain why the density of powders calcined at 500 °C was lower than that calculated from the cell parameters, Table 3.1. Thermal analysis of a peptized sol had been reported before [197] and in this case the mass loss was the sum of nitrate decomposition and water loss.

Peak no.	T_{max} (°C)	FWHM (°C)	Area (in wt% water)
1	106	67	2.8
2	185	137	2.9
3	294	220	2.1

Figure 3.12: Peak parameters for the decomposition of DTG curve of non-peptized sample of figure 3.11

3.5   Conclusions

To synthesize, by hydrolysis of the titanium isopropoxide, nanocrystallite dispersions of titania in water, suitable for coatings and having long-term stability (more than 1 year) in terms of polymorphic composition, crystallite and agglomerate size, the best experimental conditions were found to be:

1. $H_2O/Ti = 50$-100,

2. $H^+/Ti \sim 0.2$, HNO_3 preferred to HCl,

3. peptization temperature allowing the fast removal of isopropanol by evaporation ($\sim$ 80 °C).

In these conditions, the sols are composed of aggregates, with a chainlike structure, of anatase ($\sim$90%) and brookite crystallites (5–6 nm).

Upon ageing a progressive reorganization of the aggregates towards a more compact packing occurred, accompanied by a marked decrease in the viscosity. These aggregates could be quickly broken by ultrasonication. Stable sols composed solely of anatase crystallites (4 nm) were prepared by partially complexing the TTIP by acetylacetone before hydrolysis.

It was not possible to produce porous films from these sols, stabilized by electrostatic repulsion, as a result of the close packing of the particles during the drying stage. However, coatings with controlled porosity could be prepared from these hydrosols through the addition of porogens such as PEG or block copolymers (Pluronic F-127).

Chapter 4

TiO$_2$ synthesis: MOCVD

Contents

In this chapter, the effect of different MOCVD process parameters such as, distance between precursor source in the reactor chamber and the substrate (d), coating temperature (T_c), reactor pressure (P) and precursor temperature (T_p) were investigated using a statistical tool called the Design of Experiment. For this study the properties of the coating that were investigated were mass, thickness, roughness, polymorphic composition and crystallite size. The goal behind this study was to determine, quantitatively, the way in which each parameter affected any (quantifiable) coating property.

4.1 Effect of process parameters via DoE

The effect, on each response of the coating, by the process parameters under study, was calculated using equation 2.12. It was earlier discussed in Chapter 2 that as a fractional plan was used instead of a complete plan, the effect of the 4th process parameter (T_p) was statistically confounded. The confounded effects are detailed below,

$$a'_d = a_d$$
$$a'_{T_c} = a_{T_c}$$
$$a'_P = a_P$$
$$a'_{dT_c} = a_{dT_c} + a_{PT_p}$$
$$a'_{dP} = a_{dP} + a_{T_cT_p}$$
$$a'_{T_cP} = a_{dT_p} + a_{T_cP}$$
$$a'_{dT_cP} = a_{T_p}$$
$$a'_0 = a_0$$

For each response, the effect of the process parameter with the least significant value is ignored in the confounded interaction effects (mentioned above). This allows the identification of the most important interaction, for each confounded interaction. In the following sections, each response is treated individually to, quantitatively, determine the process parameter that is most significant for each response.

4.1.1 Effect on mass

The experimental results of the mass response (Y_m) are reported in Table 4.1 and the values for the effects of the process parameters, on the mass response, are reported in Table 4.2.

The standard deviation of 3 measures of a single sample (σ_m) and the sample standard deviation of mass of 3 samples obtained under similar experimental conditions, σ_e are also reported in Table 4.1.

Table 4.1: Experimental results for mass response

Trial run no.	d (mm)	T_c (°C)	P (Torr)	T_p (°C)	Y_m (10^{-4}g)	σ_m (10^{-4}g)	σ_e (10^{-4} g)	$D_m = \frac{\sigma_m+\sigma_e}{Y_m}$ (%)
1	50	350	2.5	37	5.20	0.1	0.1	4
2	70	350	2.5	42	6.90	0.3	0.1	6
3	50	600	2.5	42	49.3	0.2	0.1	0.5
4	70	600	2.5	37	24.2	0.2	0.1	1
5	50	350	20	42	7.70	0.2	0.1	4
6	70	350	20	37	7.4	0	0.1	1
7	50	600	20	37	5.17	0.2	0.1	6
8	70	600	20	42	5.5	0.6	0.1	13

Table 4.2: The effect of the parameters on mass; d= distance, T_c= deposition temperature, P= reactor pressure, T_p= precursor temperature, a'_0= effect at centre of range

Designation of effect a'	Effect on mass a'(mass) (10^{-4})
a'_d	-2.9
a'_{T_c}	7.10
a'_P	-7.50
a'_{dT_c}	-3.30
a'_{dP}	2.90
a'_{T_cP}	-8.20
a'_{dT_cP}	3.40
a'_0	13.9

From Table 4.2 we see that the effect of distance, a'd is very small therefore, it's contribution is ignored in the confounded effect of the interactions,

$a'_d = a_d$

$a'_{T_c} = a_{T_c}$

$a'_P = a_P$

$a'_{dT_c} = a_{PT_p}$

$a'_{dP} = a_{T_cT_p}$

$a'_{T_cP} = a_{T_cP}$

$a'_{dT_cP} = a_{T_p}$

$a'_0 = a_0$

These terms are substituted in equation 2.13 and so, the final equation for the mass

model is,

$$Y(model)_{mass} = a_0 + a_d d + a_{T_c} T_c + a_P P + a_{PT_p} PT_p + a_{T_c T_p} T_c T_p + a_{T_c P} T_c P + a_{T_p} T_p \quad (4.1)$$

The validation of the model is performed by first comparing the theoretical model response and the experimental results of experiments performed under similar conditions, Table 4.3. This is compared to the highest value of 'D$_m$' in Table 4.1, in this case 13%. The relative difference between the model and the experimental values is comparable with the highest standard deviation for the mass response and hence, the model is validated.

Table 4.3: Validation for mass response

Validation run no.	d (mm)	T_c (°C)	P (Torr)	T_p (°C)	Y_{expt} (10^{-3}g)	Y_{model} (10^{-3}g)	$Y_{difference}$ (%)
1	60	475	10	40	1.37	1.54	12
2	60	475	12	37	0.86	1.01	17
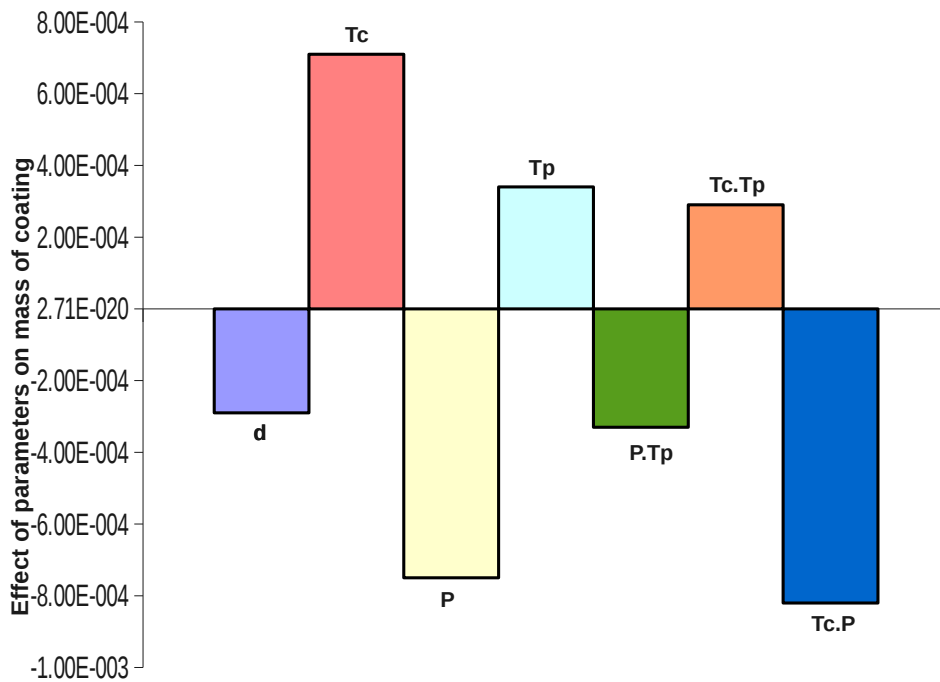
Figure 4.1: Effect of process parameters on mass of coating

Figure 4.1 clearly shows that the coating temperature and reactor pressure have the highest influence on the mass. They appear to have an equal, though opposite, influence

on the mass of the coating, i.e. an increase in the coating temperature leads to an increase in the mass, while the increase in the reactor pressure leads to a decrease in the mass. The interaction between the coating temperature and pressure is also important. Here, it means that the effect that the coating temperature has at low pressure is different from that at high pressure, and vice-versa.

The conclusions of the DoE are backed by literature: Precursor mole fraction, which is inversely proportional to reactor pressure (equation 2.2 in Chapter 2) is reported to affect the growth rate, in the absence of H$_2$O in gas mixture. At low mole fractions ($\sim 10^{-5}$), the growth rate (read mass) was reported to increase with deposition temperature and reach a maximum at 650 °C. At higher mole fractions (read lower pressures) ($\sim 10^{-4}$) this growth rate was reported to be an order higher, and here, the maximum growth rate was achieved at 600 °C (Figure 4.2). At temperatures $\leqq$ 600 °C, the reactions take place in the kinetic regime, while at higher temperatures ($\geqq$ 650 °C), the diffusion regime becomes narrow and is taken over by a depletion regime [124]. Considering the curve at lower molar fraction (higher pressure), the difference between the highest point and the lowest point is $\sim$1.5, while at higher mole fraction (lower pressure) the difference is larger ($\sim$ 3 times).This confirms the conclusion that pressure interacts differently at different temperatures.
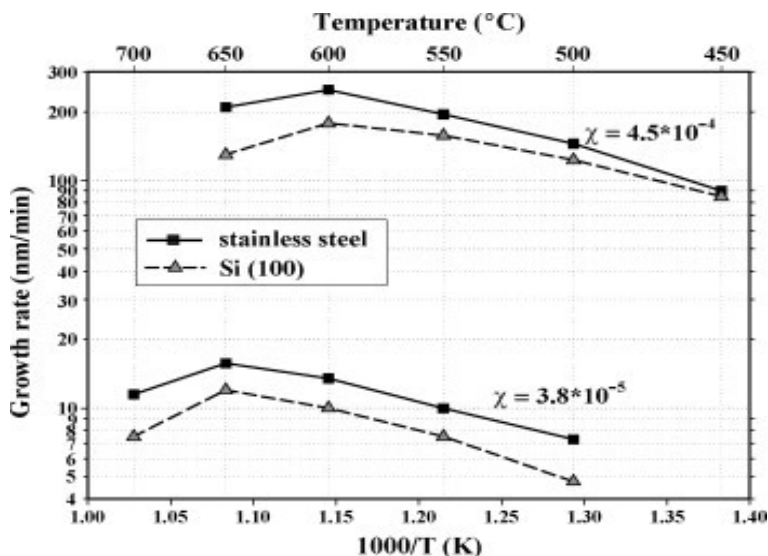
Figure 4.2: Arrhenius plot of the growth rate on Si(100) and stainless steel substrates for two TTIP mole fractions: 3.8×10^{-5} and 4.5×10^{-4} (without oxidizing reagent [124].

The distance and precursor temperature (T$_p$) are shown (Figure 4.1) to have a lower impact on the mass of the coating. The further away the substrate is from the precursor source the higher the volume available for gas-phase reactions (provided this volume is

heated) and consequently, the lower the mass. In our study, since the range between which the distance was varied is not large, the effect on mass is not pronounced.

The increase in T_p leads to an increase in the mole fraction of the precursor, and hence, the higher the mole fraction, the higher the mass for a specified period of time. As T_p was varied over a small range, it's effect is not very perceptible.

The effect of the interaction between the pressure and precursor temperature is small; Both the pressure and T_p affect the mole fraction, though the effect of pressure overshadows that of T_p since the range over which the pressure was varied is larger than that of T_p, thereby explaining the inverse relation this interaction has with mass. The effect of the interaction between deposition temperature (T_c) and T_p is small, again, this could be attributed to the small range of T_p.

4.1.2   Effect on thickness

The experimental results of the thickness response are reported in Table 4.4 and the values for the effects of the process parameters, on the thickness response, are reported in Table 4.5. The standard deviation of 3 measures of a single sample (coating on Si wafer) from a SEM cross-section micrograph (σ_m) and the standard deviation of thickness of 5 samples obtained under similar experimental conditions (σ_e) are also reported.

Table 4.4: Experimental results for thickness response

Trial run no.	d (mm)	T_c (°C)	P (Torr)	T_p (°C)	Y_t (nm)	σ_m (nm)	σ_e (nm)	$D_t = \frac{\sigma + \sigma_e}{Y_t}$ (%)
1	50	350	2.5	37	760	15	10	3
2	70	350	2.5	42	1000	120	10	13
3	50	600	2.5	42	12900	500	10	4
4	70	600	2.5	37	13200	800	10	6
5	50	350	20	42	2300	50	10	2.5
6	70	350	20	37	1700	130	10	8
7	50	600	20	37	2300	100	10	5
8	70	600	20	42	2500	250	10	10

Since the effect of distance, a'd is very small (Table 4.5), it's contribution is ignored in the confounded effect of the interactions,

$a'_d = a_d$

$a'_{T_c} = a_{T_c}$

$a'_P = a_P$

$a'_{dT_c} = a_{PT_p}$

Table 4.5: The effect of the parameters on thickness

Designation of effect a'	Effect on thickness a'(thickness)
a'$_d$	0.0004
a'$_{T_c}$	3.1363
a'$_P$	-2.3793
a'$_{dT_c}$	0.1054
a'$_{dP}$	-0.1217
a'$_{T_cP}$	-2.9403
a'$_{dT_cP}$	0.1042
a'$_0$	4.577

a'$_{dP}$ = a$_{T_cT_p}$

a'$_{T_cP}$ = a$_{T_cP}$

a'$_{dT_cP}$ = a$_{T_p}$

a'$_0$ = a$_0$

These terms are substituted in equation 2.13, and so, the final equation for the mass model is,

$$Y(model)_{thicknesss} = a_0 + a_d d + a_{T_c}T_c + a_P P + a_{PT_p}PT_p + a_{T_cT_p}T_cT_p + a_{T_cP}T_cP + a_{T_p}T_p \quad (4.2)$$

The relative difference between the model and the experimental values is comparable with the highest standard deviation for the thickness response (13%), and hence, the model is validated.

Table 4.6: Validation for thickness response

Validation run no.	d (mm)	T$_c$ (°C)	P (Torr)	T$_p$ (°C)	Y$_{expt}$ (μm)	Y$_{model}$ (μm)	Y$_{difference}$ (%)
1	60	475	10	40	3.95	4.59	16
2	60	475	12	37	4.3	5.03	17

Figure 4.3 shows that the deposition temperature and pressure have the strongest influence on the thickness of the coating, and also that similar to the mass response the effect of the deposition temperature at low pressure is different than at high pressure. The deposition temperature is directly proportional to the film thickness as a result of the increase in crystal growth rate which is brought on by a change in morphology from a compact structure at 350 °C to a columnar structure at 600 °C [124, 166]. Increase in mole fraction
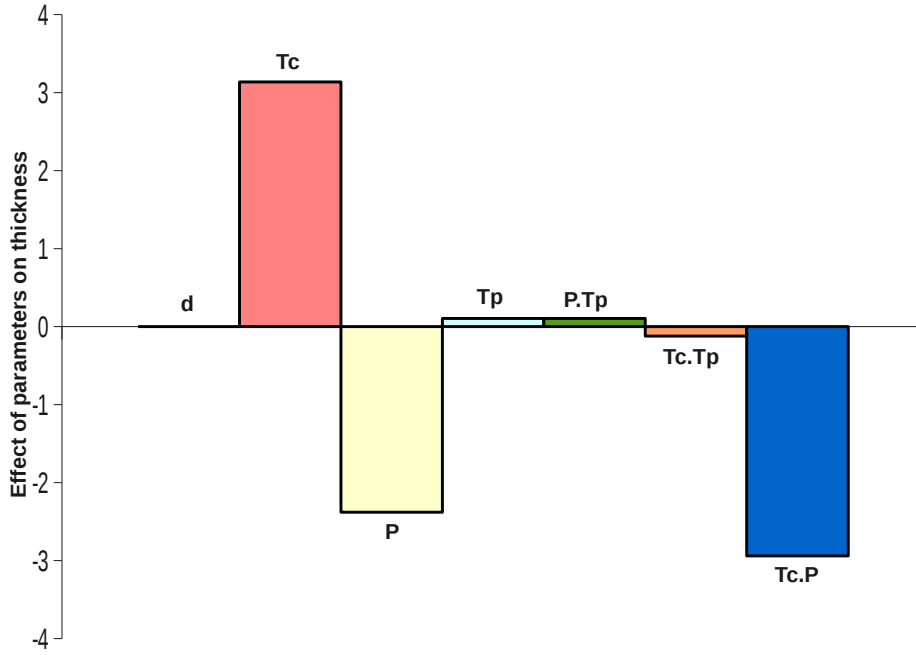
Figure 4.3: Effect of process parameters on thickness of coating

(decrease in pressure) 76 to 1035×10^{-6} leads to higher growth rate $2.3 - 58$ nm/min [166] and therefore, higher thickness. The distance and T_p and their respective interactions had no effect on the thickness, most likely, due to their small range.

4.1.3 Effect on roughness

The experimental results of the roughness response are reported in Table 4.7 and the values for the effects of the process parameters, on the roughness, are reported in Table 4.8. The standard deviation of 3 measures of a single sample (σ_m) and the sample standard deviation of roughness of 5 samples obtained under similar experimental conditions (σ_e) are reported.

Since the effect of precursor temperature, a'$_{dTcP}$ (i.e. a'$_{T_p}$) is very small (Table 4.2), its contribution is ignored in the confounded effect of the interactions,

$\text{a'}_d = \text{a}_d$

$\text{a'}_{T_c} = \text{a}_{T_c}$

$\text{a'}_P = \text{a}_P$

$\text{a'}_{dT_c} = \text{a}_{dT_c}$

$\text{a'}_{dP} = \text{a}_{dP}$

$\text{a'}_{T_cP} = \text{a}_{T_cP}$

$\text{a'}_{dT_cP} = \text{a}_{T_p}$

Table 4.7: Experimental results for roughness response

Trial run no.	d (mm)	T_c (°C)	P (Torr)	T_p (°C)	Y_r (μm)	σ_m (μm)	σ_e (μm)	$D_r = \frac{\sigma + \sigma_e}{Y_r}$ (%)
1	50	350	2.5	37	0.0462	0.003	0.003	13
2	70	350	2.5	42	0.0314	0.005	0.002	22
3	50	600	2.5	42	0.3675	0.003	0.022	7
4	70	600	2.5	37	0.3924	0.023	0.023	12
5	50	350	20	42	0.0726	0.006	0.004	14
6	70	350	20	37	0.0481	0.004	0.003	14
7	50	600	20	37	0.1143	0.001	0.007	6
8	70	600	20	42	0.1308	0.005	0.008	10

Table 4.8: The effect of the parameters on roughness; d= distance, T_c= deposition temperature, P= reactor pressure, T_p= precursor temperature, a'$_0$= effect at centre of range

Designation of effect a'	Effect on roughness a'(roughness)(10^{-3})
a'$_d$	0.263
a'$_{T_c}$	101
a'$_P$	-59
a'$_{dT_c}$	10.1
a'$_{dP}$	-2.26
a'$_{T_cP}$	-69.7
a'$_{dT_cP}$	0.163
a'$_0$	150

a'$_0$ = a$_0$

These terms are substituted in equation 2.13, and so, the final equation for the mass model is,

$$Y(model)_{roughness} = a_0 + a_d d + a_{T_c} T_c + a_P P + a_{dT_c} dT_c + a_{dP} dP + a_{T_cP} T_c P + a_{T_p} T_p \quad (4.3)$$

Table 4.9: Validation for roughness response

Validation run no.	d (mm)	T_c (°C)	P (Torr)	T_p (°C)	Y_{expt} (μm)	Y_{model} (μm)	$Y_{difference}$ (%)
1	60	475	10	40	0.156	0.10	56
2	60	475	12	37	0.144	0.31	54

In the 1st validation run, the Y_{model} and Y_{expt} are on the same scale (156 nm and 100
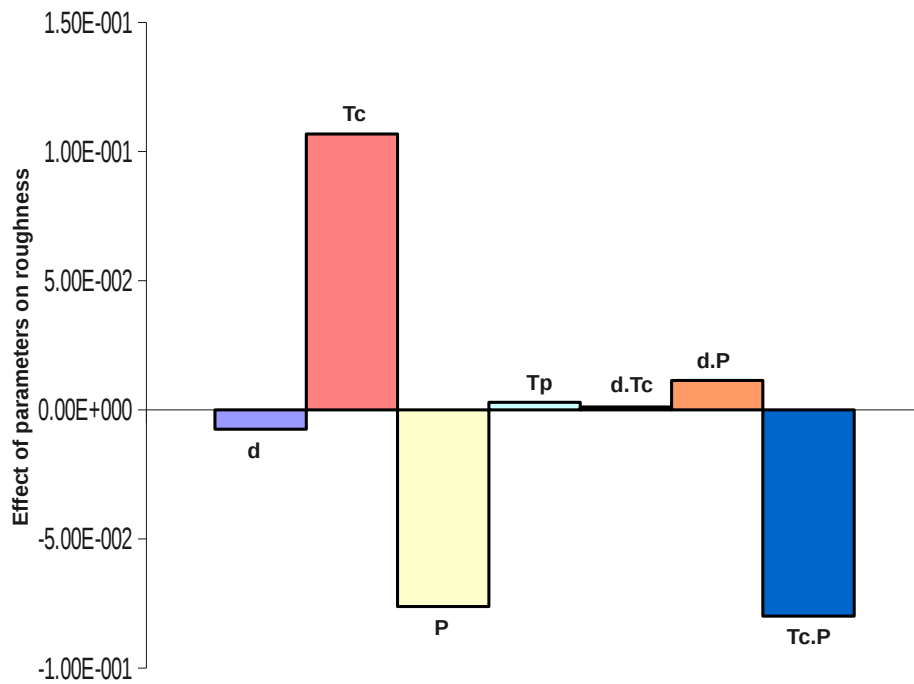
Figure 4.4: Effect of process parameters on roughness of coating

nm) even though the difference appears large. On the other hand, for the 2nd validation run this difference is more significant (144 and 310 nm). In the second case, this large difference is attributed to the inhomogeneous roughness of the coating as seen in Figure 4.6. Since the roughness model is estimated for a coating with a homogeneous roughness, this inhomogeneity in the sample causes a large deviation from the model. In light of the above explanations, this model may be considered valid.
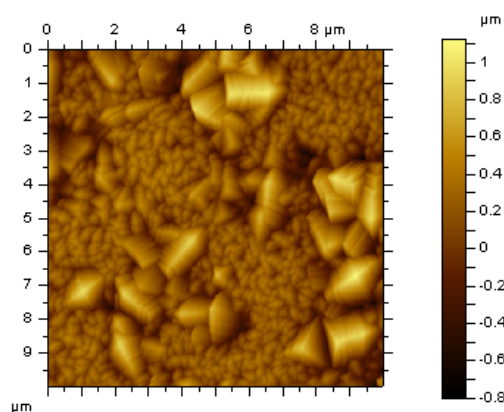
Figure 4.5: AFM scans (10μm$\times10\mu$m) showing a large inhomogeneity in the coating of the 2nd validation run

From Figure 4.4, the coating temperature and reactor pressure are significantly more

influential on the roughness of the coating than the other parameters, here again, we see
that the coating temperature is directly proportional to the roughness of the coating while
the reactor pressure is inversely proportional. This is possibly due to the sintering of the
smaller grains into larger grains, with the increase in coating temperature. The increase
in coating temperature leads to columnar structures in the coating, consisting of jagged
edges (Figure 4.6(a)), while at lower coating temperatures, the coatings are flatter and
more compact (Figure 4.6(c). This difference in roughness is perhaps linked to the growth
rate: if the growth rate is slow then particles have time to arrange themselves into a more
stable arrangement while at higher growth rate it is possible that the particles arrange
themselves in a random manner thereby leading to higher roughness.
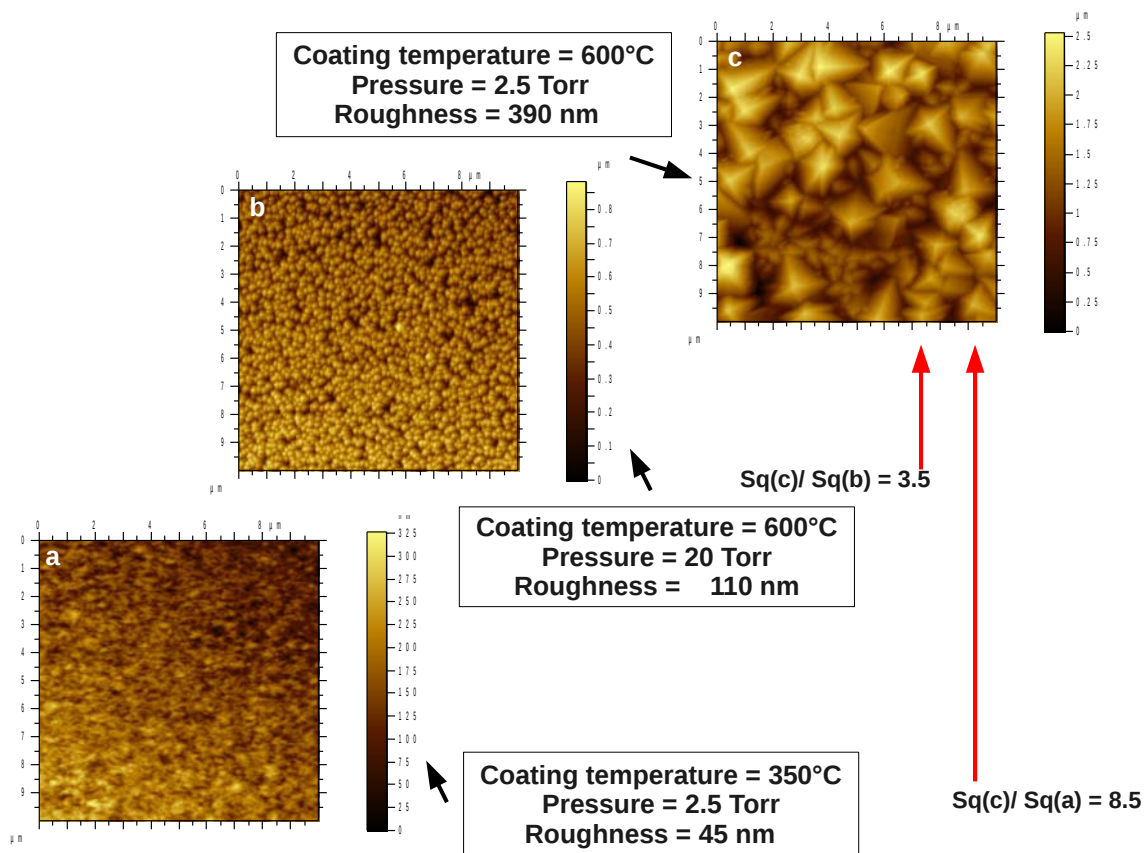
Figure 4.6: AFM scans (10μm×10μm) showing change in roughness at constant temperature
and constant pressure

Previous studies on roughness of MOCVD-TiO$_2$ films, produced in a hot-wall reactor
in a horizontal configuration, report that film roughness (R$_a$) increased from 4 to 90 nm
for corresponding film thickness ranging from 200 to 2500 nm. Below 400 nm, compact
arrangement of grains was reported to be favoured and only above 400 nm, columnar growth
begins.The TTIP molar fraction (read pressure) reportedly affects TiO$_2$ morphology. Low
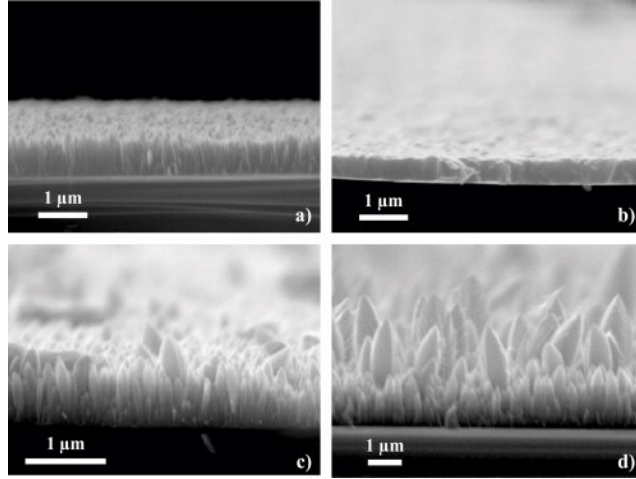
Figure 4.7: SEM micrographs of TiO$_2$ films deposited on Si(100) substrates without (a, c, d) and with (b) H2O vapor: (a) 400 °C, X=4.5 × 10^{-4}; (b) 350 °C, X=5.6× 10^{-4}, H$_2$O/TTIP=1; (c) 600 °C, X=1.8× 10^{-4}; (d) 600 °C, X=4.5× 10^{-4} [124]

mole fractions (10^{-5} - 10^{-4}) lead to uniform, dense and compact columns while higher mole fractions (10^{-3} - 10^{-2}) lead to cauliflower-like structures and elongated crystallites, therefore, increase in roughness [166] Other studies report that films produced, in a cold wall reactor in vertical configuration, at 400-450 °C, exhibit columnar structure with low roughness, whereas, films produced at 500–650 °C ,also, have columnar structure, but high roughness. Increase in time and deposition temperature was reported to increase the length of these columns, though, not uniformly, hence, higher roughness (Figure 4.7). These studies validate the trends determined by the DoE for the roughness response. The low range of d and T$_p$ might be the reason for their low influence on roughness.

4.1.4 Effect on polymorphic composition

The experimental results of the polymorphic composition response are reported in Table 4.10 and the values for the effects of the process parameters, on the polymorphic composition response, are reported in Table 4.11. The assumed standard deviation (D_p) while analysing crystallite size using Fityk is 30%.

Since the effect of precursor temperature, a'$_{dTcP}$ (i.e. a'$_{T_p}$) is very small (Table 4.2), it's contribution is ignored in the confounded effect of the interactions,

a'$_d$ = a$_d$; a'$_{T_c}$ = a$_{T_c}$; a'$_P$ = a$_P$;

a'$_{dT_c}$ = a$_{dT_c}$; a'$_{dP}$ = a$_{dP}$; a'$_{T_cP}$ = a$_{T_cP}$;

a'$_{dT_cP}$ = a$_{T_p}$ and a'$_0$ = a$_0$

Table 4.10: Experimental results for polymorphic response

Trial run no.	d (mm)	T_c (°C)	P (Torr)	T_p (°C)	$Y_{polymorphic}$ (% anatase)
1	50	350	2.5	37	100
2	70	350	2.5	42	100
3	50	600	2.5	42	87
4	70	600	2.5	37	100
5	50	350	20	42	100
6	70	350	20	37	100
7	50	600	20	37	38
8	70	600	20	42	58

Table 4.11: The effect of the parameters on polymorphic composition

Designation of effect a'	Effect on polymorphic composition a'(polymorphic)
a'_d	4.125
a'_{T_c}	-14.625
a'_P	-11.375
a'_{dT_c}	4.125
a'_{dP}	0.875
a'_{T_cP}	-11.375
a'_{dT_cP}	0.875
a'_0	85.375

These terms are substituted in equation 2.13, and so, the final equation for the mass model is,

$$Y(model)_{polymorphic} = a_0 + a_d d + a_{T_c}T_c + a_P P + a_{dT_c}dT_c + a_{dP}dP + a_{T_cP}T_cP + a_{T_p}T_p \quad (4.4)$$

Since the relative difference between the model and the experimental values is much smaller than the assumed deviation for the thickness response (30%), this model is validated.

Figure 4.8 shows that the deposition temperature and pressure are the most important parameters, and that the interaction between these two parameters is important, as well. Again, the other parameters and their interactions do not have a strong influence, possibly, because of their small range.

The polymorphic composition introduced into the DoE is the percentage of anatase

Table 4.12: Validation for polymorphic response

Validation run no.	d (mm)	T_c (°C)	P (Torr)	T_p (°C)	Y_{expt} (% anatase)	Y_{model} (% anatase)	$Y_{difference}$ (%)
1	60	475	10	40	86.7	90	4
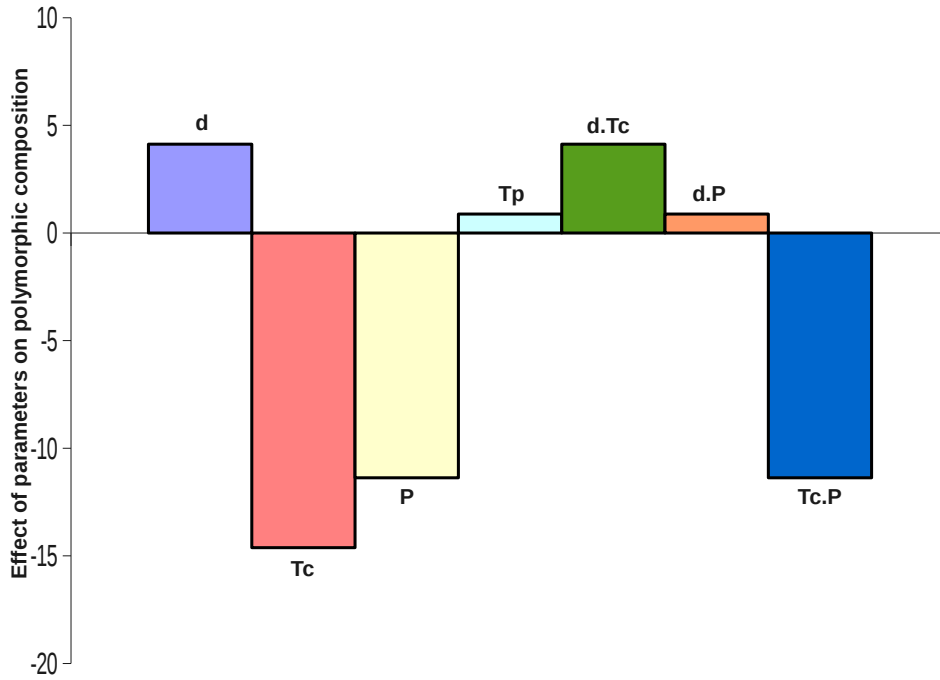
Figure 4.8: Effect of process parameters on polymorphic composition of coating

present in the coating and as anatase is a low temperature phase compared to rutile it is normal to see the decrease in the polymorphic composition (increase in rutile content) with the increase in temperature. Studies validate the conclusions from this DoE, that the molar fraction (inversely related to pressure) and deposition temperature strongly affect the polymorphic composition [166]. Other studies report that on Si(100), anatase is produced at low temperatures (500 °C) and rutile at high temperatures (700 °C). The temperature range for the growth of anatase is wider on silicon than on steel substrate. On SS-304L, presence of rutile is reported even at low temperature (450 °C). Increase in deposition temperature increases rutile concentration with only presence of rutile at 550 °C. This favoured rutile nucleation on SS-304L is probably due to the diffusion of cations from the steel substrate. Preliminary X-ray Photoelectron Spectroscopy (XPS) studies showed an absence of cation diffusion which could be attributed to the low resolution of the XPS apparatus, and hence further analyses using more sensitive apparatus should be

conducted to verify the absence of diffusion. Polymorphic composition is affected by TTIP mole fraction. At a fixed deposition temperature, low mole fractions favour rutile while high mole fractions favour anatase. The thin under-layers correspond to rutile while the long and pointed crystallites correspond to anatase. Therefore, thin films ($\leq$500 nm) show a high percentage of rutile while thick films show a high percentage of anatase, Figure 4.9. The polymorphic composition were calculated from XRD data and hence, for thick films showing 100% anatase the rutile could be too thin to be detected. For a given temperature, anatase has a higher growth rate than rutile. Therefore, changes in deposition temperature and TTIP mole fraction affect structure of CVD films [124].
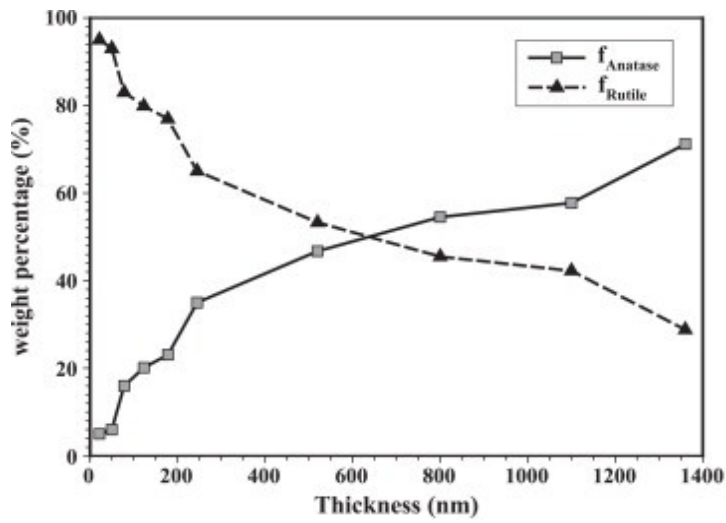
Figure 4.9: Variation of crystalline phase as a function of thickness at constant mole fraction (1.8×10^{-4}) and flow rate (6600 sccm) [124]

4.1.5   Effect on crystallite size

The experimental results of the crystallite size response are reported in Table 4.13 and the values for the effects of the process parameters, on the crystallite size response are reported in in Table 4.14. Here too, the assumed standard deviation (D_p) while analysing crystallite size using Fityk is 30%. From the values reported it could be concluded that the crystallite size is constant.

Since the effect of distance, a'$_d$ is very small (Table 4.2), it's contribution is ignored in the confounded effect of the interactions,

a'$_d$ = a$_d$

a'$_{T_c}$ = a$_{T_c}$

a'$_P$ = a$_P$

Table 4.13: Experimental results for crystallite size response

Trial run no.	d (mm)	T_c (°C)	P (Torr)	T_p (°C)	$Y_{crystallitesize}$ (nm)
1	50	350	2.5	37	32
2	70	350	2.5	42	36
3	50	600	2.5	42	32
4	70	600	2.5	37	34
5	50	350	20	42	36
6	70	350	20	37	32
7	50	600	20	37	31
8	70	600	20	42	30

Table 4.14: The effect of the parameters on crystallite size

Designation of effect a'	Effect on crystallite size a'(crystallite size)
a'_d	0.125
a'_{T_c}	-1.125
a'_P	-0.625
a'_{dT_c}	0.125
a'_{dP}	-1.375
a'_{T_cP}	-0.625
a'_{dT_cP}	0.625
a'_0	32.875

$$a'_{dT_c} = a_{PT_p}$$

$$a'_{dP} = a_{T_cT_p}$$

$$a'_{T_cP} = a_{T_cP}$$

$$a'_{dT_cP} = a_{T_p}$$

$$a'_0 = a_0$$

These terms are substituted in equation 2.13, and so, the final equation for the mass model is,

$$Y(model)_{crystallitesize} = a_0 + a_d d + a_{T_c}T_c + a_P P + a_{PT_p}PT_p + a_{T_cT_p}T_cT_p + a_{T_cP}T_cP + a_{T_p}T_p \quad (4.5)$$

Since the relative difference between the model and the experimental values is similar to that of the assumed deviation for the thickness response (30%), this model is validated.

Figure 4.10 shows that the deposition temperature has an inverse relation with the

Table 4.15: Validation for crystallite size response

Validation run no.	d (mm)	T_c (°C)	P (Torr)	T_p (°C)	Y_{expt} (nm)	Y_{model} (nm)	$Y_{difference}$ (%)
1	60	475	10	40	33.1	23	30

crystallite size. This is contrary to reports from literature, where, crystallite sizes for a cold-wall MOCVD reactor was approximately 30 nm and was reported to increase slowly with deposition temperature [124]. In hot-wall reactor, crystallite size was reported to increase with increase in deposition temperature (17 nm, 25 nm, 51 nm at 300 °C, 400 °C and 600 °C, respectively) [166]. This discrepancy is due to the almost constant crystallite size obtained in this study under the various synthesis conditions. Therefore the trends shown in this figure might have no actual physical significance.
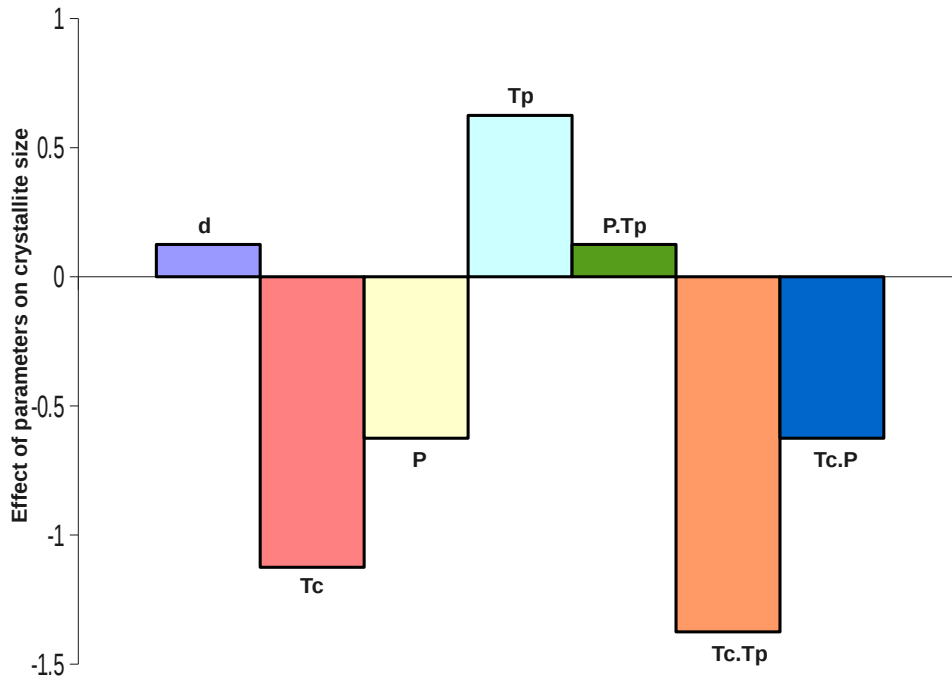
Figure 4.10: Effect of process parameters on crystallite size of coating

4.2   Conclusions

A fractional factorial DoE was successfully implemented in this study to determine the most significant parameters for any specific coating property.

The effect of the coating temperature and reactor pressure played an important role

in all three responses. The increase in coating temperature affected the packing of the coating, leading to more dense packed films. The increase in the reactor pressure inversely affected the molar fraction of the precursor leading to possibly higher surface area.

These results were obtained with a minimum number of experiments (8 experimental trial runs) and agree with data previously obtained from literature. The goal here was to show the reliability and the efficiency of DoE at the laboratory scale with promising potential at the industrial scale.

Chapter 5

TiO$_2$: Relation between Structure and Property

Contents

The previous three chapters have discussed the literature review on TiO$_2$, characterisation techniques used in this study and the different synthesis techniques used to obtain TiO$_2$ coatings. In this chapter, the focus is on the ultimate objective of this study which is to determine the relation between the structure and functional properties of TiO$_2$ coatings on metallic substrates. Here, we will discuss in detail the properties of the TiO$_2$ coatings that were analysed and their relevance to this study.

5.1 Properties of TiO$_2$ coatings

As the photocatalytic phenomenon of TiO$_2$ coatings was under scrutiny in this study, the structural properties that were chosen to be analysed were those that have been often studied by various research groups in the photocatalytic domain, namely; polymorphic composition, specific surface area, crystallite size of crystalline phase, mass, thickness, roughness, bulk density. The importance of each of them will be discussed, below.

5.1.1 Polymorphic composition

The necessity for crystallinity to conduct photocatalysis has been previously reported [1]. The aspect that was unclear was the effect of the crystalline phase. Anatase is often considered the crystalline phase with the higher photocatalytic activity, though there have been enough instances that have been reported showing a mixture of anatase and rutile with the higher photocatalytic activity, for example, commercial TiO$_2$: Degussa P-25 consisting of 80% anatase and 20% rutile. This discrepancy warranted further investigation into the effect of the polymorphs of TiO$_2$ on photocatalytic activity.

The polymorphic composition of the TiO$_2$ coatings synthesized by, both, the sol-gel and CVD techniques, were determined using the Seifert X-ray diffractometer (Section 2.2.3.2). They were all performed in the grazing incident mode configuration (X-rays incident on the coatings at 3°).

Due to the presence of a strong preferential orientation in the CVD coating patterns, it was impossible to evaluate the polymorphic composition by a Rietveld refinement of the XRD pattern. In an attempt to determine the rough estimate of the phase composition, an alternate procedure was applied, where the assumption is that the concentration of each polymorph is proportional to the total area of the lines belonging to this polymorph weighted by the polymorph density. Thus, for example, the fraction of anatase was

determined using equation 5.1.

$$Percentage \; of \; phase, a = \frac{\frac{S_a}{\rho_a}}{\frac{S_a}{\rho_a} + \frac{S_r}{\rho_r}} \qquad (5.1)$$

where,

S_a = sum of peak area of anatase

ρ_a = density of anatase (3.9)

ρ_r = density of rutile (4.3)

The calculations were further complicated by the presence of the peaks of steel (substrate) in the pattern. This is shown in Figure 5.1, where all the lines have been indexed. Figures 5.3 and 5.4 show the XRD patterns of the coatings synthesized by sol-gel and CVD, respectively.
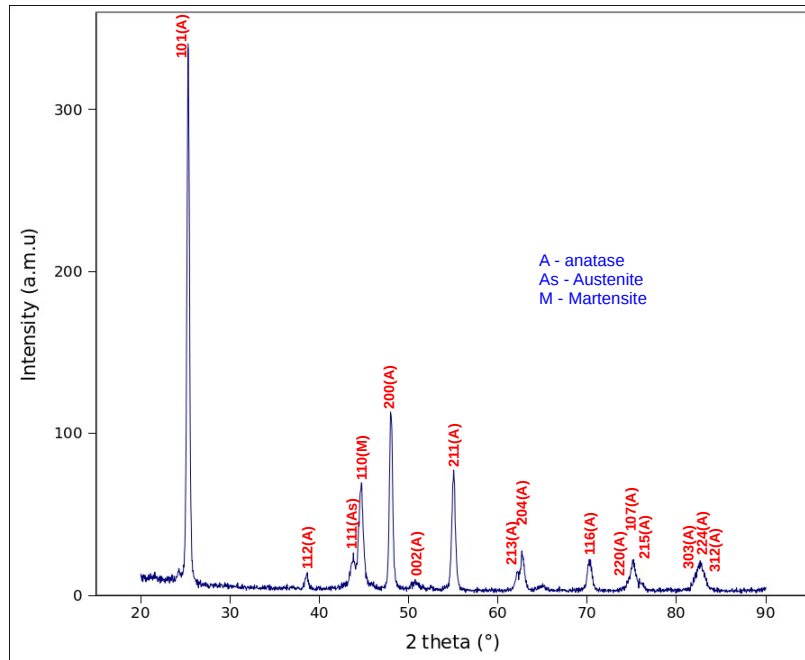
Figure 5.1: Example of an experimental XRD pattern of TiO₂ by CVD

In order to retrieve the peak parameters (intensity, area, position, FWHM) from the experimental data, a pattern decomposition method (Pawley 1980) was used. This was accomplished with the help of the Fityk software [204]. The peak positions were constrained by the cell parameters. Four crystalline phases were considered.

- Austenite, cubic, space group Fm-3m (lines 111, 002 and 022)

- Martensite, tetragonal, space group I4/mmm (lines 121)

- Anatase, tetragonal, space group I41/amd

- Rutile, tetragonal, space group P42/mnm

An example of the pattern decomposition is given in Figure 5.2 and shows that there is little difference between the calculated and experimental profiles.
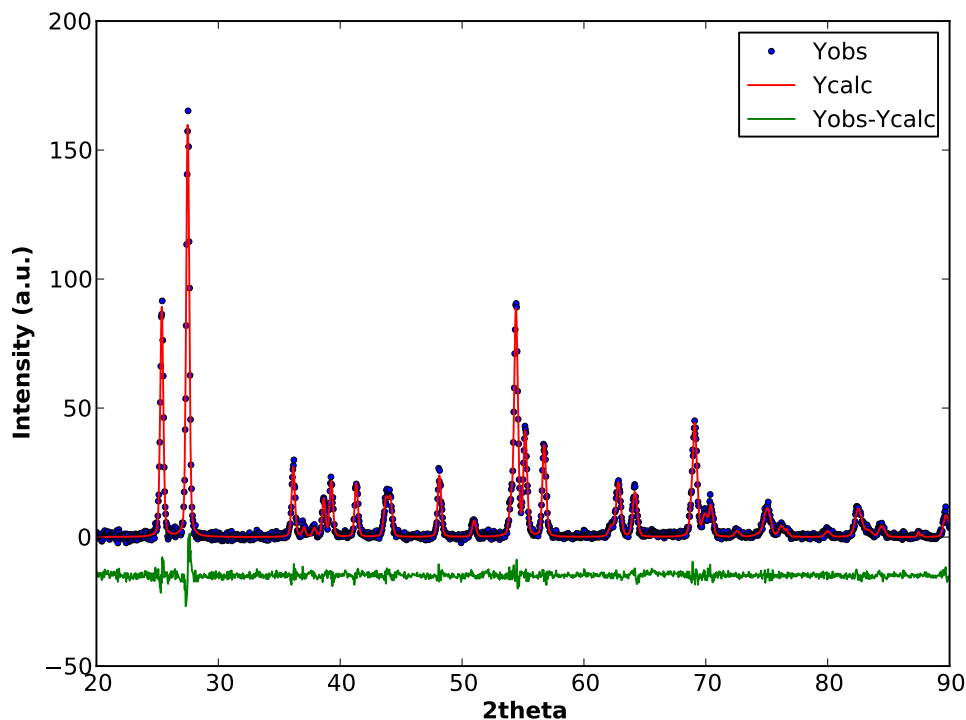
Figure 5.2: Comparison between experimental and calculated XRD patterns

The ratios of the coatings are reported as a percentage of anatase present in the coatings in Table 5.1 (sol-gel) and Table 5.2 (CVD). The abbreviations T_c and polymer in Table 5.1 refer to the heat treatment of the coating and polymer incorporated in the sol while T_c, P, T_p, d, in Table 5.2 refer to the coating temperature, the reactor pressure, precursor temperature and the distance between precursor outlet and substrate, respectively.

Table 5.1: Percentage of anatase in sol-gel coatings

Batch no.	T_c (°C)	polymer	% anatase
1	350	F127	100
2	550	F127	100
3	750	F127	31
4	750	PEG	20
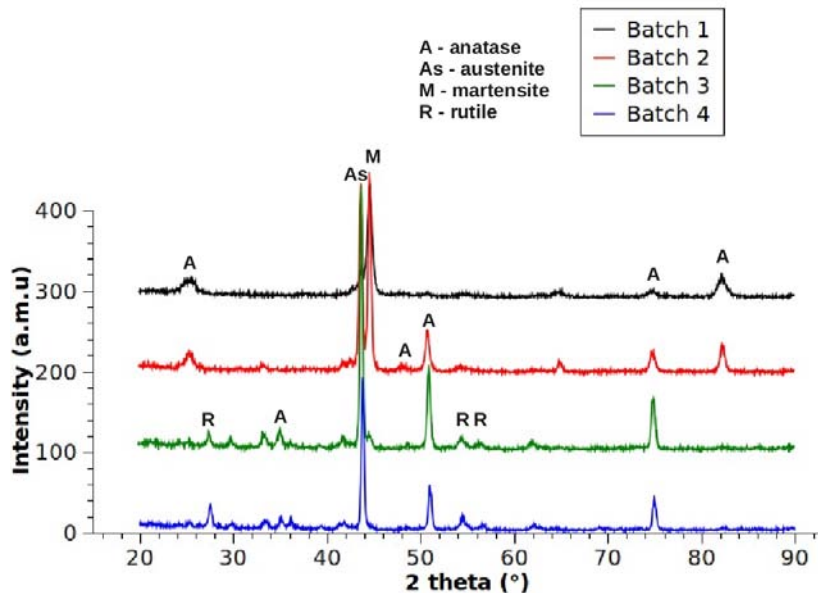
Figure 5.3: Experimental XRD patterns of TiO$_2$ by sol-gel

Table 5.2: Percentage of anatase in CVD coatings

Trial no.	T_c (°C)	P (Torr)	T_p (°C)	d (mm)	(% anatase)
1	350	2.5	37	50	100
2	350	2.5	42	70	100
3	600	2.5	42	50	87
4	600	2.5	37	70	100
5	350	20	42	50	100
6	350	20	37	70	100
7	600	20	37	50	38
8	600	20	42	70	58

The relationship between the polymorphic composition (represented as a percentage of anatase present) and the photocatalytic degradation of the methylene blue (MB) indicator, by the coatings is shown in Figure 5.5. The vertical line at 100% anatase and also the significant photocatalytic activity at lower anatase ratios show that the effect of the polymorphic composition on the photocatalytic activity is not straightforward. Based on the data represented in this Figure 5.5, the conclusion would be that a high anatase content is not a pre-requisite for high photocatalytic activity. The vertical line at 100% anatase gives the impression that other coating properties may have a significant influence on the degradation of the MB indicator, as well.
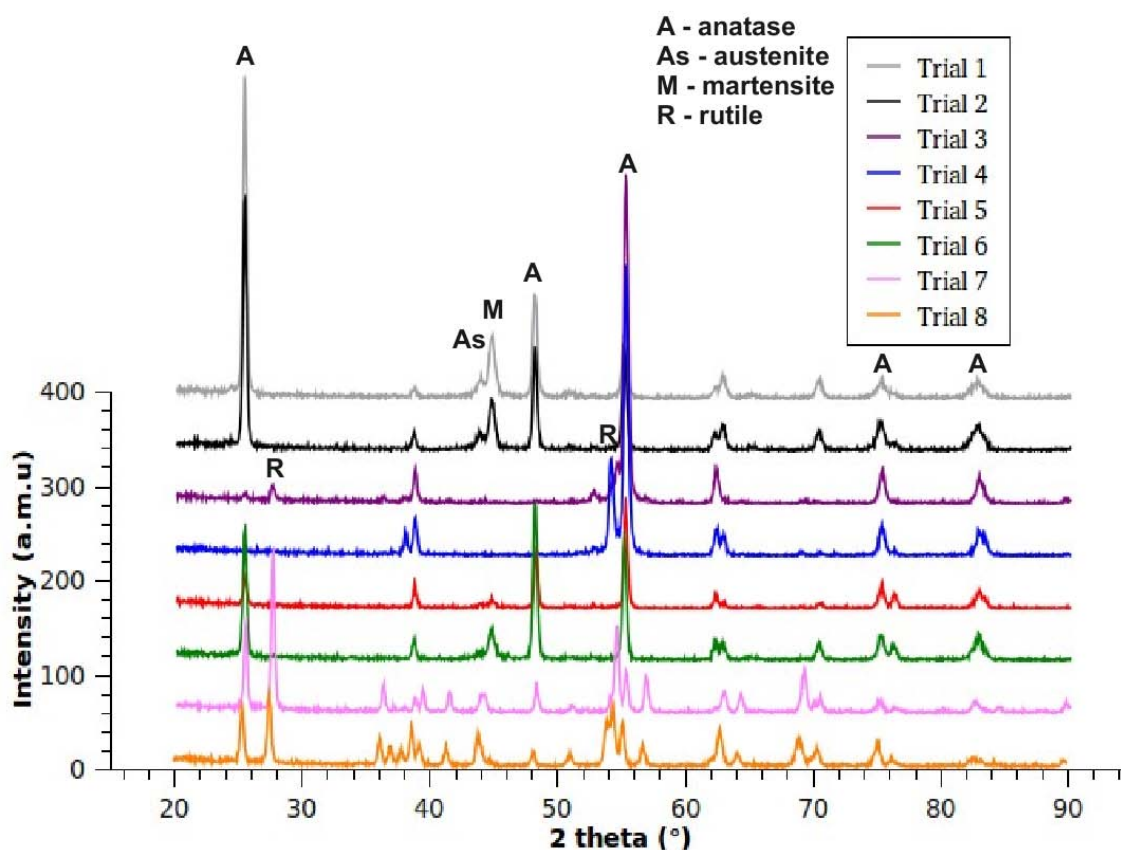
Figure 5.4: Experimental XRD patterns of TiO$_2$ by CVD
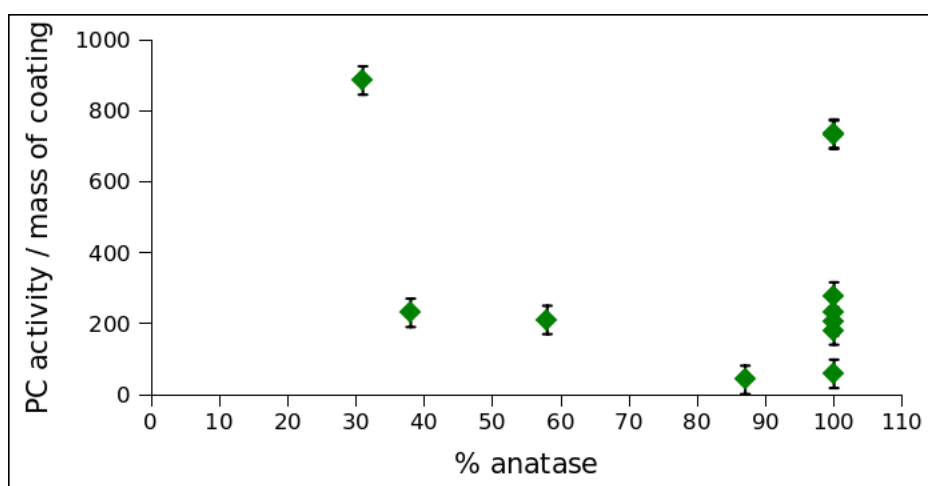
Figure 5.5: Effect of polymorphic composition on photocatalytic activity

5.1.2 Crystallite size

The strain on the MOCVD coatings, which is determined from the slope of the Williamson-Hall plot, was considered to be negligible as shown by the representative graph (of this

study), Figure 5.6.
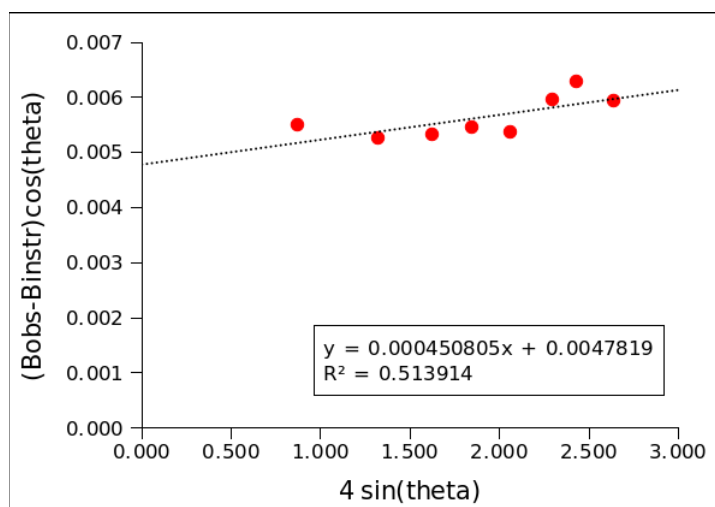
Figure 5.6: Example of a Williamson-Hall plot

A plot of the photocatalytic activity versus the crystallite size (from coatings synthesized by both CVD and sol-gel) was constructed to determine the effect of crystallite size, Figure 5.7. Here, the effect is rather clear: the increase in the crystallite size decrease the photocatalytic activity of the coating. This could be attributed to higher available surface for the MB indicator to adsorb, and consequentially, potentially more degradation to occur.
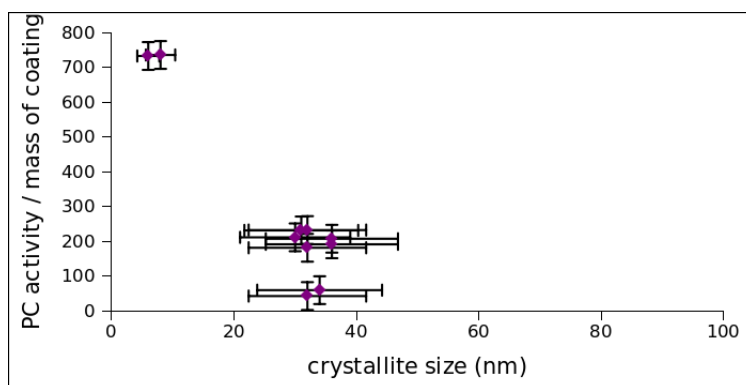
Figure 5.7: Effect of crystallite size on photocatalytic activity

The relation between the crystallite size, polymorphic composition and photocatalytic activity was also investigated, Figure 5.8. Here the PC activity was plotted against crystallite size, for all samples containing 100% anatase. This was done in an attempt to clarify the complex nature, previously discussed in Section 4.1.1, of the relation between the polymorphic composition and the photocatalytic activity. In Figure 5.8, there are two distinct families of data points: one set shows high PC activity at low crystallite size ($\leqq$ 10nm),

while the second set shows lower PC activity for bigger crystallite size ($\geqq$ 30nm). As all these points are plotted at 100% anatase, the author would conclude that the crystallite size affects the PC activity more significantly than the polymorphic compositon.
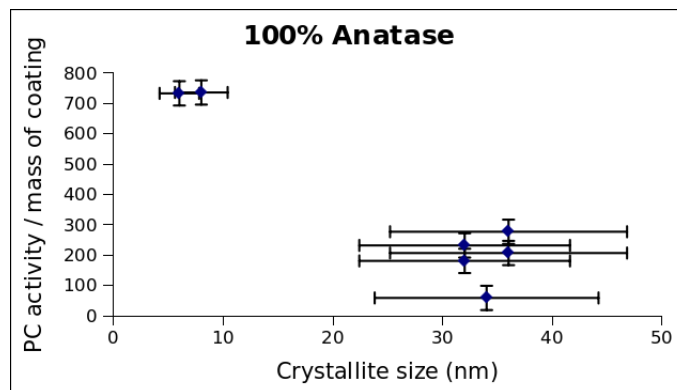
Figure 5.8: Relation between crystallite size and polymorphic composition and their effect on PC activity

5.1.3 Roughness

The root mean square roughness were determined from the AFM analyses using the Gwyddion software by scanning 10 different areas (10 μm $\times$ 10μm scans) on the sample. The effect of the roughness was investigated to determine if it had any significant influence on the PC activity of the coatings. Figures 5.9 and 5.10 show that the increase in the roughness of the coating is detrimental to its PC activity. This is explained as a result of the presence of large clusters which provide lower specific surface area when compared to smaller clusters.

5.1.4 Specific surface area, bulk density and thickness

Attempts were made to determine the specific surface area of the coating via gas adsorption isotherms with krypton as adsorbate at 77.4 K, due to the low mass involved. As the saturation pressure of krypton at this temperature is 1/300 that of nitrogen, it permits more accurate values for low surface areas. With our device (ASAP 2010 Micromeritics), it is possible to measure surface areas as low as 0.01m². A first attempt was conducted using only one coated substrate, which was unsuccessful. Nevertheless, this same technique was attempted again, this time, with four substrates, but again no reliable value could be retrieved leading to the conclusion that there was still insufficient amount of material.

These failed attempts lead us to the conclusion that the specific surface area is lower than 10m²/g. To obtain reliable results using this technique would have involved the
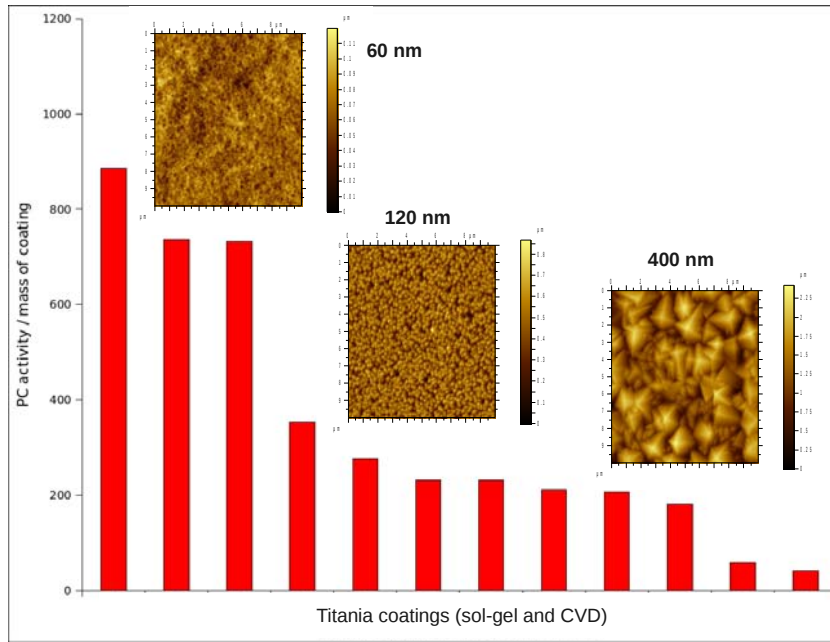
Figure 5.9: Effect of roughness on photocatalytic activity (a)
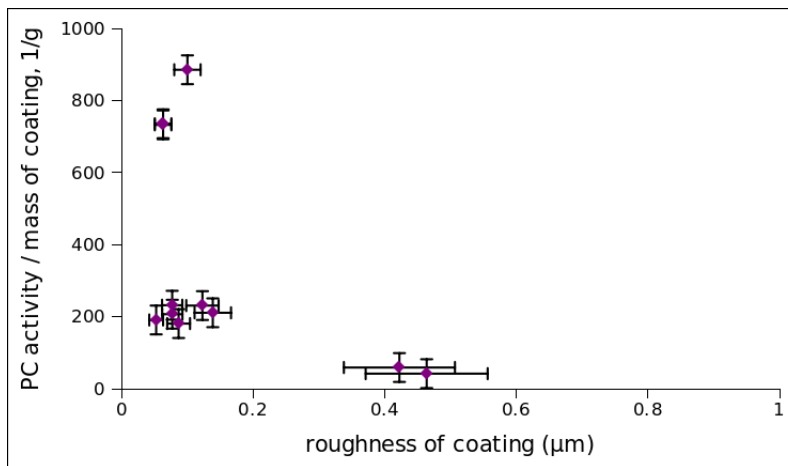
Figure 5.10: Effect of roughness on photocatalytic activity (b)

synthesis of many coatings, and so, in the interest of time this technique was abandoned and the bulk density of the coatings was measured, to give a rough approximation of the porosity present in the coatings. We also tried to estimate the surface area from AFM images, but as the tip of the AFM probe was too large, it could not reach into the space between the pores, hence this technique was rejected.

The bulk density of MOCVD coatings was calculated by dividing the mass of the coatings by their respective thickness, equation 5.2, here, the sample area is constant (1 cm²). As the thickness of the sol-gel samples was very low and difficult to measure, the bulk density for sol-gel coatings was calculated assuming a density of 4 and porosity of

30%. The thickness of the CVD coatings were measured by taking SEM images of the cross-sections of the samples (coatings on Si substrates). The average of three measures, taken on the cross-section,was used as the final thickness of the sample. In the case of the sol-gel coating the thickness was calculated from the mass measured and bulk density. We assume that the coating with the highest bulk density is the least porous and this is confirmed by the SEM cross-sections in Figure 5.11. The graph shows that as the bulk density increases the photocatalytic (PC) activity decreases (Zone II). This could be a result of the availability of less surface area for adsorption of the target molecule. On the other hand, for low bulk densities the PC activity is low (Zone I). These low bulk densities correspond to coatings with porous morphology and the low PC activity could be due to the height of the columns for the CVD coatings, and hence, perhaps the incoming radiation cannot penetrate into the coating. There appears to be an optimum thickness for these columns at which the PC activity is highest. The sol-gel coatings are present in Zone I and do not have a high PC activity since the mass deposited has not yet reached the optimal mass (optimum mass discussed in next section).

$$Bulk\ density = \frac{mass\ of\ coating}{thickness \times sample\ area\ (constant = 1cm^2)} \qquad (5.2)$$

5.1.5   Mass of coating

The mass of the coating was determined, for all samples, by weighing each sample three times and then taking their average. For sol-gel coatings, as both sides of the substrate were coated, the value of the resultant mass obtained was divided in half. From, Figure 5.12, the increase in the mass of the coating globally increases the photocatalytic activity, but appears to reach a plateau, due to the decrease in porosity. While this decrease in PC activity is straightforward for compact films (low porosity), for porous films, the effect on PC activity is a little more complex. For porous films with large mass, there is a decrease in PC activity above an optimum, since at very high mass, the pores in the films could be blocked or in the case of films with columnar morphology the height of these columns might be so large that the radiation for effective PC activity may not be accessible throughout the entire length of the columns. This is quite evident in Figure 5.11 in the previous section. This optimum mass was concluded to be attained (as in the case of the majority of the coatings besides those by sol-gel, in this study) which is shown by the negligible change in PC activity for different masses synthesised under similar conditions, Table 5.3. Therefore, it would seem judicious in analysing the PC activity alone without dividing it by the mass. This has been employed in the PCA analyses in the next section.
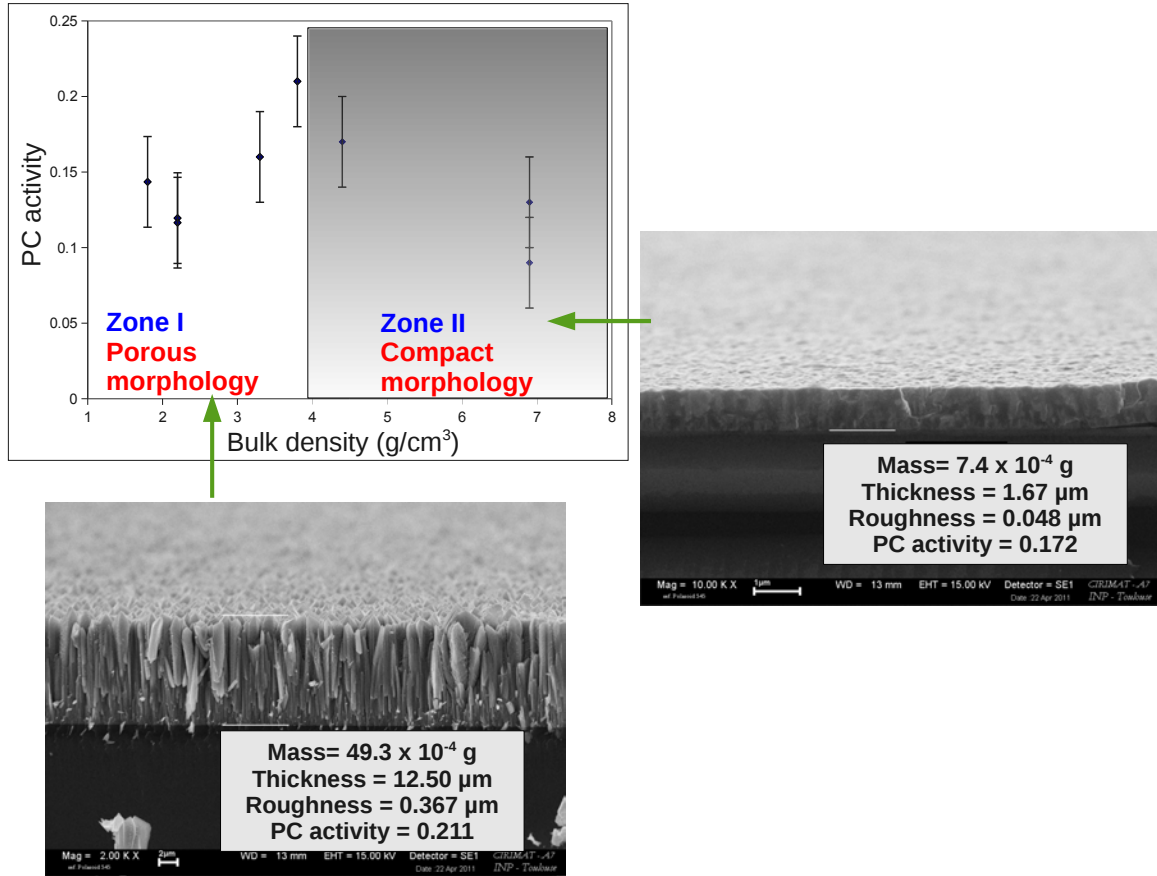
Figure 5.11: Effect of bulk density on photocatalytic activity
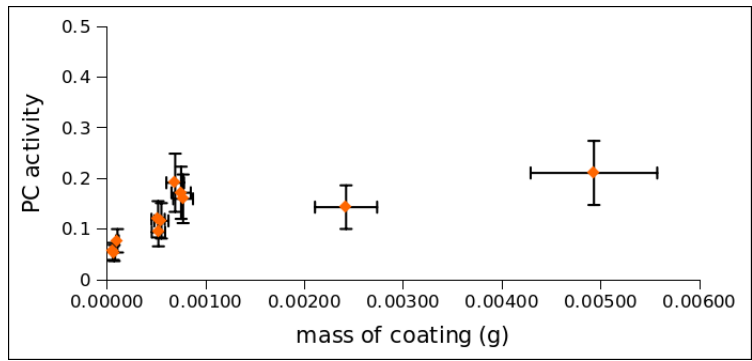
Figure 5.12: Effect of mass on photocatalytic activity

5.2   PCA analysis of TiO$_2$ coating properties

The Principal Components Analysis (PCA) as discussed in Chapter 2, is a statistical tool used to find patterns in data. In Section 4.1, the different properties of TiO$_2$ coatings were treated as a function of photocatalytic activity (PC activity). The disadvantage of this method was that each property was treated individually, when in reality, the effect of a

Table 5.3: Comparison of PC activity for different mass - CVD (* Trial 1 in CVD experimental set-up)

Run	Duration of coating (hours)	Thickness (nm)	Mass (10^{-4}g)	PC activity (%)
1*	3	760	5.2	9
2	1	300	1.2	6

property is often times affected by another.

In this study, TiO$_2$ coatings were synthesized having a large range in structural properties. Therefore, the analysis of the properties of coatings by each technique is reported, followed by the global analysis of the properties. The software used to determine patterns, in this study, was Matlab 7.7.

5.2.1 PCA analysis of TiO$_2$ coating properties - CVD

The effect of the following properties on PC activity (D) were analysed using PCA; polymorphic composition (P), roughness (R), thickness (T), mass (M). The raw data for the PCA analysis is reported in Tables 5.4.

Table 5.4: Raw data for PCA analysis - CVD

Score	R (μm)	D	P (%)	T (μm)	M (10^{-4}g)	Operating conditions (°C / Torr / °C / mm)
1	0.0462	0.0943	100	0.759	5.2	350 / 2.5 / 37 / 50
2	0.0314	0.1322	100	1.001	6.9	350 / 2.5 / 42 / 70
3	0.3675	0.2111	87	12.910	49.3	600 / 2.5 / 42 / 50
4	0.3924	0.1435	100	13.157	24.2	600 / 2.5 / 37 / 70
5	0.0726	0.16	100	2.333	7.7	350 / 20 / 42 / 50
6	0.0481	0.1719	100	1.671	7.4	350 / 20 / 37 / 70
7	0.1143	0.1195	38	2.306	5.17	600 / 20 / 37 / 50
8	0.1308	0.1165	58	2.482	5.5	600 / 20 / 42 / 70
9	0.1810	0.3061	75	3.104	26.6	600 / 20 / 37 / 50
10	0.3370	0.2493	60	4.157	10.5	600 / 20 / 37 / 50
11	0.2993	0.1456	60	3.420	9.1	600 / 20 / 37 / 50

The PC activity (D) was treated as raw data, in this analysis, instead of being divided by the mass. From Figure 5.13, we see that by plotting a graph with the first three principal components, we lose only 7% of the entire information (sum of the 3rd, 4th and 5th components over the total sum of all the principal components).
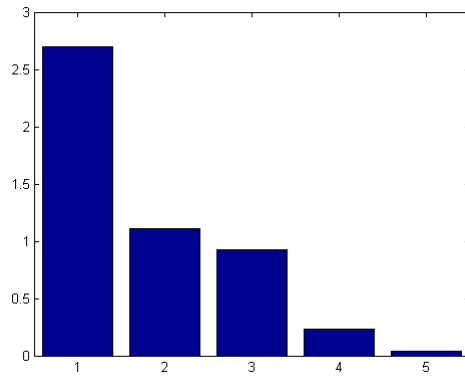
Figure 5.13: Principal components of CVD analysis
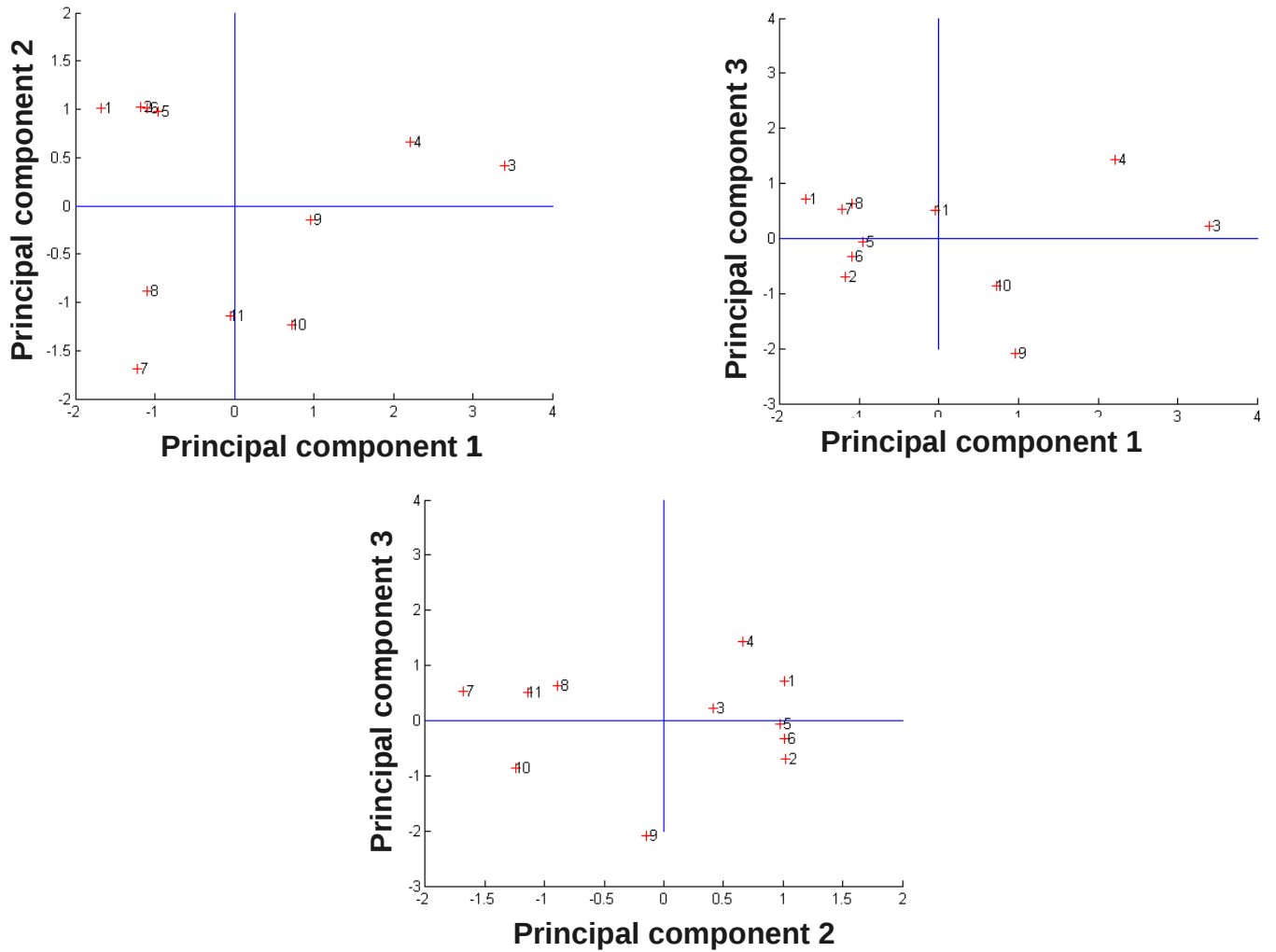
Figure 5.14: Score plot of CVD coating properties

The different views of the score plot (Figure 5.14), may be interpreted in the following manner.

1. Points 1,2,6,5 were considered as one family. These points correspond to CVD coatings synthesized at 350 °C and 2.5 Torr (1,2) and 20 Torr (5,6). The presence of these points together (despite difference in coating synthesis pressure) shows that the pressure under which the coatings were synthesized had little effect on the overall behaviour of the coating compared to the effect of the deposition temperature (discussed next).

2. The above conclusion is further emphasized by the family of points 3,4 (CVD coatings, synthesized at 600 °C and 2.5 Torr). Though the coatings were synthesized under the same pressure as point (1,2) they appear apart, most likely due to difference in deposition temperature. This interpretation confirms the conclusion from DoE (Chapter 4) that the deposition temperature was a highly influential factor in CVD coating properties as well as the strong interaction between pressure and deposition temperature.

3. Also the points 9, 10, 11 which were performed under similar conditions as 7 are not clustered together, and this is attributed to the change in the batch of the precursor, prior to the synthesis of 9, 10, 11, thereby, showing the sensitivity of the coating to changes in the precursor.

A 3-D plot of the different properties of the coating was then plotted, Figure 5.15. The different views, Figure 5.16, of this plot on a 2-D plot was analysed, as these were easier to interpret.

First, we discuss the properties that are correlated with each other. The analysis of the three different views led to the following possible interpretations, In the case of the CVD coatings, crystallite size was not included since all the coatings had similar crystallite size and, therefore, it could be considered as a constant.

1. From Figure 5.16(c), we can clearly see that the principal component axis 2 and 3 are attributed to the polymorphic composition and degradation, respectively. Hence, for CVD these two properties would be considered unrelated.

2. The principal axis 1 may be attributed to the mass, this could be confirmed if more coatings with the optimum mass for degradation were analysed. Once this mass is achieved any further increase in mass has little effect on degradation and hence, the degradation is independent of the mass.
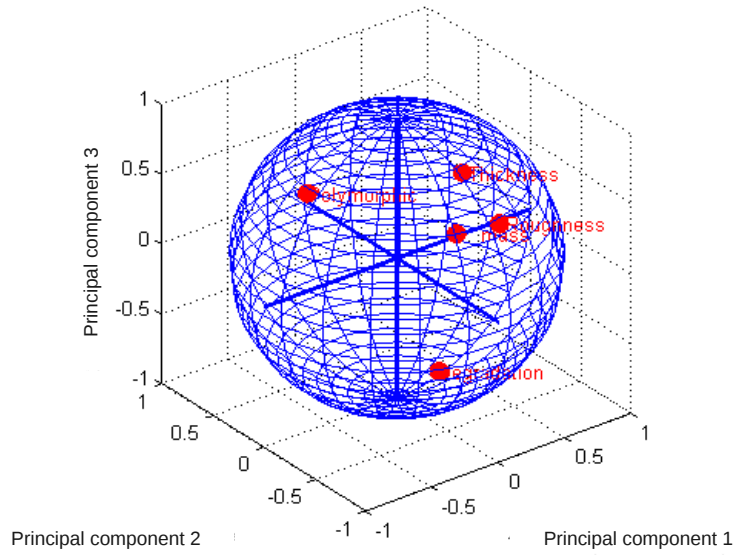
Figure 5.15: 3-D plot of CVD principal components

P - polymorphic composition
M - mass
T - thickness
R - roughness
D - methylene blue degradation
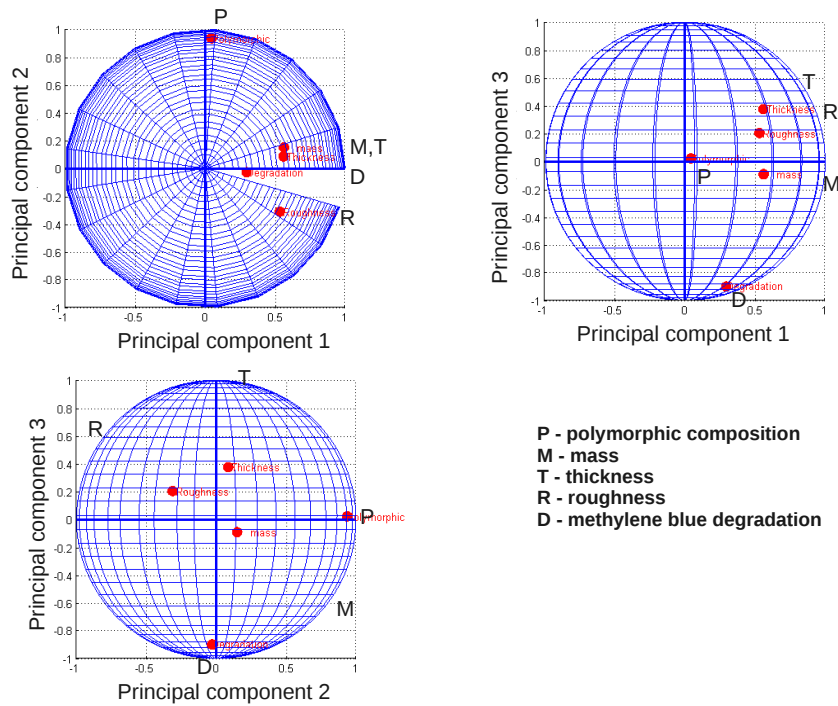
Figure 5.16: Plot of MOCVD principal components along (a) PC1 vs PC2, (b) PC1 vs PC3 and (c) PC2 vs PC3

3. Mass and roughness are not directly related due to the influence of different growth rate on the coatings (similar mass, different roughness, and vice-versa), Figure 5.17.
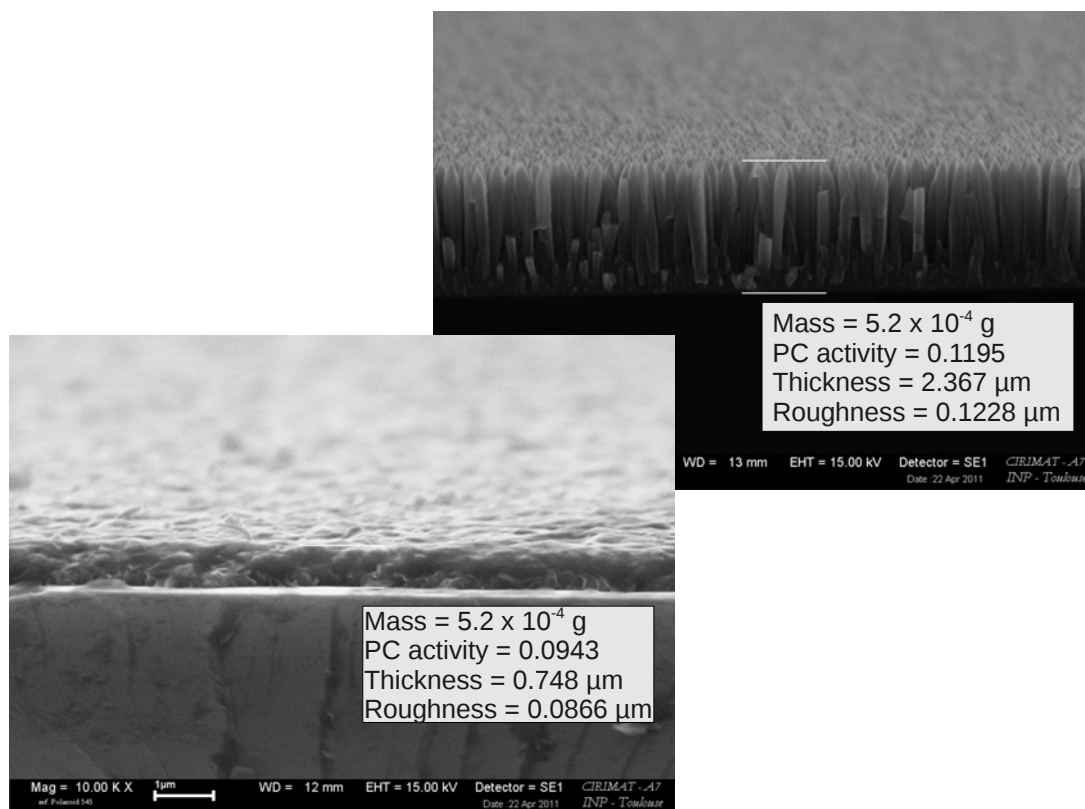
Figure 5.17: SEM micrographs of two MOCVD coatings with similar mass, but, different thickness and roughness

4. The relation between mass and thickness is not clear since the porosity of the coatings were not taken into consideration. This is clearly seen in Figure 5.17 where the SEM images show coatings produced by MOCVD with similar mass but different thickness. This similarity in mass could be attributed to the difference in porosity.

5. Degradation (D) is also not strongly dependant on the roughness (R). The roughness of a coating may be considered as an indicator of more surface available for adsorption, and hence, a weak relation between degradation and roughness could either be interpreted as degradation having a weak relation with surface area or, most likely, in this case, the roughness values not being a clear indicator of the surface area. In this study, the value of roughness (S_q) were obtained from AFM images and since the resolution of the roughness was limited by the thickness and length of the tip, the roughness values are not a clear indicator of the surface area and porosity.

5.2.2 PCA analysis of TiO$_2$ coating properties - Global (sol-gel and CVD coatings)

The effect of the following properties on PC activity of all coatings (sol-gel and CVD) were analysed using PCA; crystallite size, polymorphic composition (P), roughness (R), crystallite size (C), thickness (T), mass (M). The raw data for the PCA analysis is reported in Table 5.5. Figure 5.18 is a plot of the principal components and here when plotting a graph with the first three principal components we lose only 13% of the entire information (sum of the 4th,5th and 6th components over the total sum of all the principal components).

Table 5.5: Raw data for PCA analysis: Global (*sol-gel)

Score	R (μm)	D	P (%)	T (μm)	M (10^{-4}g)	C (nm)	Operating conditions (°C / Torr / °C / mm)
1	0.0462	0.0943	100	0.759	5.2	32	350 / 2.5 / 37 / 50
2	0.0314	0.1322	100	1.001	6.9	36	350 / 2.5 / 42 / 70
3	0.3675	0.2111	87	12.910	49.3	32	600 / 2.5 / 42 / 50
4	0.3924	0.1435	100	13.157	24.2	34	600 / 2.5 / 37 / 70
5	0.0726	0.16	100	2.333	7.7	36	350 / 20 / 42 / 50
6	0.0481	0.1719	100	1.671	7.4	32	350 / 20 / 37 / 70
7	0.1143	0.1195	38	2.306	5.17	31	600 / 20 / 37 / 50
8	0.1308	0.1165	58	2.482	5.5	30	600 / 20 / 42 / 70
9	0.1810	0.3061	75	3.104	26.6	26	600 / 20 / 37 / 50
10	0.3370	0.2493	60	4.157	10.5	28	600 / 20 / 37 / 50
11	0.2993	0.1456	60	3.420	9.1	28	600 / 20 / 37 / 50
Score*	R	D	P	T	M	C	Operating conditions (°C, polymer)
12	0.064	0.077	100	0.09	1	6	350 / F127
13	0.063	0.0536	20	0.14	1.5	11	750 / PEG
14	0.063	0.0528	100	0.06	0.7	8	550 / F127

The different views of the score plot (Figure 5.19), may be interpreted in the following manner. The points 12,13,14 are apart from the other points and correspond to sol-gel samples.For sol-gel, the interpretations made are tentative, as the number of data points analysed were insufficient for a PCA analysis. It would appear that the effect of the nature of the polymer is rather important as shown by the cluster of points 12, 14 (Pluronic-F127) which is apart from point 13 (PEG). These points correspond to sol-gel coatings synthesized at 350 °C, 550 °C, 750 °C, respectively and therefore, it would appear that the calcination temperature is of lesser importance than the nature of the polymer.

The other points correspond to CVD coatings and their interpretation remains the same
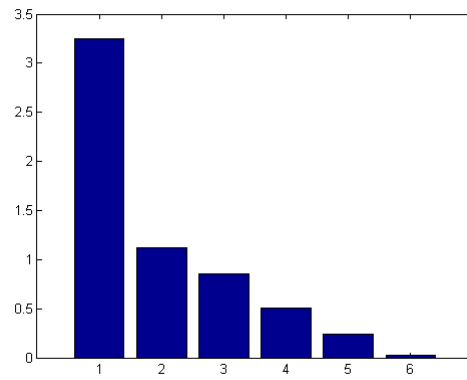
Figure 5.18: Principal components of global analysis
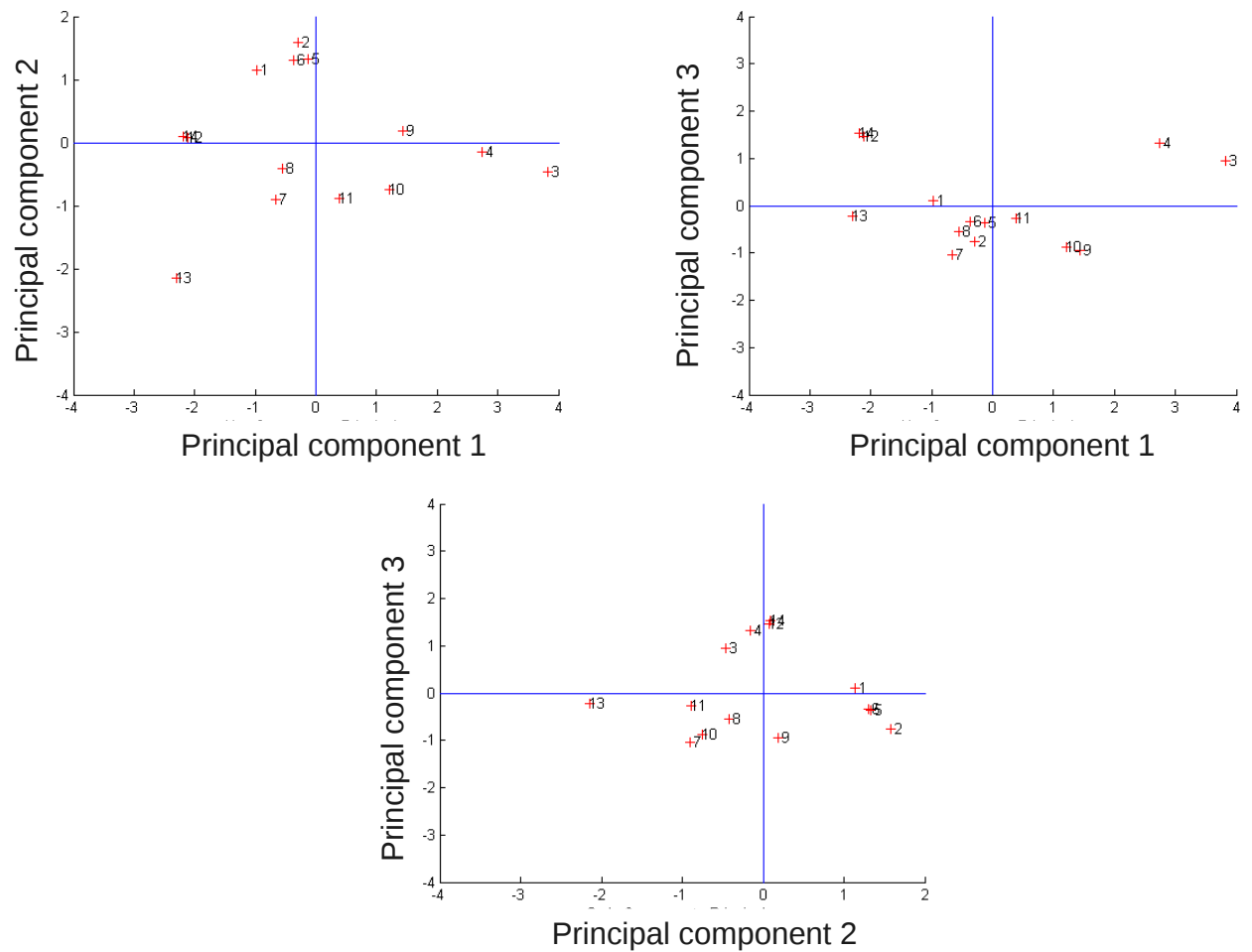
Figure 5.19: Plot of global scores along XY, XZ and YZ axis

as before (Section 4.2.1).
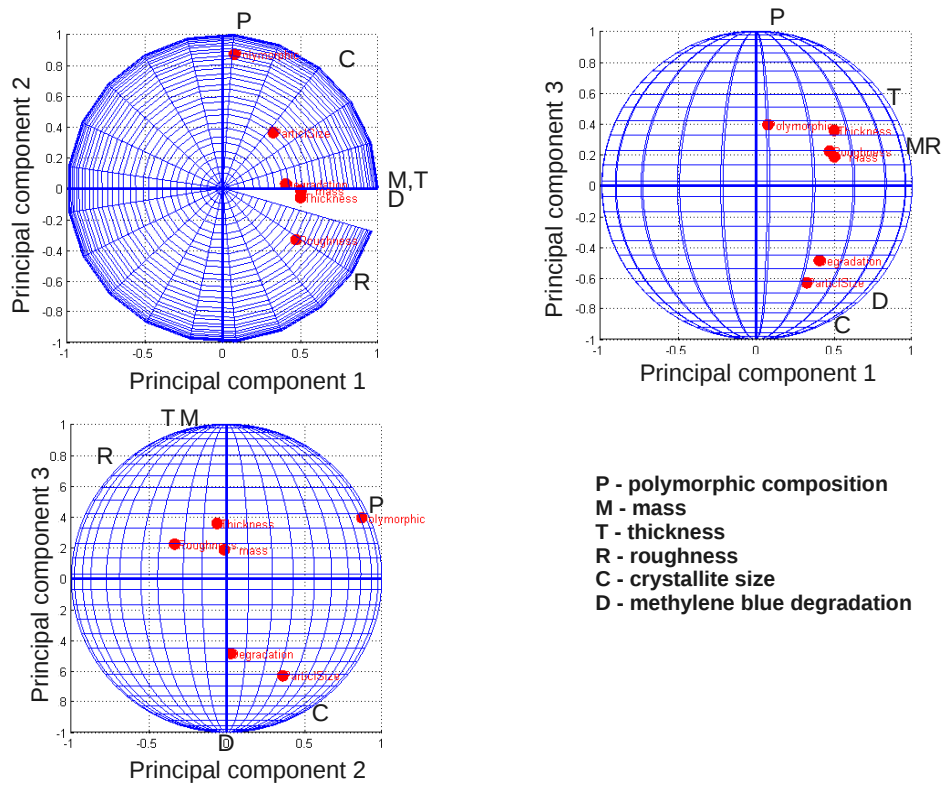
Figure 5.20: Plot of coating properties (global) along XY, XZ and YZ axis

Here as well we use the 2-D projections as a means to interpret the relation between the different properties.

1. mass (M), thickness (T) and roughness (R) were directly related - this is probably a result of the different types of morphologies (Figure 5.21) studied in this PCA analysis, such as, thin, porous, low roughness (sol-gel), thick, compact, higher roughness (CVD at low temperature and low molar fraction) and thick with columnar morphology, highest roughness (CVD at high temperature and high molar fraction). It could also be linked to the growth rate, a higher growth rate leads to a higher roughness because the grains have not had time to arrange themselves. Therefore, this strong direct correlation between mass, roughness and thickness is considered normal.

2. crystallite size (C) and degradation (D) were directly related - this can be explained by first reminding the reader that the crystallite size is not to be confused with the grain size of the coatings. The crystallite size, as mentioned earlier, was calculated using the XRD patterns. The range in our crystallite size is rather small (~10nm - ~30 nm) and, therefore, this interpretation probably has very little physical signifi-

cance. The effect of grain size would, most likely, have a greater physical meaning, since crystallites, typically, agglomerate together, and hence, individual crystallites have a lower impact on the degradation than grain size. The grain size was difficult to determine, precisely and objectively, using image analysis, especially for MOCVD coatings because of the inhomogeneity in grain size. Another hypothesis for this is that smaller crystallite size, lead to a larger number of junctions when they agglomerate to form particles. These junctions in turn lead to a large number of defaults where it is possible for the charge carriers to recombine, thereby, leading to lower degradation. Hence, larger crystallites (below an optimum) with lower number of junctions may improve degradation.
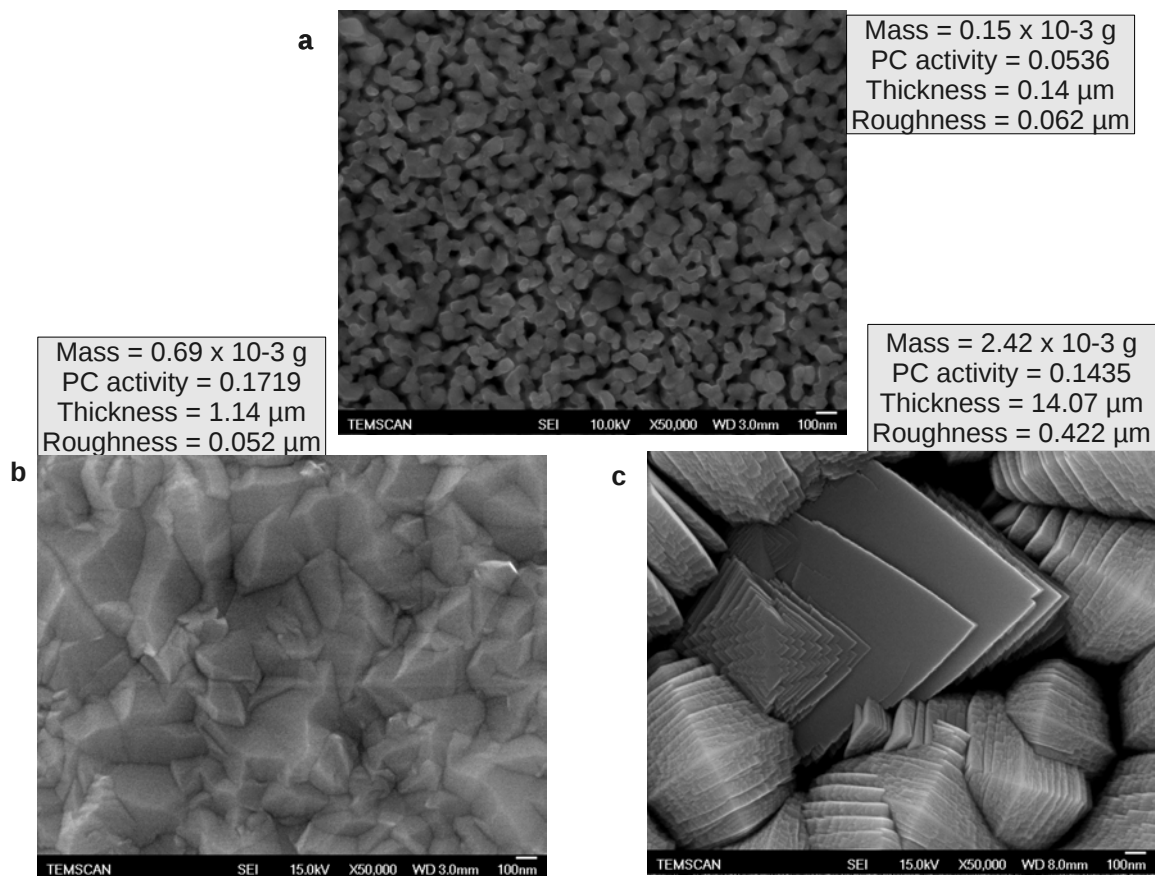
Figure 5.21: SEM micrographs of TiO₂ coatings via sol-gel (a) - low mass, high porosity and CVD (b, c) with increasing mass, thickness and roughness

Next, we discuss the properties that are not clearly correlated with each other.

1. degradation (D) was not very strongly related to the polymorphic composition (P), which contradicts empirical evidence that report that degradation is strongly (directly) related to the percentage of anatase present. This discrepancy could be at-

tributed to the different porosities that are inevitable when working with the wide temperature range between 350 °C - 750 °C. This conclusion confirms the importance of looking at the different properties of the coating, as a whole, as we have done in the PCA analysis. As neither the specific surface area data nor the porosity were included as parameters in the PCA analysis, the conclusion of the effect of porosity and specific surface area remains a hypothesis.

2. degradation (D) is also not strongly dependant on the roughness (R). A hypothesis is that though an increase in roughness may indicate higher surface area (larger degradation) it could also indicate a higher number of defects (increase in charge recombination), this competition between the two effects might lead to the unclear relation between degradation and roughness.

5.3   Synopsis

In conclusion, the relation between the different properties of TiO₂ coatings and their effect on the photocatalytic degradation (PC) of methylene blue, were studied. The effect of the different properties on PC were first studied individually. This did not permit a comprehensive analysis as the properties are related to one another, a change in one affects the other, leading to a change in the PC of the coating. Therefore, a mathematical tool called the Principal component analysis was utilized. This allowed a global view of the relation between the properties as well the relation between the properties and PC.

A global analysis of the properties of the TiO₂ coatings, synthesized by both sol-gel and CVD was conducted. It showed that the mass, thickness and roughness of the coatings were directly related, owing to wide range in morphologies investigated. The crystallite size that was used in this analysis was considered to have little physical significance, as in reality, it is the agglomerates of these crystallites that would have a higher impact on PC. It is clear that polymorphic composition did not have a high impact on PC, again, this could be attributed to the wide range of morphologies , leading to different porosities and specific surface area. As the porosity and specific surface area values of the coatings were difficult to determine, this hypothesis remains to be verified.

A PCA analysis of the MOCVD coating properties was performed as well to see the difference (if any) due to the procedure of synthesis. The results did not appear to be significantly different from the global analysis, with the small exception that here the mass thickness and roughness, were not strongly related. This could be attributed to the effect of the growth rate on the coatings. The degradation and mass are not correlated over an optimum mass; an increase over the optimum mass will have no effect on the degradation

since this excess mass will not be able to participate in the degradation (lower porosity). It is clear that the porosity and specific surface area have a strong influence on the degradation

The analysis of sol-gel coating properties by PCA was not conducted due to insufficient data. This is due to the fact that the data from the sol-gel coatings by tape-casting had to be discarded on account of their poor adherence. Due to this poor adherence the samples from tape-casting could no longer be considered as coatings, rather they were considered as powders. Hence, in the limited time available, dip-coating was used as an alternate means to obtain coatings by sol-gel. This, consequentially, did not allow sufficient quantity of time to prepare a large number of samples.

The difficulties faced during the PCA analysis stems from the lack of numerous data points due to (a) insufficient time to prepare more sol-gel samples and (b) due to the wide range of morphologies being studied it was difficult to find a common technique that could measure all these morphologies, hence, leading to the difficulty in adding porosity and specific surface area into the analysis. Some preliminary tests have been conducted and show that cyclic voltammetry could be used to evaluate the surface area with just one coated substrate [205].

Conclusion and Future work

The overall objectives of this study was to find an environmentally-friendly and simple procedure to synthesize titanium-dioxide, as well as, to determine the relation between the structural and functional properties of titanium dioxide coatings. Both of these objective have been attained in this study.

By the sol-gel technique, titanium dioxide sols were synthesized by the hydrolysis of titanium(IV)isopropoxide. Nanocrystallite dispersions of TiO_2 in water were prepared that were suitable for coatings and having long-term stability (more than 1 year) in terms of polymorphic composition, crystallite and agglomerate size. To obtain this the optimum experimental conditions were found to be:

1. $H_2O/Ti = 0$ –100

2. $H^+/Ti \sim 0.2$, HNO_3 preferred to HCl

3. peptization temperature allowing the fast removal of isopropanol by evaporation ($\sim$ 80°C).

In these conditions, the sols were composed of aggregates with a chainlike structure of anatase ($\sim$90%) and brookite crystallites (5–6 nm). On ageing, a progressive reorganization of the aggregates towards a more compact packing occurred. This rearrangement was accompanied by a marked decrease in the viscosity. These aggregates could be quickly broken by ultrasonication. Stable sols composed solely of anatase crystallites (4 nm) were prepared by partially complexing the TTIP by acetylacetone, before hydrolysis. It was not possible to produce porous films from these sols, stabilized by electrostatic repulsion. This is because during the drying step the particles rearrange themselves to form a close packed structure. However, coatings with controlled porosity could be prepared from these hydrosols through the addition of polymers, like PEG or block copolymers (Pluronic F-127).

A design of experience (DoE) was utilised, to our knowledge, for the first time in MOCVD for the synthesis of TiO_2 coatings. It was employed to determine, in a timely and economical manner, the most significant process parameters for any quantifiable property of the coating and to highlight the interaction between these operating parameters, as well

as, the correlation between the structure of the coating and the process. The conclusions drawn from the DoE were compared to results obtained by previous studies and were found to concur. Therefore, the DoE was successful in screening the most important process parameters, with a minimum number of experimental trials. For most of the properties that were under investigation, the DoE showed that, the deposition temperature and reactor pressure were, often-times, the most significant. Therefore, to change the microstructure and composition of MOCVD coatings, changing these process parameters will ensure the highest impact. It has to be stressed that the conclusions drawn from the DoE are restricted to the experimental range that was under investigation.

Principal Component Analysis (PCA) was conducted to have an overall view of how the different properties of the coatings related with one another. The interpretations made from this analysis were that the photocatalytic (PC) activity of the coatings produced did not relate strongly to the polymorphic composition, which is contrary to literature review and is explained to be a result of the different morphologies that lead to different porosities and specific surface area. The PC activity did not depend on the mass over a critical mass. With this analysis it appeared to be clear that the porosity and specific surface area played a larger role than polymorphic composition; this hypothesis has to be verified because we did not succeed in determining the specific surface area of our coatings during this study. However, some preliminary tests have been conducted showing that cyclic voltammetric could be used to evaluate the surface area of our films.

The future work regarding this particular study would involve synthesizing and analysing more coatings, especially by sol-gel. The dip-coating process could then be optimised, for this sol, by varying the viscosity of the sol, the withdrawal rate of the substrate from the sol, etc. . The estimation of the surface area using voltametry, if successful, will go a long way in determining if the hypothesis concerning the surface area is valid or not. The effect of the change in the precursor on the coatings will be analysed separately to determine the conditions for reproducibility. The results obtained here may be of potential use for different applications, such as in solar cells and catalysis.

Appendix I

The coatings produced by tape-casting had very poor adhesion, as shown in the figure below, and hence, all data obtained from these coatings had to be rejected as they could no longer be considered as coatings, rather they could be considered as a powder. As these coatings had a thickness of $\sim 2~\mu$m, it was then decided to synthesize coatings (sol-gel) that had a lower thickness to prevent poor adhesion in the coatings produced by dip-coating. Hence, coatings had been synthesized by dip-coating at the lowest withdrawal rate, as this allowed to reduce the thickness of the coating.
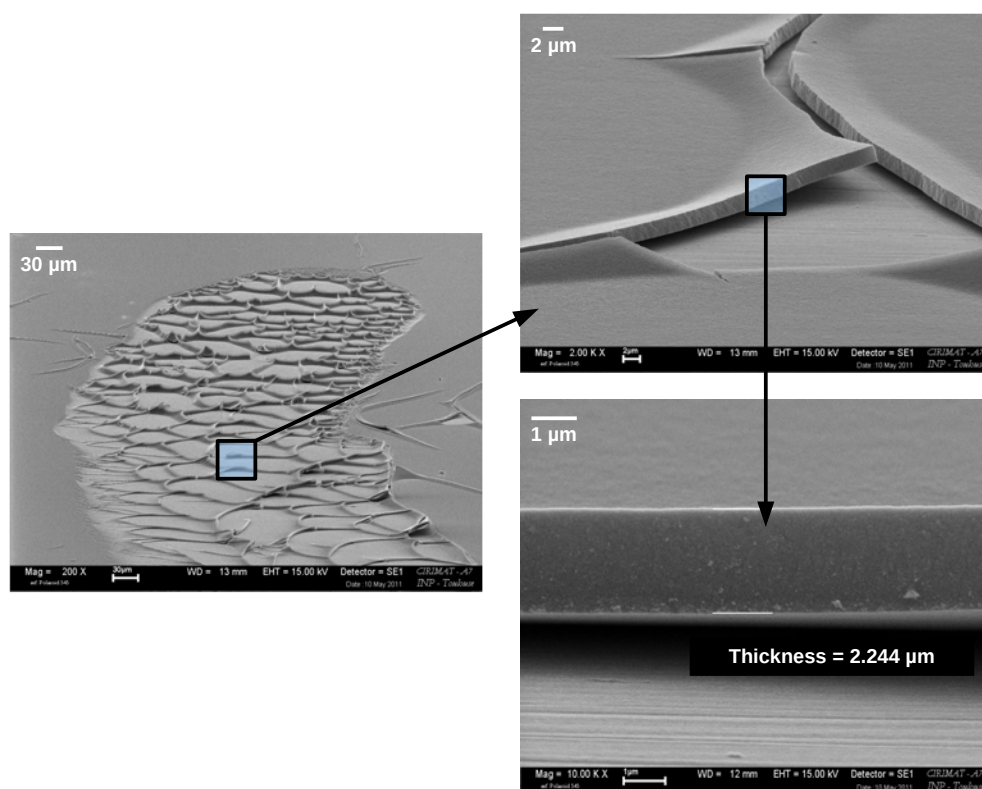
Appendix II

The reproducibility trials for MOCVD-TiO$_2$ was severely hindered by the change in the precursor batch. This can be seen quite clearly in the figure below. Images (a) and (b) correspond coatings produced with a new precursor batch while (c) corresponds to a coating made with the old precursor batch. These coatings were synthesized under identical conditions. The precursor was changed in a glove-box, and hence, impurities may be ruled out as the cause for this marked difference in morphology. Empirical evidence points to an unpredictability in the coating properties of samples synthesized by a new batch of precursors until after a few runs have been performed with the same. Therefore, it would seem that the precursor takes some time before it produces reproducible results. This 'stabilisation time' of the precursor (approximately 3 experimental runs with a new precursor batch) has to be taken into account before starting a whole set of experiments. It has to be stressed that the experiments considered for the validation of the various responses of the DoE in Chapter 4 were performed with the same precursor charge, and were reproducible.

137
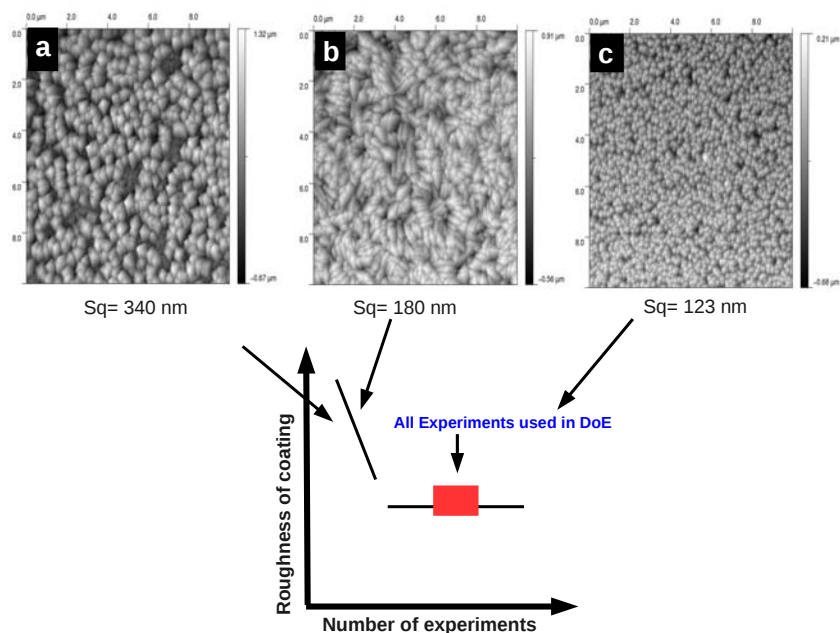
Résumé en français

La photocatalyse est un processus au cours duquel un semi-conducteur est excité par une source photonique dont l'énergie est supérieure à celle de la bande interdite. Quand les photons interagissent avec le semi-conducteur un électron passe de la bande de valence à la bande de conduction laissant un trou dans la bande de valence. Ces paires électron-trous sont alors utilisées, par exemple chimiquement, pour dégrader des polluants organiques. Dans cette étude le semi-conducteur choisi est le dioxyde de titane (TiO_2). Les recherches visent à rendre cette technologie plus efficace et plus économique, par exemple en élargissant le domaine spectral pour améliorer l'efficacité sous le rayonnement solaire ou en diminuant le cout de la synthèse afin de généraliser son utilisation à l'ensemble de la population.

Le premier objectif de cette étude était la détermination des caractéristiques du matériau qui jouent un rôle déterminant dans l'activité photocatalytique. Le second était de d'optimiser les procédures de synthèse de TiO_2.

Deux procédés de synthèse ont été utilisées dans cette étude : le procédé sol-gel et le dépôt chimique en phase vapeur (CVD). La raison de l'emploi de ces deux techniques réside dans leur capacité à produire TiO_2 sous une large gamme de morphologies mais avec des variétés polymorphiques similaires. Le précurseurs et les substrats employés pour les deux procédés ont été les mêmes, respectivement l'isopropoxyde de titane, le silicium (100) et l'acier inoxydable.

Les revêtements TiO_2 synthétisés ont été caractérises du point de vue de leur variété polymorphique, taille de cristallites, surface spécifique, rugosité, épaisseur, potentiel zêta (sol). Deux outils statistiques ont été utilisés:

1. les plans d'expériences – qui ont été employés durant la synthèse de revêtements CVD pour déterminer quantitativement les corrélations entre les paramètres de synthèse et les propriétés des revêtements.

2. l'analyse en composante principale – qui a été utilisée pour l'analyse des propriétés de l'ensemble des revêtements (sol-gel et CVD) et pour déterminer les propriétés déterminantes dans l'activité photocatalytique

Dans ce résumé nous nous focaliserons sur l'optimisation des deux techniques de synthèse et sur les corrélations obtenues entre la morphologie, la composition polymorphique et les propriétés fonctionnelles (ici l'activité photocatalytique des revêtements).

Procédé sol-gel : caractérisations des sols et des xérogels

Procédé de synthèse des sols

L'hydrolyse des alcoxydes de titane dans un grand excès d'eau, suivie d'une peptisation, est une méthode simple et rapide pour préparer des dispersions colloïdales de nanoparticules de TiO_2 dans l'eau [152, 154, 172, 173, 176, 174, 175, 184]. Dans cette étude, la procédure standard consistait à verser rapidement, sous forte agitation, une solution d'isopropoxyde de titane dans l'isopropanol ($C_3HO/Ti = 3.5$) dans une solution très diluée d'acide nitrique ($H_2O/Ti \sim 90$ et $H^+/Ti = 0.2$) chauffée à 70 °C. Le mélange est maintenu à 0 °C et sous agitation pendant 16 heures. Le précipité blanc formé initialement se transforme progressivement en une solution translucide. Pendant les 6 premières heures le flacon est laissé ouvert pour éliminer l'alcool par évaporation.

Procédé de dépôts des revêtements sol-gel

Les revêtements sol-gel ont été réalisés par la technique de trempage-retrait (dip-coating) qui consiste à plonger le substrat à recouvrir dans le sol puis à le retirer avec une vitesse contrôlée. Les principaux paramètres qui gouvernent l'épaisseur du dépôt sont la viscosité du sol, sa concentration en particules et de la vitesse de retrait.

Caractérisation des sols

Mesure de la taille des particules par diffusion de la lumière

Le diamètre hydrodynamique moyen des particules, mesuré par diffusion de la lumière (DLS) sur des sols fraichement préparés est compris entre 300 et 500 nm. Après quelques jours il devient de 100 nm environ. Quand les sols sont soumis aux ultrasons le diamètre decroit jusqu'à 20 nm.

Mesures rhéologiques

La connaissance du comportement rhéologique des sols est important car la viscosité est un paramètre clé pour contrôler l'épaisseur des revêtements réalisés par trempage-retrait (dip-coating). En outre il donne des informations sur les interactions entre les particules et sur la morphologie des agrégats. Les courbes d'écoulement ont été déterminés, avec un cône plan, en augmentant puis en diminuant la vitesse de cisaillement. Pour tous les sols les courbes enregistrées lors de la diminution du cisaillement se superposent avec les courbes enregistrées pendant l'augmentation. Les courbes expérimentales ont été modélisées par

une loi de type « puissance » ou loi d'Ostwald de Waele (equation 3.1). Quand les sols ont un comportement Newtonien (n = 1), K est en fait la viscosité. Pour γ compris entre 1 et 1000 s^{-1}, ce modèle donne un parfaite représentation des courbes expérimentales avec des coefficients de corrélation > 0.9999.

Les sols frais ont un comportement pseudo-plastique (n $\sim$ 0.75). Dans une étude précédente [198], il avait été observé que la dépendance entre la viscosité et la concentration volumique des particules pouvait être prédite par le modèle de Bachelor [200] à condition que la fraction volumique soit remplacée par la fraction volumique effective des agrégats prenant en compte leur dimension fractale. Le comportement pseudo-plastique observé avec les sols frais serait dû au fait que les particules primaires ont une forte tendance à former des agrégats en chaine (Figure 3.2). La densité d'empilement des particules diminue du centre vers la périphérie et il est probable que les particules en bordure puissent être séparées pour les fortes vitesses de cisaillement. Lors du vieillissement on constate que le comportement rhéologique se rapproche du comportement Newtonien (n $\sim$ 0.95). Le vieillissement entraine une décroissance de K; on observe une relation linéaire entre K et le logarithme de la durée de vieillissement. La diminution de K lors du vieillissement pourrait s'expliquer par une réorganisation des agrégats pour donner des structures plus compactes car la peptisation va progressivement accroître la charge de surface des particules et donc diminuer leur probabilité de collage. Les ultrasons produisent une diminution considérable de K (d'un facteur 40) et n devient proche de 1. Quel que soit l'age du sol, la valeur de K après action des ultrasons reste la même. Les paramètres K et n, pour un sol préparé sans addition d'isopropanol, sont similaires à ceux d'un sol préparé en diluant l'alcoxyde dans l'isopropanol. Par conséquent la dilution ne semble pas changer l'état d'agrégation des particules. Les sols préparés avec ajout d'acétylacétone ont un comportement newtonien et une faible viscosité. L'ajout de polymère dans le sol provoque une forte décroissance de la viscosité. Cet effet a déjà été reporté pour le PEG 2000 [198] et le Pluronic F-127 [201]. Il peut être expliqué en supposant que l'adsorption du polymère sur les particules de TiO$_2$ provoque une stabilisation par effet stérique et par conséquent une diminution de la probabilité de collage. Ceci, comme précédemment, conduit à la formation d'agrégats plus compacts. Ceci explique aussi pourquoi cet effet décroit et même disparaît complètement avec le vieillissement.

Mesure du potentiel zêta

L'effet du pH sur le potentiel zêta a été déterminé. Le point isoélectrique a été obtenu pour un pH de 5.4. Cette valeur est en bon accord avec celles de la littérature [172, 202, 172, 188, 189, 190, 191].

Observation par microscopie électronique en transmission (MET)

L'influence de la durée de peptisation sur la morphologie des particules a été suivie par microscopie électronique en transmission (Figure 3.2). L'échantillon prélevé immédiatement à la fin de l'hydrolyse (t=0) est constitué de particules de 300 nm environ. Les contours des particules sont flous ce qui est en accord avec leur structure quasi amorphe mise en évidence par diffraction des RX (Figure 3.1). Après 4 h de peptisation le sol est encore essentiellement constitué de particules de 100 à 200 nm, contenant des cristallites de 4-5 nm. A la fin de la peptisation (après 16h) le sol contient des chaines d'agrégats de cristallites de 4-6 nm. La taille du cœur de ces agrégats est comprise entre 25 et 50 nm. La taille des cristallites est en bon accord avec celle déduite de l'élargissement des pics de diffraction par la formule de Scherrer.

Diffraction des RX

L'influence de la durée de peptisation sur la structure cristalline des particules a été suivie par diffraction des RX. Les diffractogrammes reproduits Figure 3.1 ont été enregistrés sur les poudres préparés par séchage des échantillons de sols à 40 °C. L'échantillon prélevé immédiatement à la fin de l'hydrolyse (t=0) est pratiquement amorphe. Après 1h, même si les pics principaux de l'anatase peuvent être identifiés l'échantillon reste essentiellement amorphe. Après 4h l'échantillon est nanocristallin et il y a très peu de différences avec un échantillon prélevé 6 jours après la synthèse. Ces diffractogrammes correspondent à un mélange entre de l'anatase (quadratique, I41/amd, ICDDPDF 01-073-1764) et de la brookite (orthorhombique, Pbca, ICDD PDF 00-029-1360). Les diffractogrammes d'échantillons prélevés 6 jours et 6 mois après la synthèse sont superposables. Ceci prouve que la taille et la structure cristalline des nanoparticules ne sont pas modifiées par le vieillissement et montre par conséquent la grande stabilité de ces sols. Les diagrammes de diffraction réalisés à partir des sols préparés avec ajout d'acétylacétone montrent qu'ils ne contiennent que de l'anatase.

Analyse de l'effet des paramètres de synthèse sur la stabilité des sols

La première étape vise à obtenir des particules les plus petites possible en maximisant la vitesse d'hydrolyse par rapport à la vitesse de condensation. Ceci est obtenu en utilisant un large excès d'eau acidifiée car l'isopropoxyde de titane est très réactif. Il peut être rapidement et complètement hydrolysé avant que la condensation ne débute [192].

Le rapport optimal eau/alcoxyde se situe entre 50 et 100. En effet il a été montré que, pour un rapport supérieur à 200, l'effet de la dilution sur la taille des particules

devient négligeable [176] et, un rapport supérieur à 100, donne des sols stables mais trop dilués nécessitant une concentration préalable avant de pouvoir être employés pour réaliser des revêtements. D'autre part, pour des rapports inférieurs à 30 il peut subsister des groupements -OR non hydrolysés [193, 194].

Les nanoparticules formées lors de cette hydrolyse très rapide ont une énergie de surface très élevée et s'agglomèrent rapidement pour donner des grosses particules qui précipitent. Comme illustré sur la figure 3.1, ces particules sont amorphes : en effet la nucléation très rapide entraine que la croissance des particules est gouvernée par la cinétique conduisant à la formation de la phase la moins stable [195]. Mais cette phase est aussi la plus soluble et va être ensuite progressivement remplacée par des phases cristallisées comme la brookite, l'anatase ou le rutile. La vitesse de redissolution dépend du pH et de la température, paramètres qui gouvernent la solubilité.

La deuxième étape est la peptisation qui démarre immédiatement si l'hydrolyse est réalisée avec de l'eau acidifiée, ou lors de la post-addition de l'acide. Comme le PCN est proche de la neutralité, l'addition d'acide provoque la protonation des groupements hydroxyles ce qui accroît la densité de charges à la surface des particules et diminue la tension interfaciale [166, 150, 153]. Ceci provoque la fragmentation des agrégats et, comme les particules portent toutes la même charge, empêche leur reagréation car elles se repoussent. Contrairement à l'hydrolyse, la peptisation est un processus lent qui suit une cinétique d'ordre 1 [133] avec des constantes de temps de plusieurs jours [124]. Les études cinétiques ont montrées que la peptisation est un processus lent car il résulte de la compétition entre deux réaction inverses, la fragmentation due à l'agent peptisant et la réagrégration due à la une stabilisation insuffisante de la suspension [173, 184, 124].

La durée de peptisation peut être réduite soit en accroissant la température, soit la concentration en acide [195]. Cependant ceci à des conséquences néfastes. La diminution du pH et l'augmentation de la température accroit la solubilité de TiO_2 conduisant au grossissement des grosses particules aux dépends des petites selon le phénomène classique de dissolution-reprécipitation (mûrissement d'Ostwald). En outre des particules secondaires peuvent être formées par structuration verticale produite par épitaxie de particules élémentaires [152]. Un autre effet néfaste de l'augmentation de la solubilité de TiO_2 est la transformation progressive des phases cristallines métastables comme la brookite et l'anatase en rutile qui est la phase thermodynamiquement la plus stable.

Par conséquent pour préparer des sols stables il est obligatoire d'utiliser une concentration en acide la plus proche possible du minimum requis pour obtenir la peptisation. La durée de la peptisation peut-être réduite par action des ultrasons si nécessaire.

A ce stade la question se pose de savoir quel est le meilleur agent de peptisation entre HCl et HNO_3?

Isley and Penn ont montré que l'emploi d'HCl accroît le taux de phase amorphe [154]. Avec le vieillissement cette phase amorphe va recristalliser pour donner la phase stable rutile. Ceci a été mis à profit pour synthétiser des nanoparticules de rutile [110]. Par ailleurs, HNO_3 est aisément décomposé par chauffage à 300 °C alors qu'il est beaucoup plus difficile d'éliminer les ions chlorure sans un lavage exhaustif. Donc, excepté si le rutile est la phase recherchée, on aura intérêt à employer HNO_3 comme agent de peptisation.

Un autre paramètre important, souvent négligé, est la présence d'alcool. Vorkapic and Matsoukas ont montré que les alcools ont un effet néfaste sur la peptisation [184]. Ils expliquent cela par la diminution de la constante diélectrique du solvant favorisant la réagrégation. Il est aussi possible que l'alcool stabilise la phase amorphe formée aussitôt après l'hydrolyse. Par conséquent l'élimination de l'alcool diminue le temps de peptisation et stabilise le sol. Il faut remarquer que la présence de l'isopropanol ne peut être totalement évitée dans la mesure où il s'en forme lors de l'hydrolyse. La meilleure méthode pour éliminer l'isopropanol est l'évaporation en effectuant la peptisation dans un flacon ouvert et en chauffant à une température proche de l'azéotrope isopropanol-eau (80.3 °C).

L'isopropoxyde de titane est souvent dilué dans isopropanol avant de réaliser l'hydrolyse. Ceci est supposé produire une nucléation plus homogène et réduire la croissance des cristallites. Cependant nous n'avons observé que très peu de différence entre la taille des cristallites préparées avec et sans ajout d'isopropanol.

En résumé les conditions opératoires optimales, permettant de synthétiser des sols très stables de nanoparticules de taille la plus faible possible, sont les suivantes : utiliser un rapport $[H_2O]/[Ti]$ compris entre 50 et 100, HNO_3 comme agent peptisant avec un rapport $[H+]/[Ti] = 0.2$, une température d'hydrolyse comprise entre 50 et 70 °C, une température de peptisation de 80 °C et laisser l'isopropanol formé durant l'hydrolyse s'évaporer. Ces sols sont constitué de petits agrégats ($\sim$ 100 nm) de cristallites (5-6 nm) d'anatase ($\sim$ 90%) et de brookite.

Il est aussi possible de préparer des sols composés uniquement de très petites crystallites (4 nm) d'anatase par complexation partielle de l'isopropoxyde de Ti par l'acétylacétone avant l'hydrolyse. Ces complexes sont bien plus difficiles à hydrolyser que les groupes alkoxydes [192].

Caractérisation des xérogels

Détermination de la densité des xérogels par pycnométrie à l'hélium

Nous avons observé que la densité mesurée par pycnométrie à l'hélium était nettement inférieure à la densité cristalline. Ceci pourrait être du à la présence de porosité fermée mais le fait qu'on observe une bonne corrélation entre la densité mesurée et la surface

spécifique indique plutôt que ce serait du à la présence à la surface des particules d'une couche contenant de l'eau adsorbée et des groupes hydroxydes.

Détermination de la surface spécifique et de la distribution des pores

La surface spécifique et de la distribution des pores ont été déterminés à partir des isothermes d'adsorption-desorption d'azote à 77K (Figure 3.6). La surface spécifique a été calculée en utilisant la méthode BET [199]. La distribution de taille des pores a été calculée avec un logiciel utilisant la méthode NLDFT.

Les poudres chauffés en dessous de 300 °C contiennent des pores de taille inférieure à 5 nm. Ce sont essentiellement des mesopores mais il y a aussi 30% de micropores. A 300 °C ces micropores sont éliminés et la distribution, centrée sur 4 nm, devient presque symétrique. Le chauffage au dessus de 300 °C produit d'abord un décalage de la distribution vers les gros pores (à 400 °C) puis une diminution du volume poreux. Ces deux effets sont accompagnés d'une sévère diminution de la surface spécifique.

A partir du volume poreux (V_{pore}) et de la densité (ρ) il est possible de calculer la porosité (ϵ) par la relation :

$$\epsilon = \frac{voulume\ of\ pores}{total\ volume} = \frac{V_{pore}}{V_{pore} + \frac{1}{\rho}} \tag{5.3}$$

Les xérogels résultants du séchage des sols à basse température ($\leq$ 100 °C) ont une porosité de 0.27. Cette valeur est très proche de la porosité attendue pour un matériau résultant de l'empilement compact de particules sphériques (0.26). En outre la distribution de pore est aussi en très bon accord avec un tel matériau ayant des particules de 6 nm étant donné que nous observons deux pics à 1 et 2.5 nm correspondant respectivement aux interstices tetraédriques (6 x 0.225 ∼ 1.4) et octaédriques (6 x 0.414 ∼ 2.5). Ainsi, comme l'avait déjà indiqué Xu et Anderson [172] durant l'étape de séchage les particules se réarrangent pour former un matériau compact. A cause de la répulsion électrostatique qui diminue la probabilité de collage, il se forme des agrégats denses.

Quand les xérogels sont chauffés il y a une augmentation de la porosité jusqu'à 300 °C (ϵ = 0.33) à cause de la perte de l'eau adsorbée en surface et de la déshydroxylation. Cependant le gain de porosité reste limité. Au dessus de 300 °C les hydroxydes de surface qui empêchaient le contact direct entre les cristallites sont presque totalement éliminés. Ceci entraine une croissance progressive des cristallites induisant une réorganisation des particules accompagné d'un effondrement de la porosité.En définitive sans l'ajout d'additif il semble difficile de produire des revêtements poreux à partir de sols stabilisés par répulsion électrostatique puisqu'ils vont toujours donner des films compacts au séchage. Pour préparer

des revêtements en contrôlant la porosité à partir de ces sols la stratégie consiste à rajouter un polymère qui va s'adsorber à la surface des particules. Durant l'étape de séchage le polymère va recouvrir les particules et si les conditions du traitement de calcination bien choisies, la porosité libérée par la combustion du polymère peut être conservée. Comme le nombre de coordination est plus faible la stabilité thermique est améliorée. Par exemple l'ajout de polyéthylène glycol (PEG) dans ces sols augmente considérablement la surface spécifique et la porosité des poudres obtenus après calcination [110]. Il existe une teneur optimale en PEG au-delà de laquelle la surface et la porosité de nouveau décroissent .

En outre un autre avantage de l'ajout de polymère est l'élimination des fissures qui sont souvent observées, en particulier sur des substrats en acier, dès que le revêtement dépasse une épaisseur critique.

Si le polymère est un copolymère bloc il peut induire l'autoassemblage des nanoparticules pour former des structures mésoporeuses. Par exemple l'addition du Pluronic F127 produit des xérogels avec des surfaces spécifiques et des porosités plus grandes qu'une quantité équivalente de PEG 2000. Si en outre le polymère est fortement ancré à la surface des particules la stabilité du sol est accrue par stabilisation stérique.

Effet des paramètres expérimentaux sur les propriétés des revêtements MOCVD (Metallo Organic Chemical Vapor Deposition)

Le contrôle des diverses propriétés structurales des revêtements CVD requiert une bonne compréhension de l'influence de chacun des paramètres « procédé », classiquement étudiée par des simulations numériques ou des études paramétriques qui consistent à réaliser de nombreuses expériences en ne modifiant qu'un paramètre à la fois. Cette démarche expérimentale « pas à pas » est souvent longue et couteuse [133]. L'idée ici est de mettre en œuvre et de valider une méthodologie par plan d'expériences afin d'explorer l'ensemble du domaine expérimental en un nombre réduit d'expériences et de retrouver les différents résultats de la littérature relatifs aux revêtements de TiO_2 par MOCVD (en particulier ceux réalisés au laboratoire [166, 124]. Le domaine expérimental couvrira donc l'essentiel de la gamme explorée lors de ces travaux précédents sauf pour la pression puisque le revêtement de surface de géométrie complexe recquiert d'opérer sous pression légèrement réduite (quelques dizaines de torr)

Plan d'expériences - Description

Les objectifs d'un plan d'expériences sont de : cribler les facteurs les plus importants et les hiérarchiser, modéliser le comportement du système étudié (ici les revêtements de TiO_2) afin de prédire et/ou d'optimiser sa réponse sur le domaine expérimental explorer.

La mise en œuvre de ce plan passe par le choix judicieux des paramètres opératoires (facteurs X) et de leur gamme de variation ainsi que celui de ou des réponses (Y) du système à analyser, le choix du type de plan en fonction de l'objectif souhaité (criblage ou optimisation), l'écriture de la matrice des essais (en valeurs réduites et réelles) qui correspond à la liste des expériences à conduire, la résolution du plan pour hiérarchiser les facteurs et établir le modèle qui corrèle la réponse aux facteurs, la validation du plan par une étude statistique.

L'expertise du laboratoire sur les revêtements MOCVD de TiO_2 [166, 124] a permis d'identifier quatre facteurs particulièrement pertinents à considérer : la distance entre le substrat et la douchette des vapeurs de précurseur (d), la température de dépôt (Tc), la pression au sein du réacteur (P), la température de vaporisation du précurseur (Tp). Quant aux réponses, l'étude s'intéressera à l'influence des paramètres opératoires sur la prise de masse, l'épaisseur, la rugosité, la composition polymorphique et la taille des cristallites.

Un plan factoriel complet associé à 4 facteurs (plan 2^4) nécessite 16 expériences. Compte tenu du nombre de réponses à caractériser et de l'objectif du plan (ici essentiellement du criblage), il est préférable de choisir un plan fractionnaire 2^{4-1} qui réduit le nombre d'expériences à 8 en considérant négligeables les interactions entre plus de deux facteurs. Ce type conduit à un modèle d'ordre 1, c'est-à-dire une relation linéaire entre la réponse et les facteurs tout en tenant compte des interactions entre les différents facteurs.

Plan d'expériences - Résultats

Effet sur la masse

Les facteurs prépondérants sont la pression et la température de dépôt : la prise de masse est d'autant plus grande que la température est élevée et la pression faible. De plus ces deux facteurs interagissent : l'augmentation de la température n'a pas le même effet sur la masse à basse et haute pression. Ces résultats sont confirmés par la littérature [124] : globalement la vitesse de dépôt augmente avec la température pour se stabiliser ensuite (succession de 2 régimes : cinétique limitée par les réactions de surface puis par le transport de matière), néanmoins cette croissance est plus faible pour les hautes pressions que les pressions plus réduites. D'où l'interaction pression / température observée.

Effet sur l'épaisseur de dépôt

De même que pour la masse, les facteurs les plus influents sur l'épaisseur de dépôt sont la pression et la température de dépôt, avec une forte interaction entre ces deux paramètres. Cela s'explique par le fait que la vitesse de croissance suit une loi d'Arrhenius et s'accompagne d'un changement de morphologie : le film est compact à 350 °C et devient colonnaire quand la température s'élève [166, 124]. De la même manière une augmentation de la fraction molaire (donc une diminution de la pression) provoque globalement une augmentation de l'épaisseur déposée

Effet sur la rugosité

Là encore, les facteurs prépondérants sont la température de dépôt et la pression : le dépôt est d'autant plus rugueux que la température est élevée et la pression réduite. Cela peut s'expliquer par le fait que la température favorise le grossissement des grains. La figure 4.6 montre que la température favorise une croissance colonnaire, présentant de nombreuses arêtes effilées alors qu'à basse température les dépôts sont compacts. Cette différence de morphologie (directement corrélée à la rugosité) peut s'expliquer la vitesse de croissance : l'arrangement des grains est d'autant plus compact que la vitesse de dépôt est faible. Ces conclusions sont confirmées par la littérature [166, 124] et cette dépendance de la morphologie avec la pression et la température est en accord avec le modèle de Thornton.

Effet sur la composition polymorphique

La composition polymorphique correspond au pourcentage d'anatase présent dans le revêtement de TiO_2. Etant donné que l'anatase est la forme allotropique « basse température » en comparaison avec le rutile, il est normal que la composition polymorphique soit d'autant plus faible que la température est élevée. D'autre part cette composition est inversement corrélée avec la pression. Ces tendances se retrouvent dans la littérature [166]. Il est également mis l'accent sur le fait que la gamme température de croissance de la forme anatase est fortement dépendante de la nature du substrat : elle est plus étendue sur silicium que sur acier. Sur acier inox 304L par exemple, il est possible de trouver du rutile à partir de 450 °C en équilibre avec la forme anatase, et uniquement du rutile à 550 °C. Une des explications possible à cette nucléation du rutile est la diffusion des cations du substrat en acier au sein de la couche qui orienterait sa structure.

Enfin, la fraction molaire de précurseur (inversement liée à la pression) influence la structure du dépôt dans le sens ou des fractions molaires réduites favorisent le rutile. D'autre part, à température constante, la vitesse de croissance de l'anatase est plus élevée

que celle du rutile. Ainsi, dans la gamme de température où il possible de synthétiser les 2 formes allotropiques, les revêtements épais seront plus riches en anatase [124]

Effet sur la taille des cristallites

Dans la gamme expérimentale explorée au cours de cette étude, la taille des cristallites (déterminées à partir des diffractogrammes X) reste constante autour de 30 nm.

Relation entre la structure et les propriétés fonctionnelles des revêtements de TiO_2

Afin d'établir les corrélations entre les diverses propriétés des revêtements de TiO_2 synthétisés par voie sol gel et CVD et l'activité photocatalytique qui en résulte, les données ont été dans un premier temps traitées séparément. Comme toutes ces caractéristiques sont intimement liées, il a été décidé de réaliser une analyse en composante principale (ACP, outil statistique) : cela consiste à représenter l'ensemble des données dans un nouveau système de coordonnées (les composantes principales, qui correspondent en fait aux vecteurs propres de la matrice de corrélations des propriétés des divers films) qui permet de afin de dégager clairement les corrélations (Figure 5.20).

Les composantes principales 2 et 3 peuvent être attribuées respectivement à la composition polymorphique et l'activité photocatalytique, indiquant ainsi que ces 2 propriétés ne sont pas corrélées. Ceci est en contradiction avec la littérature qui montre l'importance de la présence d'anatase sur l'activité photocatalytique.

La composante principale 1 est proche la masse, ce qui devrait être confirmé si l'ensemble des revêtements présentaient une masse optimale vis-à-vis de l'activité photocatalytique, c'est-à-dire une masse déposée au-delà de laquelle l'activité photocatalytique n'évolue plus.

La masse, l'épaisseur et la rugosité semblent corrélées, probablement reliés par la vitesse de croissance qui conditionne l'arrangement et la morphologie des grains comme le montre la figure 5.21 : un dépôt fin / poreux / peu rugueux par sol-gel, plus épais / compact / rugueux par CVD basses temperature et fraction molaire et épais / colonnaire / très rugueux par CVD hautes température et fraction molaire. La relation entre la masse et l'épaisseur est cependant à nuancer par la présence ou non de porosité : une même masse déposée peut conduire à un dépôt fin et compact ou épais et poreux.

La relation entre la rugosité et l'activité photocatalytique n'est pas claire dans la mesure où elle résulte de 2 phénomènes compétitifs : une rugosité élevée est associée à une large présence de défauts donc de sites potentiels de recombinaison néfastes à l'activité photocatalytique. En revanche elle peut également aller dans le sens d'une surface spécifique

élevée et donc contribuer favorablement à la photocatalyse

La taille des cristallites qui varie dans une gamme peu étendue (10 – 30 nm : à ne pas confondre avec celle des grains) est corrélée avec l'activité photocatalytique. Il aurait sans doute été plus pertinent de corréler l'activité photocatalytique à la taille des grains mais en raison du faible contraste des images AFM et MEB, le traitement numérique des images n'a pas pu être réalisé. Néanmoins, une augmentation de la taille des cristallites est susceptible d'entrainerune diminution des joints de grains, donc des sites de recombinaisons des paires électron-trou, ce qui explique l'impact positif sur l'activité photocatalytique.

A cette étude, il manque clairement l'influence de la surface spécifique et de la porosité qu'il n'a pas été possible de déterminer.

Conclusions et perspectives

L'objectif de cette étude était de réaliser des revêtements de TiO_2 présentant une large variété de morphologie et d'établir les corrélations entre la structure de ces couches et leurs propriétés fonctionnelles, notamment en terme de photocatalyse. D'une manière générale ces objectifs ont été atteints.

Par voie sol-gel, le challenge était de synthétiser des sols stables par hydrolyse du tetra-isopropropxide de titane. Des dispersions de nano-cristallites de TiO_2 dans l'eau stable sur une longue durée (plus d'un an) en termes de composition polymorphique, taille d'agglomérats et de cristallites ont été synthétisés dans les conditions optimales suivantes:

1. $H_2O/Ti = 50\text{-}100$,

2. $H^+/Ti \sim 0.2$,(HNO_3 comme acide),

3. Température de peptisation d'environ 80 °C afin d'évaporer l'isopropanol.

De tels sols sont composés d'agrégats de nano-cristallites (5-6 nm) de forme anatase ($\sim$ 90%) et de brookite. D'autres sols composés de pure anatase ont été obtenus par complexation partielle de TTIP par l'acetylacétone avant l'hydrolyse. A partir de ces sols, stabilisés par les répulsions électrostatiques, il n'a pas été possible d'obtenir des revêtements poreux car pendant la période de séchage les particules se réarrangent de manière compacte. Néanmoins il a également été possible en ajoutant à ces hydrosols des polymères promoteurs de porosité (PEG, copolymer block Pluronic F-127) de réaliser des revêtements de porosité de TiO_2contrôlée

Pour la voie CVD, l'objectif était de mettre en œuvre et valider une démarche de méthodologie expérimentale par plan fractionnaire pour, en un nombre réduit d'expériences

(moins de 15), cribler et comprendre les relations entre les paramètres procédé et les propriétés des revêtements synthétisés. Globalement cette méthodologie est validée puisqu'elle permet de retrouver l'ensemble des résultats des travaux précédents réalisés au laboratoire. Elle met notamment en évidence l'influence prépondérante de la pression et de la température de dépôt.

Enfin de manière à établir les corrélations entre l'ensemble des propriétés des revêtements réalisés par voies sol-gel et CVD, une analyse en composante principale a été menée. Elle a permis de conclure quant à l'absence de corrélation entre l'activité photocatalytique et la composition polymorphique, ce qui réfute pas mal d'hypothèses de la littérature et qui s'explique par la large gamme de morphologie et structure de matériaux explorée lors de cette étude, grâce notamment à l'emploi de deux techniques de dépôt.

Le manque principal reste la détermination de la porosité et de la surface spécifique. Pour cette dernière, des études préliminaires de mesure par voltammétrie cyclique semblent prometteuses.Il reste également à synthétiser davantage de revêtements (sol-gel notamment) afin de confirmer ces tendances. Il faut optimiser les conditions de dépôts par dip-coating en jouant sur la viscosité, la vitesse de retrait afin de couvrir une plus large gamme d'épaisseur déposée. Enfin concernant la CVD, il serait intéressant de mener une étude sur la stabilité du précurseur de manière à fiabiliser encore plus le procédé. Ces résultats peuvent trouver leur application dans de nombreux domaines tels que la catalyse et les cellules solaires.

Bibliography

[1] O. Carp, C.L. Huisman, and A. Reller. Photoinduced reactivity of titanium dioxide. *Progress in Solid State Chemistry*, 32(1-2):33 – 177, 2004.

[2] Leif A.A. Pettersson, Lucimara S. Roman, and Olle Inganäs. Modeling photocurrent action spectra of photovoltaic devices based on organic thin films. *J Appl Phys*, 86:487, 1999.

[3] Theander M., Yartsev A., Zigmantas D., Sundstrom V., Mammo W., Andersson M.R., and Inganas O. Photoluminescence quenching at a polythiophene/C60 heterojunction. *Phys Rev B*, 61:12957, 2000.

[4] Barbara van der Zanden, Roel van de Kroland Joop Schoonman, and Albert Goossensa. Enhanced photoluminescence at poly(3-octyl-thiophene)/ TiO_2 interfaces. *Applied Physics Letters*, 84(14):2539 – 2541, 2004.

[5] Nazeeruddin M. K., Kay A., Rodicio I., Humphry-Baker R., Mueller E., Liska P., Vlachopoulos N., and Graetzel M. Conversion of light to electricity by cis-X2bis(2,2'-bipyridyl-4,4'-dicarboxylate)ruthenium(II) charge-transfer sensitizers (X = Cl-, Br-, I-, CN-, and SCN-) on nanocrystalline titanium dioxide electrodes. *Journal of the American Chemical Society*, 115(14):6382–6390, 1993.

[6] Laura L. Tobin, Thomas O'Reilly, Dominic Zerulla, and John T. Sheridan. Characterising dye-sensitised solar cells. *Optik - International Journal for Light and Electron Optics*, 122(14):1225 – 1230, 2011.

[7] Jean-Marie Herrmann. Fundamentals and misconceptions in photocatalysis. *Journal of Photochemistry and Photobiology A: Chemistry*, 216(2-3):85 – 93, 2010.

[8] Nosaka Y., Kishimoto N., and Nishino J. Factors governing the initial process of TiO_2 photocatalysis studied by means of in-situ electron spin resonance measurements. *J Phys Chem*, 102:10279, 1998.

[9] Bahnemann D.W., Cunningham J., Fox M.A., Pelizzetti E., Pichat P., and Serpone N. In Heltz GR, Zepp RG, and Crosby DG, editors, *Aquatic and surface photochemistry.*, page 261. Lewis Publishers, 1994.

[10] Herrmann J.M., Guillard C., Arguello M., Aguera M., Tejedor A., and Piedra L. et al. Determination of the reaction pathway and identification of intermediate products by various analytical methods. *Catal Today*, 54:353, 1999.

[11] Mao Y., Schoneich C., and Asmus K.D. Identification of organic acids and other intermediates in oxidative degradation of chlorinated ethanes on titania surfaces en route to mineralization: a combined photocatalytic and radiation chemical study. *J Phys Chem*, 95:80, 1991.

[12] Turchi C.S. and Ollis D.F. Photocatalytic degradation of organic water contaminants: Mechanisms involving hydroxyl radical attack. *J Catal*, 122:178, 1990.

[13] Parra S., Olivero J., and Pulgarin C. Relationships between physicochemical properties and photoreactivity of four biorecalcitrant phenylurea herbicides in aqueous TiO_2 suspension. *Appl Catal B: Environ*, 36:75–85, 2002.

[14] Peral J. and Ollis D.F. Heterogeneous photocatalytic oxidation of gas-phase organics for air purification: acetone, 1-butanol, butyraldehyde, formaldehyde and m-xylene oxidation. *J Catal*, 136:554, 1992.

[15] Vorontsov A.V., Kurkin E.N., and Savinon E.N. Study of TiO_2 Deactivation during Gaseous Acetone Photocatalytic Oxidation. *J Catal*, 186:318, 1999.

[16] Kim S.B. and Hong S.C. Kinetic study for photocatalytic degradation of volatile organic compounds in air using thin film TiO_2 photocatalyst. *Appl Catal B: Environ*, 35:305, 2002.

[17] R.M. Alberci and W.F. Jardim. Photocatalytic destruction of VOCs in the gas-phase using titanium dioxide. *Appl Catal B: Environ*, 14:55–68, 1997.

[18] Mills A. and Moris S. Photomineralization of 4-chlorophenol sensitized by titanium dioxide: a study of the initial kinetics of carbon dioxide photogeneration. *J Photochem Photobiol A: Chem*, 71:75, 1992.

[19] Inel Y. and Okte A. Photocatalytic degradation of malonic acid in aqueous suspensions of titanium dioxide: an initial kinetic investigation of CO_2 photogeneration. *J Photochem Photobiol A: Chem*, 96:175, 1996.

[20] Matthews R.W. Kinetics of photocatalytic oxidation of organic solutes over titanium dioxide. *J Catal*, 111:264, 1988.

[21] M.A. Fox and M.T. Dulay. Heterogeneous photocatalysis. *Chem Rev*, 93:341, 1993.

[22] Anpo M., Shima T., Kodama S., and Kubokawa Y. Photocatalytic hydrogenation of propyne with water on small-particle titania: size quantization effects and reaction intermediates. *J Phys Chem*, 91:4305, 1987.

[23] Hermann J.M. Heterogeneous photocatalysis: fundamentals and applications to the removal of various types of aqueous pollutants. *Catalysis Today*, 53:115–129, 1999.

[24] D.F. Ollis, E. Pelizzetti, and N. Serpone. Photocatalyzed destruction of water contaminants. *Environ. Sci. Technol.,*, 25:1522–1529, 1991.

[25] Nimlos M.R., Jacoby W.A., Blake D.M., and Milne T.A. Direct mass spectrometric studies of the destruction of hazardous wastes. 2. Gas-phase photocatalytic oxidation of trichloroethylene over titanium oxide: products and mechanisms. *Environ Sci Technol*, 27:732–740, 1993.

[26] Wang K.H., Tsai H.H., and Hsieh Y.H. The Kinetics of Photocatalytic Degradation of TCE in Gas Phase over TiO_2 Supported on Glass Bead. *Appl Catal B: Environ*, 17:313, 1998.

[27] Jacoby W.A., Blake D.M., Noble R.D., and Koval C.A. Kinetics of the Oxidation of Trichloroethylene in Air via Heterogeneous Photocatalysis. *J Catal*, 157:87–96, 1995.

[28] Wang W., Chiang L.W., and Ku Y. Decomposition of benzene in air streams by UV/TiO_2 process. *J Hazard Mater*, 101:133, 2003.

[29] Hager S., Bauer R., and Kudielka G. Photocatalytic oxidation of gaseous chlorinated organics over titanium dioxide. *Chemosphere*, 41:1219–1225, 2000.

[30] Al-Ekabi H., Safarzadeh-Amiri A., Sifton W., and Story J. Advanced technology for water purification by heterogeneous photocatalysis. *Int J Environ Pollut*, 1:125, 1991.

[31] Murov S.L, Carmichael I, and Huy G.L. *Handbook of photochemistry.* 2 edition, 1993.

[32] André M. Braun and E. Oliveros. How to evaluate photochemical methods for water treatment. *Water Science and Technology*, 35:17–23, 1997.

[33] Hung C.H. and Marinas B.J. Role of Chlorine and Oxygen in the Photocatalytic Degradation of Trichloroethylene Vapor on TiO_2 Films. *Environ Sci Technol*, 31:562, 1997.

[34] M.S. Dieckmann and K.A. Gray. A comparison of the degradation of 4-nitrophenol via direct and sensitized photocatalysis in TiO_2 slurries. *Water Res*, 30:1169–1183, 1996.

[35] Okamoto K., Yamamoto Y., Tanaka H., and Itaya A. Kinetics of heterogeneous photocatalytic decomposition of phenol over anatase TiO_2 powder. *Bull Chem Soc Jpn*, 58:2023, 1985.

[36] Chen D. and Ray A.K. Photocatalytic kinetics of phenol and its derivatives over UV irradiated TiO_2. *Appl Catal B: Environ*, 23:143–157, 1999.

[37] Crittenden J.C, Liu J., Hand D.W., and Perran D.L. Photocatalytic oxidation of chlorinated hydrocarbons in water. *Water Res*, 31:429–438, 1997.

[38] C.S. Turchi and D.F. Ollis. Mixed reactant photocatalysis: Intermediates and mutual rate inhibition. *J Catal*, 119:483, 1989.

[39] J. Bandara, J. Kiwi, R. Humphry-Baker, and C. Pulgarin. *J Adv Oxid Technol*, 1:126, 1996.

[40] L.Campion, C. Giannotti, and J. Ouzzani. Photocatalytic degradation of 5-Nitro-1,2,4-Triazol-3-one NTO in aqueous suspention of TiO_2. Comparison with fenton oxidation. *Chemosphere*, 38:1561, 1999.

[41] A. Assabane, Y.A. Ichou, H. Tahiri, C. Guillard, and J.M. Hermann. Photocatalytic degradation of polycarboxylic benzoic acids in UV-irradiated aqueous suspensions of titania.: Identification of intermediates and reaction pathway of the photomineralization of trimellitic acid (1,2,4-benzene tricarboxylic acid). *Appl Catal B: Environ*, 24:71–87, 2000.

[42] B. Ohtani, Y. Ogawa, and S.I. Nishimoto. Photocatalytic Activity of Amorphous−Anatase Mixture of Titanium(IV)Oxide Particles Suspended in Aqueous Solutions. *J Phys Chem B*, 101:3746–3752, 1997.

[43] S.S. Watson, D. Beydoun, J.A. Scott, and R. Amal. The effect of preparation method on the photoactivity of crystalline titanium dioxide particles. *Chem Eng J*, 95:213, 2003.

[44] L. Saadoun, J.A. Ayllón, J. Jimènez-Becerril, J. Peral, X. Domènech, and R. Rodríguez-Clemente. *Appl Catal B: Environ, 21 (1999), p. 269*, 21:269, 1999.

[45] K.H. Wang, Y.H. Hsieh, C.H. Wu, and C.Y. Chang. The pH and anion effects on the heterogeneous photocatalytic degradation of o-methylbenzoic acid in TiO_2 aqueous suspension. *Chemosphere*, 40:389, 2000.

[46] Y.Chen, K.Wang, and L.Lou. Photodegradation of dye pollutants on silica gel supported TiO_2 particles under visible light irradiation. *J Photochem Photobiol A: Chem,*, 163:281, 2004.

[47] W. Xiaohong, J. Zhaohua, L. Huiling, X. Shigang, and H. Xinguo. *Thin Solid Films*, 441:130, 2003.

[48] D.W. Bahnemann, S.N. Kholuiskaya, R. Dillert, A.I. Kulak, and A.I. Kokorin. Photodestruction of dichloroacetic acid catalyzed by nano-sized TiO_2 particles. *Appl Catal B: Environ*, 36:161–169, 2002.

[49] W. Chu. Photodechlorination Mechanism of DDT in a UV/Surfactant System. *Environ Sci Technol,*, 33:421–425, 1999.

[50] J. Bachman and H.H. Patterson. Photodecomposition of the Carbamate Pesticide Carbofuran: Kinetics and the Influence of Dissolved Organic Matter. *Environ Sci Technol*, 33:874–881, 1999.

[51] X.S. Miao, S.G. Chu, and X.B. Xu. Degradation pathways of PCBs upon UV irradiation in hexane. *Chemosphere*, 39:1639–1650, 1999.

[52] M.I. Stefan and J.R. Bolton. Reinvestigation of the Acetone Degradation Mechanism in Dilute Aqueous Solution by the UV/H_2O_2 Process. *Environ Sci Technol,*, 33:870–873, 1999.

[53] D. Dullin and T. Mill. *Environ Sci Technol,*, 16:811, 1982.

[54] Lazzeri M., Vittadini A., and Selloni A. Structure and energetics of stoichiometric TiO_2 anatase surfaces. *Phys. Rev. B*, 63:155409, Mar 2001.

[55] S.R. Kumar, C.S. Asha, K. Vasudevan, R. Suja, P. Mukundan, and K.G.K. Warrier. *Mater Lett,*, 38:161, 1999.

[56] A. Karthikeyan and R.M. Almeida. Crystallization of SiO_2–TiO_2 glassy films studied by atomic force microscopy. *J Non-Cryst Solids*, 274:169–174, 2000.

[57] K.N.P. Kumar, K. Keizer, and A.J. Burggraaf. Textural evolution and phase transformation in titania membranes: Part 1.—Unsupported membranes . *J Mater Chem,*, 3:1141–1149, 1993.

[58] H. Zhang and J. F. Banfield. Thermodynamic analysis of phase stability of nanocrystalline titania. *J. Mater. Chem.*, 8:2073–2076, 1998.

[59] Y. Kubota, C. Niwa, T. Ohnuma, Y. Ohko, T. Tatsuma, and T. Mori et al. Protective effect of TiO_2 particles on UV light induced pyrimidine dimer formation. *J Photochem Photobiol A: Chem,*, 141:225–230, 2001.

[60] J.H. Braun. Titanium dioxide's contribution to the durability of paint films. *Prog Org Coat,*, 15:249–260, 1987.

[61] R.R. Blakey. Evaluation of paint durability - natural and accelerated. *Prog Org Coat*, 13:279–296, 1985.

[62] T. Rentschler and A. Reller. *European Coatings*, 4:80, 1999.

[63] N.S.Allen, H.Katami, and F.Thompson. Influence of titanium dioxide pigments on the thermal and photochemical oxidation of low density polyethylene film. *Eur Polym J,*, 28:817–822, 1992.

[64] S.L. Pugh and J.T. Guthrie. *Dyes Pigments,*, 55:109, 2002.

[65] N.S. Allen. *Polym Degrad Stab,*, 29:73, 1990.

[66] T.Corralles, C.Peinado, N.S.Allen, M.Edge, G.Sandoval, and F.Catalina. A chemiluminescence study of micron and nanoparticle titanium dioxide: effect on the thermal stability of metallocene polyethylene. *J Photochem Photobiol A: Chem,*, 156:151–160, 2003.

[67] A. Wold. Photocatalytic properties of titanium dioxide TiO_2. *Chem. Mater*, 5:280–283, 1993.

[68] K. Michael, Schindler, Marinus, and Kunst. Charge-carrier dynamics in titania powders. *J. Phys. Chem.*, 94:8222–8226, 1990.

[69] Shan Cong and Yiming Xu. Explaining the High Photocatalytic Activity of a Mixed Phase TiO_2: A Combined Effect of O_2 and Crystallinity. *J. Phys. Chem. C*, 115:21161–21168, 2011.

[70] E.N Vorontsov, A.V.and Kurkin and E.N. Savinov. Study of TiO_2 deactivation during gaseous acetone photocatalytic oxidation. *J. Catal.*, 186:318–324, 1999.

[71] A. Fujishima and K. Honda. Electrochemical Photolysis of Water at a Semiconductor Electrode. *Nature*, 238:37, 1972.

[72] A.L. Pruden and D.F. Ollis. Photoassisted heterogeneous catalysis: The degradation of trichloroethylene in water. *J Catal,*, 82:404–417, 1983.

[73] C.Y. Hsiav, C.L. Lee, and D.F. Ollis. Heterogeneous photocatalysis: Degradation of dilute solutions of dichloromethane (CH_2Cl_2), chloroform ($CHCl_3$), and carbon tetrachloride (CCl_4) with illuminated TiO_2 photocatalyst. *J Catal,*, 82:418, 1983.

[74] B.O'Regan and M.Grätzel. A low-cost, high-efficiency solar cell based on dye-sensitized colloidal TiO_2 films. *Nature*, 353:737, 1991.

[75] R.Wang, K.Hashimoto, A.Fujishima, M.Chikuni, E.Kojima; A.Kitamura, M.Shimohigoshi, and T.Watanabe. Light-induced amphiphilic surfaces. *Nature*, 388:431, 1997.

[76] P.T. Moseley and B.C. Tofield. *Solid state gas sensors*. 1987.

[77] N. Kumazawa, M.R. Islam, and M. Takeuchi. *J Electrochem Chem*, 472:137, 1999.

[78] P.K. Dutta, A. Ginwalla, B.Hogg, B.R. Patton, B. Chwieroth; Z. Liang, P.Gouma, M.Mills, and S.Akbar. Interaction of Carbon Monoxide with Anatase Surfaces at High Temperatures:Optimization of a Carbon Monoxide Sensor. *J Phys Chem B*, 103:4412, 1999.

[79] Klinger M.M., Rahemtulla F., Prince C.W., Lucas L.C., and Lemons J.E. Proteoglycans at the bone-implant interface. *Critical Review in Oral Biology*, 9:449–463, 1998.

[80] Disegi J.A. and H. Wyss. Implant materials for fracture fixation: A clinical perspective. *Orthopedics*, 12:75–79, 1989.

[81] L. Polontchouk, J.Elbel, L. Eckert, J.Blum, E.Wintermantel, and H.M.Eppenberger. Titanium dioxide ceramics control the differentiated phenotype of cardiac muscle cells in culture. *Biomaterials*, 21:539–550, 2000.

[82] W.S. Oh, C. Xu, D.Y. Kim, and D.W. Goodman. Preparation and characterization of epitaxial titanium oxide films on Mo(100). *J Vac Sci Technol A,*, 15:1710, 1997.

[83] W.D. Brown and W.W. Granneman. C-V characteristics of metal-titanium dioxide-silicon capacitors. *Solid State Electron*, 21:837–846, 1978.

[84] C. Li, Z. Zheng, F. Zhang, S. Yang, H. Wang, and L. Chen et al. *Nucl Instrum Meth Phys Res B,*, 169:21, 2000.

[85] Ebelmen M. *Ann. Chimie Phys.*, 16:129, 1846.

[86] Ebelmen M. *C . R. Acad. Sci.*, 25:854, 1847.

[87] Liesegang R. E. *Photogr. Archiu.*, page 221, 1896.

[88] Heinisch H. K. *Crystal Growth in Gels*. Pennsylvania State University Press: State College, PA, 1970.

[89] Roy D. M.and Roy R. An experimental study of the formation and properties of synthetic serpentines and related layer silicate minerals. *Am. Mineralogist*, 39:957–975, 1954.

[90] Roy R. Aids in Hydrothermal Experimentation: II, Methods of Making Mixtures for Both "Dry" and "Wet" Phase Equilibrium Studies. *J. Am. Ceram. Soc.*, 39:145–146, 1956.

[91] Roy R. Gel Route to Homogeneous Glass Preparation. *J. Am. Ceram. Soc.*, 52:344, 1969.

[92] McCarthy G.J., Roy R., and McKay J.M. Preliminary Study of Low-Temperature "Glass" Fabrication from Noncrystalline Silicas. *J. Am. Ceram. Soc.*, 54:637–638, 1971.

[93] W.Stober, A. Fink, and E.Bohn. Controlled growth of monodisperse silica spheres in the micron size range. *J . Colloid Interface Sci.*, 26:62–69, 1968.

[94] Khadikar C. *The Effect of Adsorbed Poly(vin 1 Alcohol) on the Properties of Model Silica Suspensions*. PhD thesis, University of Florida: Gainesville, FL, 1988.

[95] C.Jeffrey Brinker and George W.Scherer. *Sol-Gel Science: The Physics and Chemistry of Sol-Gel Processing*. Academic Press, 1990.

[96] D. TRUYEN. *Elaboration par voie sol-gel de revêtements catalytiques sur substrats métalliques*. PhD thesis, Université de Toulouse, 2007.

[97] Bernardo Arcuri and Renato Bellarosa. Sol-gel technology: "The Nano-son's big mum" [Online]. @http://www.lswn.it/en/technologies/news/sol-gel-technology-the-nano-sonss-big-mum, 07 2010 (last accessed 02/2012).

[98] Larry L.Hench and Jon K. West. The sol-gel process. *Chem.Rev*, 90:33–72, 1990.

[99] Iler R. K. *The Chemistry of Silica*. Wiley, 1955.

[100] Iler R.K. *The Chemistry of Silica*. Wiley, 1979.

[101] G.Winter. *oil and Colour Chemist's Association*, 34:30, 1953.

[102] E. Bistan and I. Gomory. *Chem Zvesti*, 10:91, 1956.

[103] E.A. Barringer and H.K. Bowen. High-purity, monodisperse TiO_2 powders by hydrolysis of titanium tetraethoxide. 1. Synthesis and physical properties. *Langmuir*, 1:414, 1985.

[104] E.A. Barringer and H.K. Bowen. High-purity, monodisperse TiO_2 powders by hydrolysis of titanium tetratethoxide. 2. Aqueous interfacial electrochemistry and dispersion stability. *Langmuir*, 1:420, 1985.

[105] T. Boyd. Preparation and properties of esters of polyorthotitanic acid. *J Polym Sci*, 7:591, 1951.

[106] S. Minami and T. Ishino. Technical report, Osaka univ, 1953.

[107] N.M.S. Cullinane, J. Chard, G.F. Price, B.B. Millward, and G. Langlois. Organic derivatives of titanium. II. Preparation and properties of some ortho-esters. *J. Appl. Chem*, 1:400, 1951.

[108] L.L. Hench and D.R. Ulrich, editors. *Ultrastructure Processing of Ceramic Glasses and Composites*. Wiley, 1984.

[109] M. Vallet-Regi, M.L. Veiga-Blanco, and A. Mata-Arjon. *Ann. Quim.*, 76B:172,177,182,187, 1980.

[110] D. Vorkapic and T. Matsoukas. Effect of Temperature and Alcohols in the Preparation of Titania Nanoparticles from Alkoxides. *J.Am.Ceram.Soc*, 81:2815–2820, 1998.

[111] An Introduction to Zeta Potential and its Measurment [online]. @http://www.silver-colloids.com/Tutorials/Intro/pcs12.html, last accessed 28/02/2012.

[112] J. H. Jean and T. A. Ring. Nucleation and Growth of Monosized TiO_2 Powders from Alcohol Solution. *Langmuir*, 2:251–55, 1986.

[113] J.L. Look and C. F. Zukoski. Alkoxide-Derived Titania Particles: Use of Electrolytes to Control Size and Agglomeration Levels. *J. Am. Ceram. Soc.,*, 75 [6]:1587–95, 1992.

[114] L. Look and C. F. Zukoski. Colloidal Stability of Titania Precipitate Morphology: Influence of Short-Range Repulsions. *J. Am. Ceram. Soc*, 78 [1]:21–32, 1995.

[115] V. J. Nagpal, R. M. Davis, and J.S. Riffle. In Situ Steric Stabilization of Titanium Dioxide Particles Synthesized by a Sol–Gel Process. *Colloids Surf*, 87:25–31, 1994.

[116] Q. Xu, M. J. Gieselmann, and M. A. Anderson. The colloid chemistry of ceramic membranes. *Polym. Mater. Sci. Eng*, 61:889–893, 1989.

[117] M. A. Anderson, M. J. Gieselmann, and Q. Xu. Titania and alumina ceramic membranes. *J. Membr. Sci*, 39:243–258, 1988.

[118] C. Lijzenga, V. T. Zaspalis, K. Keizer, A. J. Burrgraaf, K. P. Kumar, and C. D. Ransjin. Nanostructure Characterization of Titania Membranes. *Key Eng. Mater*, 61;62:379–82, 1991.

[119] P. Yimsiri and M.R. Mackley. Spin and dip coating of light-emitting polymer solutions: Matching experiment with modelling. *Chemical Engineering Science*, 61(11):3496 – 3505, 2006.

[120] C. Jeffrey Brinker and Alan J. Hurd. Fundamentals of sol-gel dip-coating. *J. Phys. III France*, 4(7):1231–1242, 1994.

[121] Yu-Ping Zeng, Andre Zimmermann, Longjie Zhou, and Fritz Aldinger. Tape casting of PLZST tapes via aqueous slurries. *Journal of the European Ceramic Society*, 24(2):253 – 258, 2004.

[122] Forge-Dip Coating [Online]. @http://engineering1.pbworks.com/w/page/33764428/Revision for Pol - Ultan, Caoimhin - Feilim, last accessed 29/02/2012.

[123] Spin Coating [online]. @http://materials.web.psi.ch/Research/Thin-Films/Methods/Spin.htm, last accessed 29/02/2012.

[124] Florin-Daniel DUMINICA. *Fonctionnalisation de surfaces d'aciers par des procédés CVD compatibles avec le traitement de plaques au défilé : dépôts de TiO_2 et Fe*. PhD

thesis, L'Institut National Polytechnique de Toulouse and l'Unversité Politechnique de Bucarest, 2004.

[125] Spear K.E. Principles and applications of chemical vapour deposition. *Pure Appl Chem*, 54:1297–1311, 1982.

[126] P.C. Chou, Q. Zhong, Q.L. Li, K. Abazajian, A. Ignatiev, C.Y. Wang, E.E. Deal, and J.G. Chen. Optimization of Jc of YBCO thin films prepared by photo-assisted MOCVD through statistical robust design. *Physica C: Superconductivity*, 254(1–2):93 – 112, 1995.

[127] Yongdong Xu and Xiu-Tian Yan. *Chemical Vapour Deposition: An Integrated Engineering Design for Advanced Materials*. Springer, 2010.

[128] Bird R.B., Stewart W.E., and Lightfoot E.N. *Transport phenomena*. Wiley, New York, 1960.

[129] Constantin Vahlas. Chemical Vapour Deposition of Metals: from Unary Systems to Complex Metallic Alloys. In *3rd Euroschool, Ljubljana*, 2008.

[130] Glocker D.A. and Shah S.I. *Handbook of thin process technology*. Taylor & Francis, 1995.

[131] Pierson H.O. *Handbook of chemical vapour deposition (CVD)*. Noyes, Park Ridge, NJ, 2 edition, 1999.

[132] Choy K.L. Chemical vapour deposition of coatings. *Prog. Mater. Sci.*, 48:57–170, 2003.

[133] Z. Nami, O. Misman, A. Erbil, and G.S. May. Effect of growth parameters on TiO_2 thin films deposited using MOCVD. *Journal of Crystal Growth*, 179:522–538, 1997.

[134] K. Sugawara. Silicon Epitaxial Growth by Rotating Disk Method. *J. Electrochem. Soc.*, 119:1749–1760, 1972.

[135] S.V. Patankar. *Numerical Heat Transfer and Flud Flow*. Hemisphere, Washington DC, 1980.

[136] K. Lin and C. Spanos. Statistical equipment modeling for VLSI manufacturing: an application for LPCVD . *IEEE Trans. Semi. Manufac.*, 3:216, 1990.

[137] Z. Nami, A. Erbil, and G.S. May. *Proc. SPIE (Version 4.3),*, 2334:294, 1994.

[138] Z. Nami, O. Misman, A. Erbil, and G.S. May. Computer simulation study of the MOCVD growth of titanium dioxide films. *Journal of Crystal Growth*, 171(1–2):154 – 165, 1997.

[139] D.I. Fotiadis, A.M. Kremer, D.R. McKenna, and K. Jensen. Complex flow phenomena in vertical MOCVD reactors: Effects on deposition uniformity and interface abruptness. *J. Crystal Growth,*, 85:154, 1987.

[140] Zhong-Xin Chen and Anke Derking. TiO$_2$ thin films by chemical vapour deposition: control of the deposition process and film characterisation. *J. Mater. Chem.*, 3:1137, 1993.

[141] Qingming Zhang and Gregory L. Griffin. Gas-phase kinetics for TiO_2 CVD: hot-wall reactor results. *Thin Solid Films*, 263(1):65 – 71, 1995.

[142] Yoldas B.E. Hydrolysis of titanium alkoxide and effects of hydrolytic polycondensation parameters. *J Mater Sci*, 21:1087–1092, 1986.

[143] Yu J., Zhao X., and Zhao Q. Effect of surface structure on photocatalytic activity of TiO_2 thin films prepared by sol-gel method. *Thin Solid Films*, 379:7–14, 2000.

[144] Yu J., Zhao X., Du J., and Chen W. Preparation, microstructure and photocatalytic activity of the porous TiO_2 Anatase coating by Sol–Gel processing. *J Sol–Gel Sci Technol*, 17:163–171, 2000.

[145] Kim DJ, Hahn SH, Oh SH, and Kim EJ. Influence of calcination temperature on structural and optical properties of TiO_2 thin films prepared by sol–gel dip coating. *Mater Lett*, 57:355–360, (2002).

[146] Legrand-Buscema C, Malibert C, and Bach S. Elaboration and characterization of thin films of TiO2 prepared by sol-gel process. *Thin Solid Films*, 418:79–84, (2002).

[147] Zhang L, Zhu Y, He Y, Li W, and Sun H. Preparation and performances of mesoporous $TiO2$ film photocatalyst supported on stainless steel. *Appl Catal B*, 40:287–292, (2003).

[148] Bu S, Jin Z, Liu X, Yang L, and Cheng Z. Fabrication of TiO_2 porous thin films using PEG templates and chemistry of the process. *Mater Chem Phys*, 88:273–279, 2004.

[149] Bu SJ, Jin ZG, Liu XX, Yang LR, and Cheng ZJ. Synthesis of TiO_2 porous thin films by polyethylene glycol templating and chemistry of the process. *J Eur Ceramic Soc*, 25:673–679, 2005.

[150] Guo B., Liu Z., Hong L., and Jiang H. Sol gel derived photocatalytic porous TiO_2 thin films. *Surf Coat Technol*, 198:24–29, 2005.

[151] Djaoued Y, Thibodeau M, Robichaud J, Balaji S, Priya S, Tchoukanova N, and Bates SS. Photocatalytic degradation of domoic acid using nanocrystalline TiO_2 thin films. *J Photochem Photobiol A Chem*, 193:271–283, 2008.

[152] Oskam G, Nellore A, Penn RL, and Searson PC. The Growth Kinetics of TiO_2 Nanoparticles from Titanium(IV) Alkoxide at High Water/Titanium Ratio. *J Phys Chem B*, 107:1734–1738, (2003).

[153] Vorkapic D and Matsoukas T. Reversible Agglomeration: A Kinetic Model for the Peptization of Titania Nanocolloids. *J Colloid Interface Sci*, 214:283–291, 1999.

[154] Isley SL and Lee Penn R. Relative Brookite and Anatase Content in Sol-Gel-Synthesized Titanium Dioxide Nanoparticles. *J Phys Chem B*, 110:15134–15139, 2006.

[155] Jianxia Jiao, Qun Xu, and Limin Li. Porous TiO_2/SiO_2 composite prepared using PEG as template direction reagent with assistance of supercritical CO_2. *Journal of Colloid and Interface Science*, 316(2):596 – 603, 2007.

[156] Structure of Polyethylene Glycol[online]. @http://www.crawfordscientific.com/Agilent-J-W-PEG.htm, last accessed 29/02/2012.

[157] J. J. Escobar-Chávez, M. López-Cervantes, A.Naïk, Y. N. Kalia, D. Quintanar-Guerrero, and A.Ganem-Quintanar. Applications of thermo-reversible pluronic F-127 gels in pharmaceutical formulations. *J Pharm Pharmaceut Sci*, 9:339–358, 2006.

[158] Kyung-Jun Hwang, Jae-Wook Lee, Wang-Geun Shim, Hee Dong Jang, Se-Il Lee, and Seung-Joon Yoo. Adsorption and photocatalysis of nanocrystalline TiO_2 particles prepared by sol–gel method for methylene blue degradation. *Advanced Powder Technology*, Available online 1 June 2011(0), 2011.

[159] Rietveld H.M. A profile refinement method for nuclear and magnetic structures. *J Appl Crystallogr*, 2:65–71, 1969.

[160] Rodrıguez-Carvajal J. Recent developments of the program FULLPROF. Commission on powder diffraction (IUCr). *News Lett*, 26:12–19, (2001).

[161] Patterson A.L. The Scherers Formula for X-Ray particle size determination. *Phys Rev*, 56:978–982, 1939.

[162] Brunauer S., Hemmett P., and Teller E. Adsorption of gases in multimolecular layers. *J Am Chem Soc*, 60:309–319, 1938.

[163] Seaton N., Walton J., and Quirke N. A new analysis method for the determination of the pore size distribution of porous carbons from nitrogen adsorption measurements. *Carbon*, 27:853–861, 1989.

[164] D.J. Johnson, S.A. Al Malek, B.A.M. Al-Rashdi, and N. Hilal. Atomic force microscopy of nanofiltration membranes: Effect of imaging mode and environment. *Journal of Membrane Science*, 389(0):486 – 498, 2012.

[165] Gwyddion [Online]. @http://gwyddion.net/, last accessed 25/02/2012.

[166] Christos SARANTOPOULOS. *Photocatalyseurs a base de TiO_2 prepares par infiltration chimique en phase vapeur (CVI) sur supports microfibreux.* PhD thesis, L'Institut National Polytechnique de Toulouse, 2007.

[167] Simona Andreia JACOTA POPESCU. *Films minces de dioxyde de titane deposes sur titane par MOCVD: Microstructure et biocompatibilite.* PhD thesis, L'Institut National Polytechnique de Toulouse, 2008.

[168] NIST/SEMATECH. e-Handbook of Statistical Methods [Online]. @http://www.itl.nist.gov/div898/handbook/ , last accessed 15/02/2012.

[169] Richard Linder. *Les plans d'expériences. Un outil indispensable à l'expérimentateur.* 2005.

[170] Marie-Christine Sado and Gilles Sado. *Les plans d'expériences. De l'expérimentation à l'assurance qualité, 2ème édition.* 2000.

[171] Jon Shlens. Tutorial on Principal Component Analysis [Online]. @http://www.snl.salk.edu/ shlens/, last accessed 18/01/2012.

[172] Xu Q. and Anderson M.A. Synthesis of porosity controlled ceramic membranes. *J Mater Res*, 6:1073–1081, 1991.

[173] Bartlett J.R. and Woolfrey J.L. Production of sols from aggregated Titania precipitates, In: Better ceramics through chemistry V: materials research society symposium proceedings. *Materials Research Society, Pittsburg (Pa)*, 271:309–315, (1992).

[174] So WW, Park SB, Kim KJ, Shin CH, and Moon SJ. The crystalline phase stability of Titania particles prepared at room temperature by the sol–gel method. *J Mater Sci*, 36:4299–4305, (2001).

[175] Bosc F, Ayral A, Albouy PA, and Guizard C. A simple route for low-temperature synthesis of mesoporous and nanocrystalline anatase thin films. *Chemistry of Materials*, 15:2463–2468, (2003).

[176] Cordero-Cabrera M, Walker G, and Grant D. Effect of processing parameters on the particle size and stabilisation of Titania sols. *J Mater Sci*, 40:3709–3714, 2005.

[177] Sanchez C. and Livage J. Sol–gel chemistry from metal alkoxide precursors. *New J Chem*, 14:513–521, 1990.

[178] Terabe K., Kato K., Miyazaki H., Yamaguchi S., and Iguchi Y. Imai A. Microstructure and crystallization behaviour of TiO_2 precursor prepared by the sol–gel method using metal alkoxide. *J Mater Sci*, 29:1617–1622, (1994).

[179] Bischoff B.L. and Anderson M.A. Peptization process in the Sol–Gel preparation of porous anatase (TiO_2). *Chem Mater*, 7:1772–1778, (1995).

[180] Bancroft W.D. The theory of peptization. *J Phys Chem*, 20:85–117, 1916.

[181] Sen K.C. On the theory of peptization. *J Phys Chem*, 29:1533–1547, 1925.

[182] A. Pottier, S. Cassaignon, C. Chaneac, F. Villain, and J.P. Jolivet E.Tronc. Size tailoring of TiO_2 anatase nanoparticles in aqueous medium and synthesis of nanocomposites. Characterization by Raman spectroscopy. *J Mater Chem*, 13:877–882, (2003).

[183] Bosc F, Ayral A, Keller N, and Keller V. Room temperature visible light oxidation of CO by high surface area rutile TiO_2-supported metal. *Applied Catalysis B*, 69:133–137, 2007.

[184] Bleuzen A., Barboux-Doeuff S., Flaud P., and Sanchez C. Rheological study of titanium oxide-based gels. *Mater Res Bull*, 29:1223–1232, (1994).

[185] Julbe A., Guizard C., Larbot A., Mouchet C., Vacassy R., Metz R., and Cot L. Sol–gel processing of zirconia and titania membrane. *Proceeding of the international conference on inorganic membranes, Worcester MA USA*, page 17–25, (1994).

[186] Bokhimi X, Morales A, Novaro O, Lopez T, Sanchez E, and Gomez R. Effect of hydrolysis catalyst on the Ti deficiency and crystallite size of sol–gel–TiO_2 crystalline phases. *J Mater Res*, 10:2788–2796, 1995.

[187] Zhang H and Banfield JF. Understanding polymorphic phase transformation behavior during growth of noncrystalline aggregates: insights from TiO_2. *J Phys Chem B*, 104:3481–3487, 2000.

[188] Kosmulski M. and Matijevic E. Zeta potential of anatase TiO_2 in mixed solvents. *Colloids Surf*, 64:57–65, 1992.

[189] Yang Hua-Gui, Li Chun-Zhong, Gu Hong-Chen, and Fang Tu-Nan. Rheological behavior of titanium dioxide suspensions. *J Colloid Interf Sci*, 236:96–103, 2001.

[190] Kosmulski M. The significance of the difference in the point of zero charge between rutile and anatase. *Adv Colloid Interface Sci*, 99:255–264, (2002).

[191] Preocanin T and Kallay N. Point of zero charge and surface charge density of TiO_2 in aqueous electrolyte solution as obtained by potentiometric mass titration. *Croatica Chemica Acta*, 79:95–106, 2006.

[192] Ridley MK, Hackley VA, and Machesky ML. Characterization and Surface-Reactivity of noncrystalline anatase in aqueous solutions. *Langmuir*, 22:10972–10982, 2006.

[193] Fazio S, Guzman J, Colomer MT, Salomoni A, and Moreno R. Colloidal stability of nanosized Titania aqueous suspensions. *J Eur Ceramic Soc*, 28:2171–2176, 2008.

[194] Anderson M.A., Gieselmann M.J., and Xu Q. Titania and alumina ceramic membranes. *J Membr Sci*, 39:243–258, 1988.

[195] Goodwin J.W. and Hughes R.W. *Rheology for chemists: an introduction.* The Royal Society of Chemistry, London, 2002.

[196] Alphonse P, Bleta R, and Soules R. Effect of PEG on rheology and stability of nanocrystalline Titania hydrosols. *J Colloid Interf Sci*, 337:81–87, 2009.

[197] Bleta R, Alphonse P, and Lorenzato L. Nanoparticles route for the preparation in aqueous medium of mesoporous TiO_2 with controlled porosity and crystalline framework. *J Phys Chem C*, 114:2039–2048, 2010.

[198] Xu Q., Gieselmann M.J., and Anderson M.A. The colloid chemistry of ceramic membranes. *Poly Mater Sci Eng*, 61:889–893, 1989.

[199] Kumar KNP, Engell J, Kumar J, Keizer K, Okubo T, and Sadakata M. Pore-structure stabilization by controlling particle coordination. *J Mater Sci Lett*, 14:1784–1788, (1995).

[200] Miki T, Nishizawa K, Suzuki K, and Kato K. Preparation of thick TiO_2 film with large surface area using aqueous sol with poly (ethylene glycol). *J Mater Sci*, 39:699–701, 2004.

[201] Alphonse P and Ansart F. Catalytic coatings on steel for low-temperature propane pre-reforming to SOFC application. *J Col- loid Interface Sci*, 336:658–666, 2009.

[202] Tadros T.F. Steric stabilisation and flocculation by polymers. *Poly J*, 23:683–696, (1991).

[203] Mueller R, Kammler HK, Wegner K, and Pratsinis SE. OH surface density of SiO_2 and TiO_2 by thermo gravimetric analysis. *Langmuir*, 19:160–165, (2003).

[204] M. Wojdyr. Fityk : a general-purpose peak fitting program. *J. Appl. Cryst*, 43:1126–1128, 2010.

[205] L.D. Burke and O.J. Murphy. Cyclic voltammetry as a technique for determining the surface area of RuO_2 electrodes. *Journal of Electroanalytical Chemistry and Interfacial Electrochemistry*, 96:19–27, 1979.